



Thèse de doctorat
de l'Université de Paris



Préparée à l'Université Paris Diderot

École Doctorale “Physique en Île-de-France” - ED 564

Laboratoire Matière et Systèmes Complexes

**Interactions médiées dans la matière molle
et tension de surface des fluides actifs**

**Mediated interactions in soft matter
and surface tension of active fluids**

Par **Ruben Zakine**

Thèse de doctorat de Physique théorique

dirigée par Jean-Baptiste FOURNIER
et Frédéric VAN WIJLAND

Présentée et soutenue publiquement à Paris le 20 septembre 2019
Devant un jury composé de

Bruno ANDREOTTI, Professeur, ENS, Paris

Denis BARTOLO, Professeur, ENS de Lyon

Ludovic BERTHIER, Directeur de recherche, Univ. de Montpellier

Leticia CUGLIANDOLO, Professeur, UPMC, Paris

Erwin FREY, Professeur, LMU, Munich

Jean-Baptiste FOURNIER, Professeur, Univ. Paris Diderot

Frédéric VAN WIJLAND, Professeur, Univ. Paris Diderot

Examineur

Président

Rapporteur

Examinatrice

Rapporteur

Directeur

Co-Directeur



Except where otherwise noted, this work is licensed under
<https://creativecommons.org/licenses/by-nd/3.0/fr/>

Remerciements

Je tiens à remercier chaleureusement mes deux directeurs de thèse, Jean-Baptiste Fournier et Frédéric van Wijland. Leur gentillesse, leur bienveillance constante à mon égard, leur pédagogie, leur entrain et leur générosité m'ont porté depuis mon premier jour au laboratoire. Un troisième mousquetaire, répondant au nom de Julien Tailleur, a également été très présent durant ces trois années et a participé à mon encadrement. Sa générosité, son aide et ses conseils avisés illustrent de nouveau la chance que j'ai eue d'atterrir dans cette formidable équipe.

Je remercie les membres du jury pour le temps qu'ils m'ont consacré, et un grand merci à Ludovic Berthier et Erwin Frey d'avoir endossé les rôles de rapporteurs.

Il est aussi de nombreuses personnes sans qui je n'aurais jamais pu arriver au résultat final. Je tiens à remercier mes collaborateurs *and in particular Yongfeng Zhao with whom I never stopped interacting*. Merci à Adrian Daerr pour toutes les sympathiques discussions de physique (mais pas que). *Thanks also to Yariv Kafri and Miloš Knežević with whom my discussions were brief but dense*. Je dois également beaucoup à Doru Constantin et ses recherches qui ont été le point de départ de notre travail sur les colloïdes dans les phases lamellaires. Merci également à Paolo Galatola qui a réalisé de superbes simulations à partir de nos calculs.

Durant ces trois ans, j'ai aussi eu la chance de beaucoup voyager. *I had the chance to be warmly welcomed in the research group of Shigeyuki Komura at the Tokyo Metropolitan University. My time in Japan was marvellous thanks to the students and thanks to Shigeyuki Komura, and I benefited from great discussions with Professor Komura and Riiichi Okamoto*. Sans oublier bien sûr ma fabuleuse rencontre imprévue avec Ram Adar et David Andelman... *Thanks a lot to Kranthi Mandadapu who accepted me in his lab for one month. I benefited from great and lively discussions during my stay there*. Merci également à Martin Lemoine qui m'a encadré pour mon premier stage de recherche à l'Institut d'Astrophysique de Paris et qui m'a donné une première excellente image de la recherche.

Merci à Vincent Démery et Marc Durand qui ont eu la sympathie d'accepter les rôles administratifs de tuteur et parrain dans le comité de suivi de ma thèse. Merci à Laurette Tuckerman pour son aide. Merci aux membres du laboratoire MSC qui en font sa richesse, et en particulier, merci à Bérengère Abou et Matthieu Roché pour tous les bons moments passés à discuter de tout sauf de physique ! Un grand merci évidemment à Marlène Hanoomie pour sa sympathie, sa gentillesse, et le travail qu'elle fournit pour

nous au quotidien.

Mais les chercheurs qui m'ont le plus chaleureusement accueilli et pris sous leur aile sont bien entendu les Docteurs Agnese Curatolo et Mourtaza Kourbane-Houssene ! Ils m'ont guidé au laboratoire, enseigné les bases d'UNIX et de C, et passé des heures à m'aider à débbugger mes programmes... J'ai eu une grande chance de partager leur bureau car j'ai non seulement pu bénéficier de leurs compétences, mais j'ai en plus partagé d'excellents moments de rigolade. Merci évidemment aussi à Annette, Anouchka, David, Mélina, Jérémy, Satochi, Thibaut et Yongfeng grâce à qui j'étais tous les jours profondément heureux d'aller à la fac. Je me suis toujours senti un peu moins idiot après nos discussions, alors un grand merci à vous !

Évidemment, je ne serais jamais arrivé jusque-là si ma famille ne m'avait pas épaulé depuis si longtemps. Merci à mes parents qui ont toujours été présents pour moi et qui m'ont transmis, entre autres, le goût pour l'étude. Merci à mes grands-mères pour leur amour inconditionnel que je garde ancré en moi. Merci à Laurinda qui s'est toujours occupée de moi comme si j'étais l'un de ses enfants. Merci à mes tantes et mes oncles qui m'ont tant soutenu dans mes études, allant jusqu'à m'accueillir des jours et des semaines chez elles/eux pour des stages intensifs de français et d'anglais. Merci à mes sœurs qui égaient ma vie. Merci enfin à Léa pour sa douceur, son humour et son indulgence envers toutes mes idioties du quotidien.

Résumé

Cette thèse aborde deux thématiques chères à la matière molle, à savoir, l'apparition d'interaction médiées par le milieu entre objets de taille nanométrique ou micrométrique, et la notion de tension de surface dans les systèmes hors de l'équilibre.

La première partie de cette thèse est consacrée à l'étude de systèmes dans lesquelles les interactions entre particules sont médiées par un champ fluctuant. Nous étudions dans un premier temps un système hors d'équilibre et nous montrons que l'existence d'interactions médiées associées à l'activité des particules qui place le système hors de l'équilibre conduit à la formation de structures complexes. Nos prédictions s'appuient sur des méthodes de mécanique statistique mais surtout sur des méthodes de dynamique non-linéaire utilisées pour prédire l'apparition de motifs dans les systèmes dans lesquels il existe une quantité conservée. La seconde étude de cette partie est dédiée à l'explication des interactions émergentes observées expérimentalement dans des systèmes de particules colloïdales insérées dans des phases lamellaires lyotropiques. En partant de la description microscopique des interactions entre particules et couches de surfactants, nous calculons de façon exacte la force effective qui émerge entre particules seulement. Ces résultats analytiques sont ensuite utilisés pour distinguer et identifier, parmi deux types possibles d'interactions entre lamelles et particules, lequel est observé dans notre système expérimental à l'étude.

La seconde partie de cette thèse s'attache à identifier la notion de tension de surface dans les fluides actifs. Nous parvenons à proposer une définition de la tension de surface qui relie les forces macroscopiques aux forces microscopiques existant entre particules, ou entre particules et un mur confinant. Lorsque le fluide actif est en contact avec un mur, la tension de surface solide-fluide est en général d'une nature plus complexe que celle que l'on peut définir pour son analogue d'équilibre. Par ceci, nous entendons que la valeur mesurée de la tension de surface peut dépendre de la géométrie ou d'autres détails de l'appareil de mesure utilisé. Nous montrerons également que des appareils de mesure correctement choisis permettent d'accéder à une tension de surface intrinsèque au matériau (et non plus à la géométrie), caractéristique d'une variable d'état d'équilibre. Les séparations de phases de type liquide-vapeur peuvent être également rencontrées dans les assemblées de particules auto-propulsées, lorsque celles-ci sont sujettes à une séparation de phase induite par la motilité. Nous montrons alors que la tension de surface associée à l'interface liquide-vapeur possède une définition mécanique cohérente avec son interprétation d'équilibre.

Mots clefs : Physique statistique, Matière molle, Formation de patterns, Matière active

Abstract

This thesis focuses on two topics ubiquitous in soft matter: first, mediated interactions between nano-to-micrometer sized objects, second, surface tension in out-of-equilibrium systems.

The first part of this thesis is devoted to the properties of a system of particles whose interactions are mediated by a fluctuating background. We start with a nonequilibrium study and we show that the combination of mediated interactions and of the nonequilibrium drive leads to complex structures. Our predictions, beyond statistical mechanical methods, rest on extending the methods of nonlinear dynamics in pattern forming systems, to systems with a local conservation law. The second study of this part is dedicated to an equilibrium experimental system of colloidal particles embedded in lyotropic lamellar phases. Relying on a bottom-up approach, we implement the details of the interaction between each colloidal particle and each lamella to come up with an exact description of the effective force emerging between colloids. These analytical results are then used to discriminate between two types of interaction, both being possibly encountered in experiments.

The second part of this thesis focuses on the notion of surface tension for interfaces involving active fluids. We will come up with a definition relating macroscopic forces to microscopic ones, either between particles or, when applicable, between particles and a confining medium. When the active fluid is in contact with a solid boundary, the solid-fluid surface tension is, in general, a more complex quantity than its equilibrium counterpart. By this we mean that its value may depend on the geometry or other details of the measuring device. We will also show that a carefully designed probe allows us to access an equation-of-state-abiding surface tension akin to its equilibrium counterpart. Liquid-vapor interfaces can also be encountered in assemblies of self-propelled particles when these undergo a motility-induced phase separation. We show also that the surface tension associated to a liquid-vapor interface possesses a mechanical definition that echoes the equilibrium one.

Keywords: Statistical Physics, Soft Matter, Pattern Formation, Active Matter

Contents

Résumé	5
Abstract	7
Contents	9
Introduction	13
I Mediated interactions in a fluctuating medium	17
1 Mediated interactions in soft matter	19
1.1 Where are mediated interactions relevant?	19
1.2 How to deal with the mediated interactions?	24
1.2.1 Equilibrium systems	24
1.2.2 Out-of-equilibrium systems	25
2 Field mediated interactions between active spins	27
2.1 Introduction	27
2.2 Model	29
2.3 Numerical simulations	30
2.3.1 Equilibrium benchmark	31
2.3.2 Active system	33
2.4 Mean-field behavior	33
2.4.1 Equilibrium free energy	33
2.4.2 Mean field dynamics	37
2.4.3 Numerical solution of the coupled partial differential equations . .	38
2.5 Pattern analysis	40
2.5.1 Linear stability analysis	40
2.5.2 Weakly nonlinear analysis	43
2.5.3 Roll and square stability	49
2.6 From equilibrium system to active system	50
2.6.1 Mean-field analysis	52
2.6.2 Linear stability analysis	52

2.7	Entropy production	56
2.8	Conclusion	61
3	Colloidal particles in lamellar phases	63
3.1	Introduction	63
3.2	Lamellar phase model	65
3.2.1	Definition	65
3.2.2	Fluctuations	67
3.3	Interactions between colloidal particles	68
3.3.1	Membrane-binding colloidal particles	69
3.3.2	Membrane-excluding colloidal particles	72
3.4	Typical results	74
3.4.1	Orders of magnitude	74
3.4.2	Results for binding colloids	75
3.4.3	Results for excluded-volume colloids	76
3.5	Comparison with experiments	77
3.5.1	Monte Carlo simulations for colloids in the $C_{12}E_5$ lamellar phase	78
3.5.2	Experimental structure factors	80
3.6	Conclusion	81
II	Surface tension of active fluids	83
	An elusive quantity?	85
4	What is surface tension?	87
4.1	The macroscopic approach	87
4.1.1	First contact	87
4.1.2	Measurement: the Wilhelmy plate experiment	88
4.2	The microscopic origin	90
4.3	Free energy and closed container	93
5	A Virial approach to surface tension	97
5.1	The Virial for the pressure	97
5.2	The Virial for planar interfaces	102
5.2.1	Surface tension in a rectangular box	102
5.2.2	Mesosopic shortcut	107
5.2.3	Virial with a phase separation	110
6	Measuring surface tension of active fluids	113
6.1	A delicate measurement	113
6.1.1	The Langmuir experiment	113
6.1.2	Why does the active measurement give non-trivial results?	115
6.1.3	The dipolar field created by the junction	118
6.2	Accessing the bare surface tension	120

6.2.1	A setup where currents do not contribute	120
6.2.2	The hard-wall limit and the Virial surface tension	121
6.3	The liquid-vapor surface tension	122
6.3.1	The Wilhelmy probe for active fluids	123
6.3.2	Simulation results	126
Conclusion		131
A Details on experiments of colloids in lamellar phases		133
A.1	Monte Carlo simulations	133
A.2	Joint validation of the Monte Carlo simulations and the Percus-Yevicz approximation	134
B Details on the surface tension for active fluids		137
B.1	Vanishing nematic tensor	137
B.2	Measurements in the computer simulations	138
Publications		139
Bibliography		140

Introduction

The emergent properties of a system made of a large number of interacting agents are probably the most gripping phenomena encountered in physics. Whether molecules, colloids, bacteria, agents may be of very different nature, size and shape. Statistical Physics strives to predict the behavior of such complex assemblies at scales directly accessible to observation. The broad spectrum of approaches commonly used in statistical physics (mechanics, classical or quantum, computer simulations, analytical computations...), along with the numerous fields to which these considerations may apply (thermodynamics, chemistry, biophysics, hydrodynamics, economics...) have profoundly seduced the student I was.

In particular, the fact that the behavior of biological systems could be qualitatively and quantitatively captured by physics and mathematics was quite appealing to me. In general, for systems which feature an energy imbalance between injection in and dissipation out of their environment, predicting the steady state is impossible because the details of the dynamics play a role in the final state (whereas they are, remarkably and surprisingly, irrelevant to infer the steady state of systems in equilibrium). Yet, there is a class of nonequilibrium systems for which the out-of-equilibrium drive occurs at the very scale of the agents composing the system. In such systems, referred to as active matter systems, where particles are identical, and where the system does not *a priori* break any spatial symmetry, physicists are inclined to focus on a finite number of intensive quantities such as density, (effective) temperature [LMC08], pressure [Sol+15], etc., that echo the equilibrium ones, and that may define the state of the system [Gin+15], or at least that may help to characterize its steady state.

In addition, for nano-to-micrometer-scale systems that are typically encountered in soft matter and biology, another layer might drive the system to a second level of complexity. In these systems, particles are indeed most of the time embedded in a medium, typically a fluid-like material and, in addition to direct physical interactions between agents that still exist, there is also the possibility for a particle to modify the surrounding medium, which in return, affects the motion and the stationary position of other particles. Such indirect interactions are said to be mediated by the medium in such systems. Several examples come to mind: passive nano-particles embedded in liquid crystals that develop non-local interactions [Pou+97], but also membrane-deforming active proteins at the membrane surface [NF17], or quorum-sensing bacteria that interact *via* sensing and secreting a chemical agent released in the medium. In these systems, what mediates the

interaction can, most of the time, be described by a field (density, elasticity, height or thickness of an interface,...), and the spatial variations of the field impact the particles' behavior. In equilibrium, with a coarse-grained description to linear order, what controls the (free) energy cost of a field gradient is (surface) tension. A question that we take up in this thesis is whether there exists a similar quantity for nonequilibrium systems, and this question is in line with the previous one: it is part of the search for thermodynamic quantities which would give hints on the behavior of the system.

These considerations lead us to formulate general questions that guide our research as physicists. For instance, to what extent is it possible to coarse-grain nonequilibrium systems? How to get rid of irrelevant degrees of freedom? Is it possible to integrate out a background field with which particles interact? Can we extract a class of nonequilibrium systems whose behavior can be described by an effective free energy? Is it possible to come up with meaningful state variables for out-of-equilibrium systems?

The work of this thesis will be devoted to answering, on specific cases, different aspects of the questions phrased out above.

This thesis is divided in two parts. The first part is dedicated to the study of two different systems that have a common basis, namely, many particles embedded in an elastic medium. In both cases, we use a continuous description for the medium, whereas we use an individual resolution for particles. Because of the local interaction between the particles and the medium, particles end up interacting with each other and these interactions govern their different phases. In Chapter 1 we will start with review on mediated interactions in statistical physics and in soft matter, with particular emphasis on recent experimental realizations. In Chapter 2, aiming at describing the collective effects induced by active state flips of proteins in the biological membrane, we build a simplified active model retaining the minimal and major physical ingredients. This allows us to carry out analytical derivation of the boundaries of the phase diagram. We also explore the different pattern formation regimes, whose multitude stems from the existence of a conserved field, namely the density of particles. This bottom-up approach is also useful to track down the dissipation in the system at the particle level. At the end of the chapter, we open on the various descriptions we can choose for the elastic field, along with a hydrodynamic description we should adopt to model the lipid bilayer faithfully. In Chapter 3, we embark on an equilibrium description of colloidal particles embedded in an aqueous lamellar phase made of lipids or surfactants. By means of Monte Carlo simulations and X-ray scattering experiments, we are able to distinguish between our different theoretical models.

In Part II, we focus on an another class of active particles, namely self-propelled active particles. With the secret and remote goal of understanding wetting and interface phenomena in active liquids, we focus on the first step: that of understanding surface tension. In Chapter 4 we review the different approaches one can follow to apprehend surface tension, both from its microscopic and from its macroscopic mechanical definitions. In Chapter 5 we introduce a Virial derivation for the surface tension of active fluids, in the spirit of the analogous derivation for the pressure by Clausius. We then focus, in Chapter 6, on specific experimental setups that allow for a mechanical measurement of surface tension between an active fluid and a solid, or between an active

liquid and its vapor. These setups are notably useful to pinpoint the inherent difficulty of such measurements: steady state currents generically dress up our force measurement, hence leading to an *a priori* probe-dependent surface tension. Our approach will combine Monte Carlo simulations and analytical computations.

Part I

Mediated interactions in a fluctuating medium

Chapter 1

Mediated interactions in soft matter

1.1 Where are mediated interactions relevant?

Let us start with a macroscopic example. We all have in mind the attraction or the repulsion that occur between air bubbles or cereal grains at the surface of a liquid, a phenomenon referred to as ‘the Cheerios effect’. To quantitatively predict the phenomenon, one never returns to a microscopic level description. Instead, an effective theory combining surface tension and buoyancy is invoked, and one adopts a continuous description for the surface of the fluid. With these ingredients, we are able to interpret the Cheerios effect in terms of an *effective* force between floating objects [VM05]. Though intuitive and simple, this example already shows that the general approach of the physicist is to eliminate as many degrees of freedom as possible without losing any information that would be essential to the prediction of the motion of the observed particles. In addition, in this example, coarse-graining up to the macroscopic scale has led to a non-fluctuating description of the fluid. Thermal fluctuations can indeed be neglected in the dynamics of macroscopic objects, but they always play a role in the definition of the macroscopic thermodynamic quantities like pressure and surface tension.

The former setup provides a macroscopic example of a soft matter system where interactions are mediated by the medium. When are we prompted to think in term of mediated interactions? Assuming scale separation between the particles and the constituents of the medium in which they are embedded, one typically considers mediated interactions when the particles deform the embedding medium and when there is an energy cost associated to this deformation. This local deformation can propagate (the coarse-grained medium displays for instance some elasticity), and the cost needed to embed a second particle in the medium is different from the cost needed to embed the first particle. Since the deformation created by an object varies with the distance from this object, the energy cost depends on the distance between the embedded objects. In addition, embedding an object in a medium reduces the configuration space in which the medium is allowed to fluctuate. If several particles are placed in the medium, the fluctuations of the medium are constrained by the relative position of the particles. The restriction of the configura-

tion space for the medium (associated to a loss of entropy) can induce, in average, what are called *fluctuation-induced* forces between the particles. Again, these forces depend on the relative position of the particles.

Why are these mediated effective interactions relevant? In general, physicists may be committed to exhibiting collective behaviors, or collective organization, of particles at different scales, and this because collective behaviors of particles usually explain the macroscopic properties of a material. Especially in soft matter, materials may present interesting properties, endowed with names that reflect the sense of humor of who discovered them: materials can be flabby or granular, neither solids, nor fluids... Such great level of complexity mainly stems from molecular constituents with a large number of degrees of freedom, which physicists are yearning to eliminate. To predict phase behaviors, effective theories and effective interactions have eventually proven very useful, for instance in the description of polymers and liquid crystals.

Here, we choose to focus on a certain class of systems where a scale separation occurs between the particles, typically nano-to-micrometer-sized objects, and the constituents of the medium in which they are embedded. As formerly stated, the collective behavior of these particles has continuously drawn the interest of physicists because they see possible ways to achieve functionalization of materials [BG70; LM79; Ham03; Fir+01; Lew+13; LYS14]. Relying on mediated interactions only, without considering the details of the embedding medium, facilitates the predictions on the phase behavior. Following a bottom-up approach, several experimental groups have focused on the mediated interaction between a couple of objects when embedded in media such as giant vesicles [Van+16; SD16], lamellar phases, smectic and nematic liquid crystals [Pou+97; Eva+13], or non polar Newtonian fluids [Bri+13]. The latter reference actually provides an interesting example where mediated interactions lead to a transition to collective motion of the particles. Let us review here some of the recent experimental realizations.

Thanks to recent progress in real-time imaging with optical microscopy, it is possible to measure the full time-realization of the position of particles embedded in a giant unilamellar vesicle, and thus to access to effective interaction potential between particles. In Ref. [Van+16], the authors show that the curvature deformation caused by the micrometer-sized colloids embedded in the vesicle membrane leads to attraction between particles, see Fig. 1.1. The amplitude of this attraction is $\sim 3k_B T$ for particles two diameters away from each other. This result is also interesting because deformations go far beyond the linear regime. In the linear regime, the repulsion of the inclusions when they each impose the same local curvature, whatever the sign of the curvature, is predicted [FG15].

At smaller scales, it becomes very difficult to optically resolve inclusions in lipid membranes [Sez+17]. Imaging proteins in biological membranes is of paramount importance to test hypotheses on protein cooperation in cell signalling. Many theoretical and experimental works have indeed focused on the interactions between membrane proteins that can deform the biological membrane. Depending on their shape and conformation, proteins may impose a local curvature. Recent experiments have succeeded in isolating such proteins and they have pinpointed the strong coupling that occurs between the protein conformation and the local shape of the membrane [Fri+14]. These measurements are

No display

Figure 1.1 – Left: Measurement of effective interaction between two colloidal particles embedded in a giant unilamellar vesicle as a function of their geodesic separation s , for different values of the membrane tension σ . Center: confocal image of colloids (green) wrapped by the vesicle membrane (magenta). Scale bar is 1 μm . Right: cross-section of the simulation of two particles (green) adhered to a coarse-grained membrane (magenta) at separation $s = 1.5D_p$, with the diameter of the particles $D_p = 0.98 \pm 0.03 \mu\text{m}$. *Reproduced from Ref. [Van+16].*

performed with electron microscopy (see Fig. 1.2) and they seem particularly difficult to achieve *in vivo*. Without the possibility of imaging proteins, computer simulations

No display

No display

No display

Figure 1.2 – Left: Ring formed of proteins called ATP-Binding Cassette transporters (ABC-transporters) in a lipid membrane. Black bar represents 5 nm. Center: Computation from electron-microscopy showing the structure of the ring. Right: zoom on two ABC-transporters embedded in the lipid bilayer (blue domain). *Reproduced and adapted from Ref. [Fri+14].*

are intensively used to bring answers to questions on collective effects between proteins induced by the local deformation the latter enforce on the membrane. In particular, recent simulations have focused on transmembrane domain of proteins embedded in the lipid membrane [WBS09a; Kat+16], or on curvature inducing proteins at the membrane surface [NF17]. For many protein channels, such as the potassium channel KcsA, the transmembrane domain can change size, for instance due to a pH variation [Sum+14] or to the action of a chemical substrate. The conformational change may lead to the local deformation of surrounding lipids that adopt new conformation and orientation. When there is a large discrepancy between the transmembrane domain of the protein and the hydrophobic width of the bilayer, the protein displays what is called a *hydrophobic mismatch*. Such a mismatch is believed to induce effective elastic interactions between

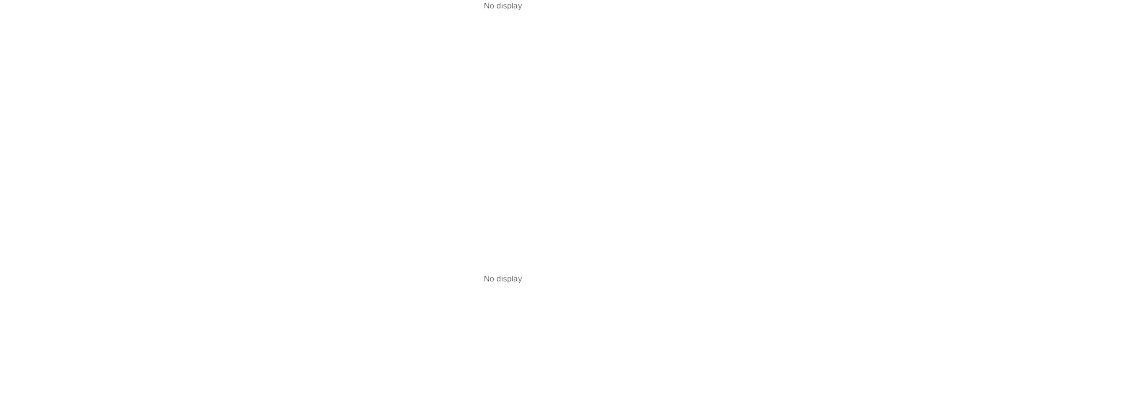


Figure 1.3 – Top: side view of simulations of proteins embedded in a lipid bilayer. The hydrophobic tail of the lipids is in pink, the hydrophilic head is in grey. Top left: a membrane protein with a hydrophobic mismatch. The transmembrane domain of size $\ell = 2.3$ nm is smaller than the hydrophobic width of the bilayer. Top right: membrane protein with no hydrophobic mismatch; hydrophobic transmembrane domain is $\ell = 3.1$ nm. Bottom: top view of two proteins getting closer to each other because their hydrophobic mismatch locally favors a lipid-disordered phase. Grey line: phase separation line between the lipid-ordered and lipid disordered phase in the membrane. *Reproduced and adapted from Ref. [Kat+16].*

proteins [WBS09a], and may also induce a first-order phase transition in the membrane between a liquid-ordered phase of lipids far from the protein and a liquid-disordered phase of lipids around the protein, see Fig. 1.3 adapted from [Kat+16].

The former examples have focused on interactions mediated by a quasi two-dimensional medium, namely the lipid bilayer. Yet, other types of mediated interactions can also be encountered in bulk fluids. In particular, it might seem easier to achieve self-organization of particles into complex structures if interactions are anisotropic, thus creating preferential directions of assembling. To do so, anisotropic fluids like liquid crystals are more likely to mediate anisotropic interactions than isotropic fluids (e.g. water). In Ref. [LMS09], the authors explicitly show that faceted colloidal polygons display multipolar elastic interactions in a nematic liquid crystal. For instance, triangles and pentagons interact *via* dipolar interactions, whereas squared-shape colloids display quadrupolar interactions. In an other experiment, using laser-tweezers to guide the clustering process, spherical colloidal particles have been assembled into 3D crystals in a nematic fluid. The new colloidal crystal exhibits interesting electrostriction properties [Nyc+13]. Research on nematic colloids also extends in the direction of externally tunable colloids [Eva+13]. These can optically be shaped and deformed by a laser while in the liquid crystal bath. The colloid can be considered as an active particle, in the sense that its conformational changes, externally driven, break the thermodynamic equilibrium imposed by the bath.

Finally, colloidal condensation can occur with fluctuation-induced forces. These forces should be mentioned since they exist in many soft matter systems. More specifically

No display

Figure 1.4 – Different colloidal particles embedded in a nematic liquid crystal. Left: sequence of two squared colloids, orienting then getting closer, *reproduced from [LMS09]*. Center: 3D crystal of colloids, fluorescent confocal polarizing microscopy (top), and schematic view in the nematic (bottom), *reproduced from [Nyc+13]*. Right: colloidal rod in a nematic, and deformed rod under the action of a laser scan along the red arrow (schematic view on the right), *reproduced from [Eva+13]*.

No display

Figure 1.5 – Colloids in a critical water-lutidine mixture. On the left part, colloids spread on one layer. Indeed, the left part is coated with a hydrophilic substrate, and Casimir-like interactions are attractive between the colloids and the plate. The right part is coated with a hydrophobic substrate and colloids are subjected to repulsive critical Casimir forces. They arrange in 3D clusters. *Reproduced and adapted from [Soy+08]*.

here, what we have in mind are the Casimir-like forces emerging between particles that constrain a fluctuating medium. These forces have been measured between a colloidal particle and a plate in a critical binary mixture of water and lutidine [Her+08]. The constraint on the medium is implemented here through the coating of the material which induces preferential affinity of the material surface for either water or lutidine. Long-range fluctuations of the relative density of the fluids are thus constrained by the surfaces. Similarly to the force, predicted by Casimir [Cas48], that appears between two metal plates in vacuum and which is due to the quantum fluctuations of the electromagnetic field, in this setup also a force develops between the field-constraining objects. Using this effect, colloidal particles have been assembled on selected areas of a plate with a chemically-patterned coating, see Fig. 1.5.

As we have just explained, mediated interactions can be found almost everywhere in soft matter. Identifying their origin is often instrumental to achieve bottom-up design of new materials, or to achieve accurate manipulation of micrometer-sized objects. It can be

challenging to analytically extract these interactions, especially when working with out-of-equilibrium systems for which relying on thermodynamics is impossible. Hydrodynamics effects can also be difficult to treat since they may lead to long-range correlations. In the following, we review some of the theoretical approaches that make it possible to predict the emerging mediated interactions.

1.2 How to deal with the mediated interactions?

1.2.1 Equilibrium systems

Long time and stationary properties of a given physical system are often the easiest one to access, especially in equilibrium. Among common question marks having to do with collective behavior: Has a condensation of particles occurred? Is the system fluid? Is it a solid? In these cases, if the system is in equilibrium, the dynamics has no influence on the configurations in the final state, no matter how complicated the microscopic dynamics might be. Extracting the mediated interaction between the particles amounts to integrating out the degrees of freedom of the underlying field with which particles locally interact. At the end of the procedure, one obtains an effective Hamiltonian containing the particles' position (or particles density) only. Then, from this effective interaction, with less degrees of freedom to analyze, it can be easier to construct the phase diagram, using the standard tools from statistical physics of interacting particles. Let's add, in passing, a small comment on Hamiltonians at this point. In soft matter, Hamiltonians might refer to already coarse-grained free energies. The use of a word instead of the other (Hamiltonian or free energy) depends on the scale at which we look. For instance, we usually refer to the Helfrich Hamiltonian to describe the bending and tension energy of a given profile of the membrane bilayer. The concepts of bending energy and surface tension are meaningful when the degrees of freedom of the underlying lipids have all been integrated out. The membrane is then described as a two-dimensional sheet. The bending modulus and the tension thus always implicitly depend on temperature. The Helfrich Hamiltonian for the membrane can be considered as a free energy of the lipid phase for a given curvature profile¹.

Let us come back to the integration of the underlying field. It turns out that this procedure can be carried out analytically when the interaction Hamiltonian is at most quadratic in the field, provided that the background field is also described by a Gaussian Hamiltonian. Then, the effective force between particles can be directly obtained from the minimization of the Hamiltonian. However, an elastic description for the field and the couplings is not always possible. Especially when the particles locally constrain the value of the field. For instance, a protein imposes the local curvature of the membrane bilayer [NF17], a silica colloid tightly binds to adjacent bilayers of surfactants and fixes

¹At smaller scales, we encounter again a similar hierarchy when considering Van der Waals interactions. Indeed, these interactions are mediated by the fluctuations of the electromagnetic field [CP48] that we have integrated out to get effective interactions. These interactions are then absorbed in the Hamiltonian of interacting particles. They are even usually considered as pairwise forces, which cannot be the case of fluctuation-induced forces.

the interlayer width at that position (see Chapter 3), etc. When considering such strong couplings, mediated interactions always contain the ‘athermal’ elastic interaction and the interaction induced by the fluctuations. Sometimes, for some peculiar Hamiltonians, interactions mediated by the medium can artificially be split between an elastic interaction and a fluctuation-induced interaction, or Casimir-like interaction. Such a separation can be used to explicitly pinpoint the role of these fluctuation-induced interactions since they display universal features. For instance, in the case of critical binary mixtures (Fig. 1.5), the critical Casimir forces are proportional to temperature and depend only on the geometry of the interacting objects. The force between two plates of area S , separated by a distance L in a bath of a critical binary mixture at temperature T reads $F_C = k_B T \theta (\tau (L/\xi_0^+)^{1/\nu}) S/L^3$ [KD91; Gam+09a], with $\tau = (T - T_c)/T_c$ the reduced temperature, ξ_0^+ the non-universal amplitude coming from the correlation length divergence at critical point ($\xi(\tau \rightarrow 0^+) = \xi_0^+ \tau^{-\nu}$), and ν the universal exponent ($\nu = 0.6301(4)$ for the three-dimensional Ising universality class) [Gam+09a; PV02]. In general, mediated interactions contain both the elastic contribution and the Casimir one, and one contribution cannot be isolated from the other.

All in all, when looking at systems in equilibrium, the dynamics can be bypassed to infer the stationary states. By calculating the partition function, we access the interaction energies, along with stationary correlations. We will follow this approach in Chapter 3 to predict the collective behaviors of colloidal particles embedded in lamellar phases of water and surfactants in equilibrium.

1.2.2 Out-of-equilibrium systems

For nonequilibrium systems, it is no longer possible to integrate out the degrees of freedom of the field, starting from the Hamiltonian only. Instead, we need to know how particles move and how the background field evolves with time to infer mediated interactions. Even if one would like to access the steady state only, it turns out that nonequilibrium steady states depend on the details of the dynamics. To predict the steady states, one no longer has a “miracle recipe” as in equilibrium. Rather, one follows several *ad hoc* routes which are impossible to thoroughly list here. Nonetheless, we wish to mention a couple of standard approaches, often used in a combination to fuel the predictions on a given model.

If enough computing power is available, simulating the full system – the dynamics of each particle, along with the dynamics of the medium – is an option. Implementing and running complex simulations can prove time-greedy though. To simplify the problem, a good starting point is to describe the ensemble of particles as a density field, and to extract an evolution equation for the density of particles. Since particles evolve with a stochastic dynamics, the evolution of the density field is stochastic as well. Sometimes, inferring the stochastic equation on the density field, without coarse-graining, is possible. Most of the time, however, some coarse-graining is needed to close the coupled partial differential equations that describe the system under study. In the end, it may be easier to carry out predictions from the obtained coupled PDEs. In particular, performing a linear stability analysis to predict the destabilization of a spatially homogeneous phase

is often useful.

In the next chapter, we are combining the two approaches described above to infer the steady states of our system of diffusing active particles interacting with a background Gaussian field. The PDEs description will prove useful as it allows us to rationalize the phase diagram (both the phase boundaries and the ordered nature of these phases).

Chapter 2

Field mediated interactions between active spins

The goal of this chapter is to build a generic model belonging to the same family of systems as those described in Chapter 1. We shall consider a system of independent point-like particles performing a Brownian motion while interacting with a Gaussian fluctuating background. These particles are in addition endowed with a discrete two-state internal degree of freedom that is subjected to a nonequilibrium source of noise. We explore the phase diagram of the system with Monte Carlo simulations and a mean-field analysis. Our model, in that we consider point-like particles interacting with the field only, is new. The following results are new also. By means of a weakly nonlinear analysis on the coupled PDEs describing the evolution of our system, we account for the parameter-dependence of the boundaries of the phase and pattern diagram in the stationary state. We show in addition that the patterns created by the active noise survive a small amount of equilibrium. Finally, we compute the entropy production rate in our active system and we relate it to the different regimes observed in the simulations. This work was accomplished under the joint supervision of Jean-Baptiste Fournier and Frédéric van Wijland.

2.1 Introduction

An early approach to the question of why and how active particles, e.g., proteins in cell membranes, self-organize appeared in Ref. [Che04; CC06; CM10]. In a parallel series of works on reactive two-state particle systems, spinodal decomposition coupled to active flips between the states has been shown to lead to a wealth of complex patterns. These have been described in Ref. [OS87; OB88; PF98; GSJ94; GDM95]. A common feature to these approaches, necessary for the active flips to produce non trivial patterns, is the requirement to start from directly interacting objects, either by assuming two-body interactions or in a coarse-grained form by describing these in terms of an *ad hoc* Cahn-Hilliard field.

Here, we resolve particles at the individual level and we assume their individual motion to be diffusive. We further endow our particles with a two-state, spin-like, internal degree of freedom that can be switched by an external drive (this is where activity will come into play). Second, we choose to describe the embedding medium by a coarse-grained field. Third, we consider a coupling between the medium and the degrees of freedom –both spin and position– of the particles, that will lead to mediated interactions. In order to focus on the latter, we omit from our model any direct interaction (hard-core, attractive or else) between particles. The dynamics of the medium itself is assumed to be assumed local and purely relaxational (model A-like). The out-of-equilibrium nature of the system comes from the active conformation switch of the particle that breaks detailed balance. Beyond proteins in biomembranes, such externally driven conformational changes can also be found in synthetic soft-matter systems (see [Fri+14; GS18; Che04] for recent references).

Even with the simplifying assumptions that have led to our model, our particles do evolve far from equilibrium, and no free-energy based method is available. Predicting collective phenomena thus requires to implement a variety of approaches, both numerical (Monte Carlo) and analytical (mean-field equations, noiseless reaction-diffusion equations). We present the details of the model and in particular its key parameters in Section 2.2. Its stationary phase diagram is explored in Section 2.3, by means of Monte Carlo dynamical simulations, both for our active system and its equilibrium counterpart (that we properly define). A variety of patterned phases emerge in some regions of our parameter space. The subsequent mean-field analysis of Section 2.4 allows us to understand the phase boundaries of the phase diagram given by our simulations. This very good qualitative (and good quantitative) agreement between the solution of the mean-field partial differential equations (PDE) and dynamical simulations suggests that the mean-field approach might also prove powerful to describe the physical nature of our patterned phases. Thus, in Section 2.5, we embark into a linear and a nonlinear analysis of these equations, which allows us to describe the pattern content of our physical problem. Particular emphasis is placed on the extra mathematical difficulty of dealing with a conserved mode in a pattern forming system, a question that was hitherto sidelined in the existing literature of active inclusions in membranes [RBL05b; RBL05a]. As it will turn out, this is the existence of the conserved mode (expressing that particles are conserved, regardless of their internal spin state) that gives birth to a rich phenomenology of patterns. Our analysis of such patterns will draw from recent theoretical work [Rie92a; MC00; CM03; Win06]. In our final two sections, we discuss the role of the nonequilibrium drive in producing patterned phases. To this end we introduce, in Section 2.6, a model that interpolates between the active system and its equilibrium counterpart. This allows us to probe the robustness of patterns with respect to a partial restoration of reversibility (via tunable coupling to the same thermal bath the particles and the field are in contact with). To further pinpoint at the microscopic level the processes by which entropy is created in our active system, we establish a spatial map of entropy production that we superimpose to the patterns we obtain. The various regimes observed throughout our simulations can be reasonably rationalized using this versatile entropy production as a quantitative indicator. This last piece of our analysis can be found in Section 2.7.

2.2 Model

The first ingredient of our model is a fluctuating field ϕ standing for the surrounding medium in which our particles are embedded. Our analysis is confined to a two-dimensional medium. We choose to use a free field with a Gaussian Hamiltonian endowed with the following features: the value of the field at rest and without particles is 0, and the field has a finite correlation length ξ . The Hamiltonian of the field then reads

$$H_0 = \int d^2x \left[\frac{r}{2} \phi^2 + \frac{c}{2} (\nabla \phi)^2 \right], \quad (2.1)$$

with $\xi = \sqrt{c/r}$. We assume the medium is in contact with a thermostat at temperature T . We further assume a separation of scales between the medium constituents and the particles, so that the medium can be described by a continuous field on a continuous space. However we retain the individual localized nature of the particle which we describe by their position \mathbf{r}_k . The value $\phi(\mathbf{r}_k)$ of the field at the position \mathbf{r}_k of particle k is elastically constrained to the value $\pm\phi_0$ by the internal degree of freedom $S_k = \pm 1$ of the particle. This leads us to use the following interaction energy between N particles and the field

$$H_{\text{int}} = \sum_{k=1}^N \frac{B}{2} (\phi(\mathbf{r}_k) - S_k \phi_0)^2, \quad (2.2)$$

where B is the strength of the particle-field coupling. Note that, as discussed in the introduction, particles experience no direct interactions (not even hard-core repulsion). The Ising spin variable S_k refers to the two internal states the particle is assumed to be found in. More realistic models will of course be system-dependent. For instance, to describe conically shaped proteins that locally constrain lipid membrane curvature, a Helfrich Hamiltonian [Hel73] should be used instead of Eq. (2.1). A description of the membrane thickness with the Landau-Ginzburg Hamiltonian (2.1) is perhaps better adapted to the description of protein-protein interactions experiencing hydrophobic mismatch interactions and coarse-grained packing interactions, already existing in pure one-component lipid bilayer [WBS09b]. Once energy functions are specified, we turn to the question of how to implement dynamical evolution. Regarding the background field itself, discarding possible conservation laws or hydrodynamic interactions (either or both could prove relevant in a variety of physical systems), we resort to a purely relaxational dynamics consistent with the contact to a thermal bath at temperature T :

$$\partial_t \phi(\mathbf{x}, t) = -\Gamma \frac{\delta H}{\delta \phi(\mathbf{x}, t)} + \sqrt{2\Gamma T} \zeta(\mathbf{x}, t), \quad (2.3)$$

$$\langle \zeta(\mathbf{x}, t) \zeta(\mathbf{x}', t') \rangle = \delta(\mathbf{x} - \mathbf{x}') \delta(t - t'), \quad (2.4)$$

where $H = H_0 + H_{\text{int}}$, Γ is a mobility coefficient, T is the temperature in energy units and $\zeta(\mathbf{x}, t)$ a Gaussian white noise with zero average. As far as particles are concerned,

their (low Reynolds) motion is described by an overdamped Langevin equation:

$$\frac{d\mathbf{r}_k}{dt} = -\mu \frac{\partial H}{\partial \mathbf{r}_k} + \sqrt{2\mu T} \boldsymbol{\xi}_k(t), \quad (2.5)$$

$$\langle \xi_k^\alpha(t) \xi_\ell^\beta(t') \rangle = \delta_{\alpha\beta} \delta_{k\ell} \delta(t - t'), \quad (2.6)$$

where μ is a mobility coefficient, and the $\xi_k^\alpha(t)$ are the components of independent Gaussian white noises with zero average. We use the simplifying assumption that $\boldsymbol{\xi}_k$ and ζ are independent. So far, at fixed spin variables, our dynamics is consistent with detailed balance. The nonequilibrium drive will arise from the dynamics the spins are endowed with. With an external source of energy (such as photons or ATP in biological systems) in mind, we introduce temperature and state independent flipping rates α and γ :

$$S_k = -1 \xrightleftharpoons[\gamma]{\alpha} S_k = +1. \quad (2.7)$$

For the purpose of benchmarking genuinely nonequilibrium effects, we shall later introduce a detailed-balance preserving spin-flip dynamics. The final simplifying step is to work in terms of dimensionless parameters. We introduce a characteristic size a which will be used to spatially discretize the field ϕ , we normalize energies by T , times by $a^2/(\Gamma c)$ and we absorb c in a redefinition of the field ϕ . We thus carry out the replacements $\mathbf{x}/a \rightarrow \mathbf{x}$, $\Gamma c t/a^2 \rightarrow t$, $c\phi^2/T \rightarrow \phi^2$, $c\phi_0^2/T \rightarrow \phi_0^2$, $a^2 r/c \rightarrow r$, $B/c \rightarrow B$, $T\mu/(\Gamma c) \rightarrow \mu$, $a^2\alpha/(\Gamma c) \rightarrow \alpha$ and $a^2\gamma/(\Gamma c) \rightarrow \gamma$. In a nutshell, rescaling time, space, fields and constants boils down to $a = c = T = \Gamma = 1$. Our model being now defined, we present the results of our numerical Monte Carlo-based exploration of its properties.

2.3 Numerical simulations

We perform Monte Carlo dynamical simulations on a two dimensional square lattice of size $L_x \times L_y$ with periodic boundary conditions. The Gaussian field is defined on each site (i, j) and takes continuous real values ϕ_{ij} . The field ϕ evolves according to the explicit stochastic Euler scheme corresponding to the dimensionless form of Eq. (2.3):

$$\begin{aligned} \phi_{ij}(t + \Delta t) = & \phi_{ij}(t) - \Delta t \left[r \phi_{ij}(t) - \nabla^2 \phi_{ij}(t) \right. \\ & \left. + B \sum_{k=1}^N (\phi_{\mathbf{r}_k}(t) - S_k \phi_0) \right] + G(0, 2\Delta t), \end{aligned} \quad (2.8)$$

where the discrete Laplacian is defined as

$$\nabla^2 \phi_{ij} \equiv \phi_{i+1,j+1} + \phi_{i-1,j} + \phi_{i,j+1} + \phi_{i,j-1} - 4\phi_{ij}, \quad (2.9)$$

$\mathbf{r}_k \equiv (i_k, j_k)$ being the position of the particle k on the lattice, and $G(0, 2\Delta t)$ being a Gaussian variable of mean 0 and variance $2\Delta t$.

At each time step, we update the field, and then the particles' positions. The particles lie on the lattice sites. Since our model involves non-interacting particles, we a priori allow

for several particles to occupy the same lattice site. We implement a tower sampling algorithm [Kra06] to choose what action a particle should do, namely, either jump on a neighboring site, or stay on the same site or flip its spin. The total energy variation when the particle k moves from site (i_k, j_k) to (i'_k, j'_k) is given by

$$\Delta H_{r_k \rightarrow r'_k} = \frac{B}{2}(\phi_{i'_k, j'_k} - \phi_{i_k, j_k})(\phi_{i'_k, j'_k} + \phi_{i_k, j_k} - 2\phi_0 S_k). \quad (2.10)$$

The following jump probability $P_{(i_k, j_k) \rightarrow (i'_k, j'_k)}$ between times t and $t + \Delta t$ implements a discrete version of the Langevin equation (2.5):

$$P_{(i_k, j_k) \rightarrow (i'_k, j'_k)} = \mu \Delta t \exp\left(-\frac{\Delta H_{r_k \rightarrow r'_k}}{2}\right). \quad (2.11)$$

According to our model, the spin flip probability of particle k , P_k^f , is fixed by the rates α and γ , except when we consider detailed-balance preserving flipping rates for the purpose of comparison to the out-of-equilibrium case. Each case will be specified below. We take Δt small enough to ensure that the probabilities verify

$$\sum_{(i'_k, j'_k)} P_{(i_k, j_k) \rightarrow (i'_k, j'_k)} + P_k^f < 1, \quad (2.12)$$

then the probability P_k^n that particle k neither jumps nor flips is given by $P_k^n = 1 - [\sum_{(i'_k, j'_k)} P_{(i_k, j_k) \rightarrow (i'_k, j'_k)} + P_k^f]$. We take $\Delta t = 2 \times 10^{-5}$.

2.3.1 Equilibrium benchmark

Though we are mostly interested in the active system, for the purpose of discussion and comparison we first study the system with spin flips that preserve the detailed balance condition. This is useful to sort out generic collective phenomena already present in our equilibrium Hamiltonian from those induced by activity. In this equilibrium benchmark system, the probability of a spin flip, say from spin up to spin down, between t and $t + \Delta t$ is

$$P_k^f(\uparrow \rightarrow \downarrow) = \eta \Delta t \exp\left(-\frac{H_{k\downarrow} - H_{k\uparrow}}{2}\right), \quad (2.13)$$

where η is an inverse time-scale and where $H_{k\uparrow}$ (resp. $H_{k\downarrow}$) refers to the energy of the system when spin k is up (resp. down).

When endowed with this equilibrium reversible dynamics the particles+field system already displays a nontrivial phase diagram explored with dynamical Monte Carlo simulations (see Fig. 2.1). When the coupling B with the field is small, a paramagnetic fluid (the average value of the spins is zero) is observed. When the coupling is increased, the system displays a paramagnetic-ferromagnetic transition. When the density is small, further increasing the coupling yields a phase separation between a paramagnetic gas and a ferromagnetic liquid (Fig. 2.1c). As a consistency check, we verified that the equilibrium phase diagrams do not depend on dynamical parameters. The specific simulations shown in Fig. 2.1 were performed with $\mu = 5$, $\eta = 1$.

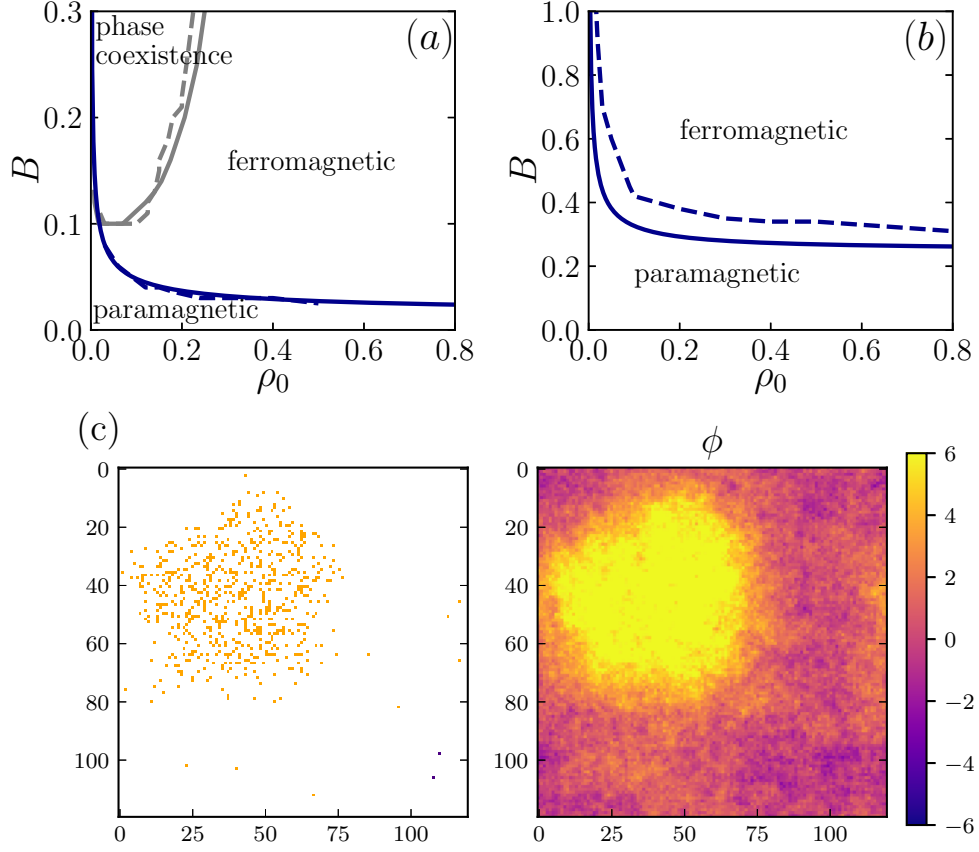


Figure 2.1 – Phase diagram (a) and (b), and snapshot (c) of the equilibrium system. (a) $r = 0.01$, $\phi_0 = 8$. (b) $r = 0.01$, $\phi_0 = 2$. Solid lines: mean-field predictions for the paramagnetic–ferromagnetic transition (blue) and for the binodal curve of the phase separation (gray). The corresponding dashed lines are the frontiers given by the Monte Carlo simulations. Phase coexistence is achieved for larger values of B out of the range of the plot. (c) Snapshot of the particle positions (left) and the corresponding underlying field ϕ (right) in the phase coexistence region for $r = 0.01$, $B = 0.26$, $\phi_0 = 8$, $\rho_0 = 0.05$. In the left snapshot, spin up particles are in yellow, spin down particles are in purple.

2.3.2 Active system

In the active system, the flipping probabilities corresponding to Eq. (2.7) are given by

$$P_k^f = \begin{cases} \gamma\Delta t & \text{if } S_k = +1 \\ \alpha\Delta t & \text{if } S_k = -1. \end{cases} \quad (2.14)$$

If flipping rates are symmetric ($\alpha = \gamma$) the average magnetization is zero and the system cannot develop a homogeneous ferromagnetic state. In the asymmetric case, it is convenient to define the total flip rate $\omega = \alpha + \gamma$ and the mean fraction $s = \alpha/\omega$ of spin-up particles in steady state. The flipping rates are thus given by $\alpha = s\omega$ and $\gamma = (1 - s)\omega$.

In the following, we explore the phase diagram of the system for $s = 1/2$ (Fig. 2.2, top). When the coupling B to the field is weak, the system remains homogeneous (and paramagnetic). At low densities, when increasing B , finite size clusters of both magnetization appear (see Fig. 2.3a). At higher densities, the phenomenology becomes richer. Increasing B from the homogeneous phase, macroscopic stripes of both magnetization (Fig. 2.3b) are observed. As B is further increased, the stripes harbor the continuous nucleation of small lumps of particles of opposite magnetization (Fig. 2.3c). These lumps grow, drift, then merge with adjacent bands of same magnetization. Increasing B again, the proliferation of lumps leads to a system of micro-clusters (Fig. 2.3d). In the patterned phase (stripes or clusters), increasing the flipping frequency ω yields local mixing of the spins, which results in the homogeneization of the whole system (Fig. 2.4, top).

If now asymmetric flipping rates ($s \neq 1/2$) are considered, the phase diagram features similar transitions. The homogeneous phase is however ferromagnetic since the mean number of spins up and spins down is different. In addition, because of the breaking of the up-down symmetry, hexagonal patterns can be observed (see Fig. 2.5). In the following section, we work out a mean-field analysis which predicts the transition between different regimes. The appearance of lumps lies at the transition between two different pattern forming regimes.

2.4 Mean-field behavior

2.4.1 Equilibrium free energy

We briefly treat the equilibrium case where particles are allowed to flip while respecting detailed balance (equilibrium benchmark). Our goal is to determine the phase diagram of the system. We first identify a conserved field, $\rho = \rho^+ + \rho^-$, and a non conserved field $\psi = \rho^+ - \rho^-$. From the Hamiltonian H , we write down a mean-field free energy density:

$$f_{\text{MF}} = \frac{r}{2}\phi^2 + B\frac{\rho^+ + \psi}{4}(\phi - \phi_0)^2 + B\frac{\rho^- - \psi}{4}(\phi + \phi_0)^2 \\ + \frac{\rho^+ + \psi}{2} \ln \frac{\rho^+ + \psi}{2} + \frac{\rho^- - \psi}{2} \ln \frac{\rho^- - \psi}{2}, \quad (2.15)$$

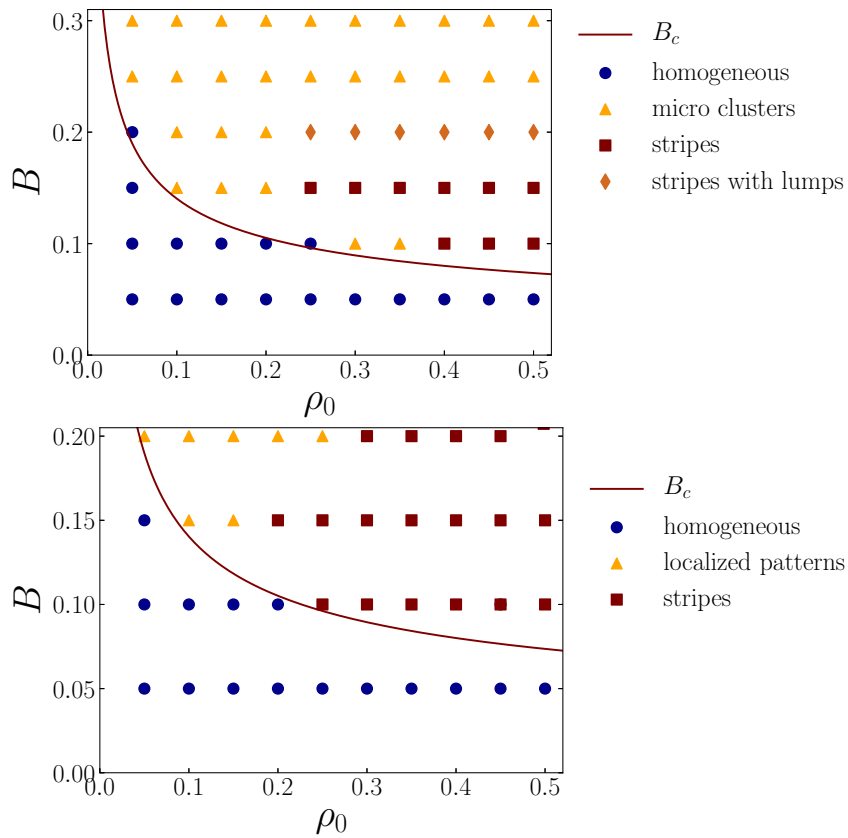


Figure 2.2 – Top: Monte Carlo phase diagram in space (ρ_0, B) in the nonequilibrium steady-state. **Bottom:** Solved-PDE (Sec. 2.4.3) phase diagram in space (ρ_0, B) . Parameters: $r = 0.01$, $\phi_0 = 8$, $\mu = 5$, $s = 1/2$ and $\omega = 0.2$. Solid burgundy line: pattern apparition threshold determined from a linear stability analysis (see Eq. (2.40)).

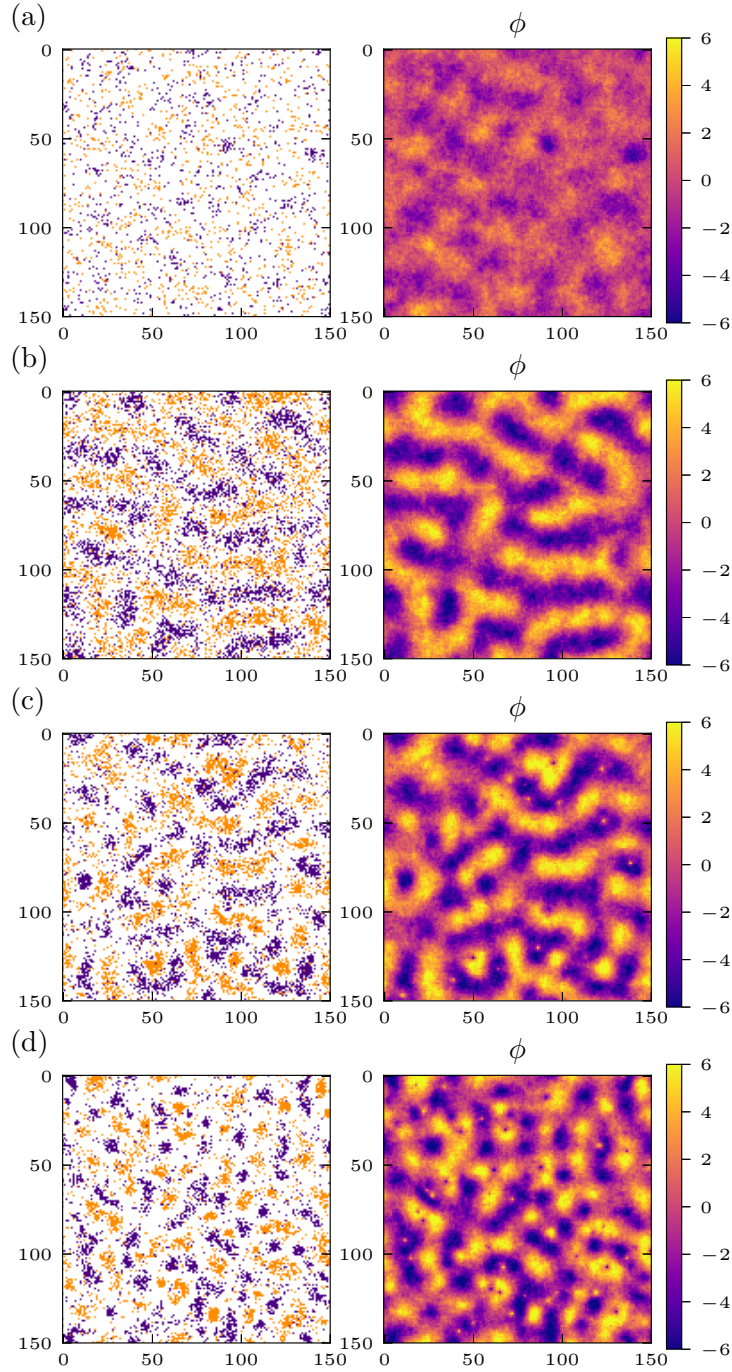


Figure 2.3 – Snapshots of the system corresponding to points in the phase diagram (ρ_0, B) shown in Fig. 2.2. In the left snapshots, spin up particles are in yellow, spin down particles are in purple. Parameters: same as in Fig. 2.2. (a) $\rho_0 = 0.1, B = 0.2$: micro clusters. (b) $\rho_0 = 0.4, B = 0.15$: stripes. (c) $\rho_0 = 0.4, B = 0.20$: stripes with lumps. (d) $\rho_0 = 0.4, B = 0.25$: unstructured stripes, micro clusters.

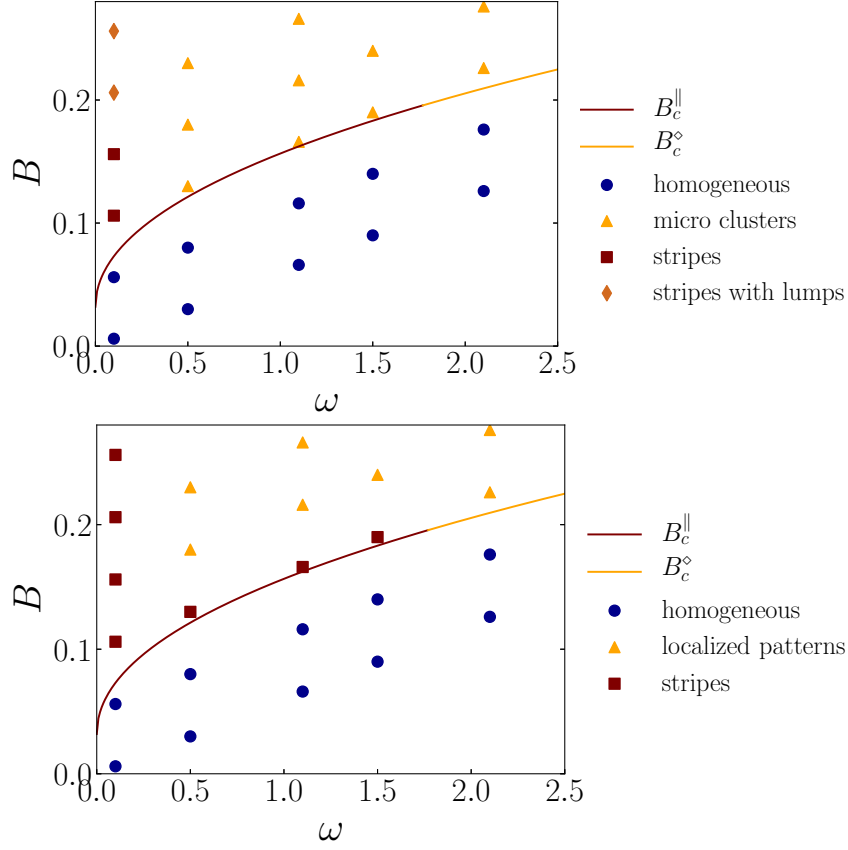


Figure 2.4 – Top: Monte Carlo phase diagram in space (ω, B) in the nonequilibrium steady-state. **Bottom:** Solved-PDE (Sec. 2.4.3) phase diagram in space (ω, B) . Parameters: $r = 0.01$, $s = 1/2$, $\rho_0 = 0.3$, $\phi_0 = 8$, $\mu = 5$. Solid burgundy line: pattern apparition threshold computed from linear stability analysis (see Eq. (2.40) in the section on the patterns analysis). Weakly nonlinear analysis predicts that rolls are stable to squares close to B_c^{\parallel} . Solid yellow line: pattern apparition threshold computed from linear stability analysis (see Eq. (2.40)). Weakly nonlinear analysis predicts that squares are stable to rolls close to B_c^{\diamond} . Rolls become unstable to squares at $(\omega, B) = (1.77, 0.1956)$ for $\rho_0 = 0.3$ (see Sec. 2.5.3).

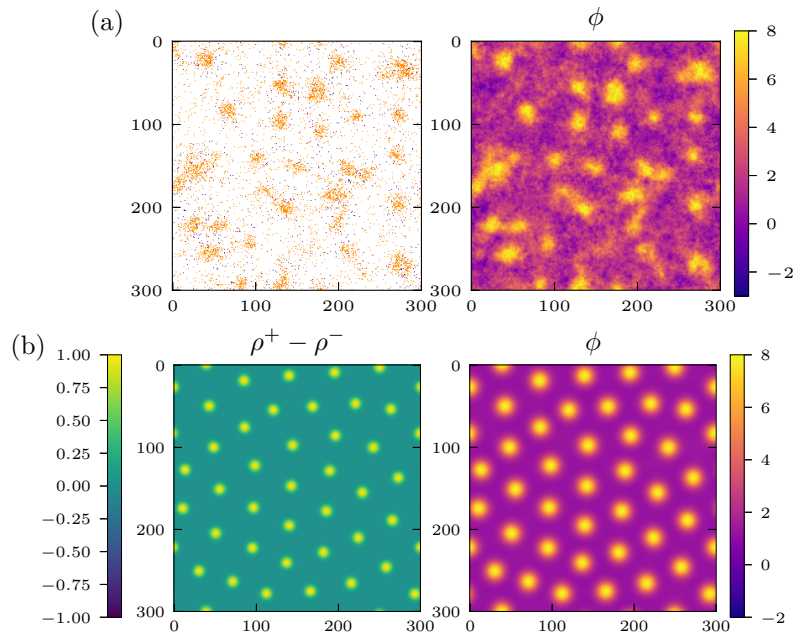


Figure 2.5 – Snapshots of (a) Monte Carlo simulation, (b) PDEs solution, in the strongly asymmetric case ($s = 0.9$) in the nonequilibrium steady-state. In the top-left snapshot, spin up particles are in yellow, spin down particles are in purple. The PDEs solution exhibit stable hexagonal pattern which is partly destroyed in the Monte Carlo simulation. See Sec. 2.4.3 for details on the mean field solution. Parameters: $r = 0.02$, $B = 0.16$, $\rho_0 = 0.1$, $\phi_0 = 10$, $\mu = 5$, $\omega = 0.25$, $s = 0.9$, and $N = 9000$ in the Monte Carlo simulation.

where the first three terms are directly inferred from the energy functional H , while the last two ones reflect the particles' entropy. Since ρ is the only conserved quantity, we minimize f_{MF} with respect to ϕ and ψ . We obtain $\phi = B\phi_0\psi/(r+B\rho)$ and $\psi = \rho \tanh(B\phi_0\phi)$. This imposes a self-consistent equation on $\phi = B\phi_0\rho \tanh(B\phi_0\phi)/(r+B\rho)$ similar to what is obtained for the magnetization in the Ising model. Searching for homogeneous phases, yields either $\phi = 0$ (paramagnetic phase), or $\phi \neq 0$ (ferromagnetic phase). At low values of B , the system is uniform and there is a continuous paramagnetic–ferromagnetic transition at $B_c^{(\text{MF})} = (1 + \sqrt{1 + 4r\phi_0^2/\rho})/(2\phi_0^2)$. At higher values of B , we numerically solve the double tangent construction on $f_{\text{MF}}(\rho)$ (already minimized with respect to ψ and ϕ). The system undergoes a phase separation between a low density paramagnetic phase and a high density ferromagnetic phase. These mean-field predictions correspond to the continuous lines of Fig. 2.1 while the results of the Monte Carlo simulations are indicated by the dashed lines. We have checked that the agreement is all the better as we are working at large ϕ_0 .

2.4.2 Mean field dynamics

We consider now the original model of interest where flips are fixed by an external and independent source of energy. Out of equilibrium, we can no longer rely on the free energy to construct the phase diagram. Since particles execute Brownian motions, we consider the noiseless limit of the Dean–Kawasaki equations [Dea96] for the up and down particle densities. Taking spin exchange into account (and neglecting the corresponding Poisson

noise as well), we arrive at the deterministic evolution equations for ρ^\pm :

$$\partial_t \rho^+ = \mu \nabla \cdot [\rho^+ \nabla \frac{\partial f_{\text{MF}}}{\partial \rho^+}] + \alpha \rho^- - \gamma \rho^+, \quad (2.16)$$

$$\partial_t \rho^- = \mu \nabla \cdot [\rho^- \nabla \frac{\partial f_{\text{MF}}}{\partial \rho^-}] - \alpha \rho^- + \gamma \rho^+ \quad (2.17)$$

$$\partial_t \phi = \nabla^2 \phi - r \phi - B \rho^+ (\phi - \phi_0) - B \rho^- (\phi + \phi_0). \quad (2.18)$$

It will prove convenient to write these equations in terms of the conserved field ρ , and of the non-conserved field ψ . We also parametrize the rates α and γ by means of $\omega = \alpha + \gamma$ and $s = \alpha/\omega$ (the latter being the steady-state fraction of spin up particles). The dynamical evolutions of the fields then read

$$\partial_t \rho = \mu \nabla^2 \rho + \mu B \nabla \cdot [(\rho \phi - \psi \phi_0) \nabla \phi], \quad (2.19)$$

$$\begin{aligned} \partial_t \psi = \mu \nabla^2 \psi + \mu B \nabla \cdot [(\psi \phi - \rho \phi_0) \nabla \phi] \\ - \omega \psi + (2s - 1) \omega \rho, \end{aligned} \quad (2.20)$$

$$\partial_t \phi = \nabla^2 \phi - r \phi - B \rho \phi + B \phi_0 \psi. \quad (2.21)$$

These three equations are the starting point of our analysis of the patterns that form in the steady-state of our system. It is important to note that $s = \frac{1}{2}$ will play a special role because then these equations are invariant upon the up-down symmetry $(\rho, \psi, \phi) \rightarrow (\rho, -\psi, -\phi)$. Before we embark in a detailed analytical study of their pattern content, we begin with a numerical solution of these nonlinear coupled PDEs.

2.4.3 Numerical solution of the coupled partial differential equations

We shall show that the numerical solution of the nonlinear coupled PDEs (which are noiseless) is relevant to analyze the stochastic simulations to the extent that phases and phase boundaries are quite faithfully captured. The coupled PDEs are solved on a lattice of size $L_x \times L_y = 150 \times 150$. The three fields ρ^+ , ρ^- and ϕ are discretized in time and space; an explicit Euler scheme to update the three fields is implemented. The explicit Euler scheme is easy to implement and it converges in the domains of the phase diagram we are interested in. Our discretized equations take the following form:

$$\begin{aligned} \rho_{ij}^+(t + \Delta t) = \rho_{ij}^+(t) + \Delta t \Bigg[& \mu \nabla^2 \rho_{ij}^+ \\ & + \mu B \nabla_x (\rho_{ij}^+ (\phi_{ij} - \phi_0) \nabla_x \phi_{ij}) \\ & + \mu B \nabla_y (\rho_{ij}^+ (\phi_{ij} - \phi_0) \nabla_y \phi_{ij}) \\ & - \gamma \rho_{ij}^+ + \alpha \rho_{ij}^- \Bigg] (t), \end{aligned} \quad (2.22)$$

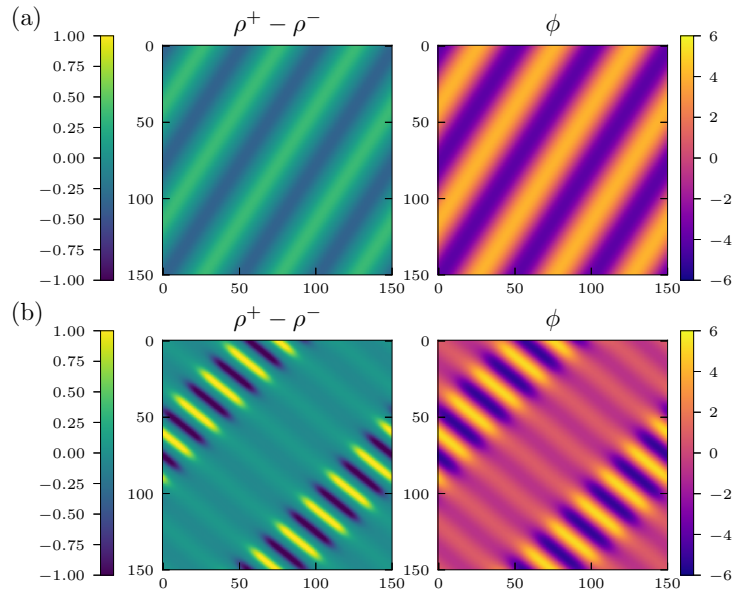


Figure 2.6 – (a) Snapshot of PDEs solution with $\omega = 0.1$ and $B = 0.106$. (b) Snapshot of PDEs solution with $\omega = 0.5$ and $B = 0.18$. In (a) we observe extended stripe-like patterns, while in (b) pattern localization occurs in the direction transverse to the stripes. Parameters: $r = 0.01$, $\rho_0 = 0.3$, $\phi_0 = 8$, $\mu = 5$, $s = 1/2$.

$$\begin{aligned} \phi_{ij}(t + \Delta t) = & \phi_{ij}(t) + \Delta t \left[\nabla^2 \phi_{ij} - r \phi_{ij} \right. \\ & - B \rho_{ij}^+(\phi_{ij} - \phi_0) \\ & \left. - B \rho_{ij}^-(\phi_{ij} + \phi_0) \right](t), \end{aligned} \quad (2.23)$$

and the discretized equation on ρ^- is formally identical to the discretized equation on ρ^+ up to the exchange $\rho^+ \leftrightarrow \rho^-$, $\phi_0 \rightarrow -\phi_0$, $\alpha \leftrightarrow \gamma$. The discrete spatial derivatives of any field g_{ij} are defined as

$$\nabla_x g_{ij} \equiv \frac{1}{2}(g_{i+1,j} - g_{i-1,j}), \quad (2.24)$$

$$\nabla_y g_{ij} \equiv \frac{1}{2}(g_{i,j+1} - g_{i,j-1}), \quad (2.25)$$

and the Laplacian has already been defined in Eq. (2.9). We confirm that different initial conditions lead to same stationary density profiles. We check the conservation of total density, namely $(L_x L_y)^{-1} \sum_{ij} \rho_{ij} = \rho_0$, along with the positivity of ρ^+ and ρ^- on each site.

To ease comparison of the PDE solution with the Monte Carlo simulation, the PDE phase diagram is plotted Fig. 2.4 (bottom) for the same physical parameters as those of the Monte Carlo results of Fig. 2.4 (top). The results of the PDEs numerical solution match the results of the Monte Carlo simulations. The solution of the PDEs is also in good agreement with the predictions obtained from a weakly nonlinear analysis in Section 2.5.2: we can observe either homogeneous patterns (Fig. 2.6, top), or spatially localized patterns (Fig. 2.6, bottom), depending on the parameters. The coming section is devoted to an analysis of these patterns.

2.5 Pattern analysis

2.5.1 Linear stability analysis

By resorting to a linear stability analysis (LSA), the range of parameters for which a uniform stationary state is destabilized can be found. While LSA tells us about the first unstable mode, the question of which are the selected modes that eventually build up into patterns requires a full analysis of the nonlinear equations. The homogeneous and stationary solution to Eqs. (2.19), (2.20), (2.21) is characterized by the following values of the fields

$$\rho_h = \rho_0, \quad (2.26)$$

$$\psi_h = (2s - 1)\rho_0, \quad (2.27)$$

$$\phi_h = (2s - 1)\frac{B\rho_0}{\tilde{r}}\phi_0, \quad (2.28)$$

with

$$\tilde{r} = r + B\rho_0 = \tilde{\xi}^{-2} \quad (2.29)$$

where $\tilde{\xi}$ is the renormalized correlation length of the field ϕ . We set $\rho_1 = \rho - \rho_h$, $\psi_1 = \psi - \psi_h$ and $\phi_1 = \phi - \phi_h$ and we expand Eqs. (2.19), (2.20), (2.21) to linear order in the ρ_1 , ϕ_1 , ψ_1 fields. We expand the fields in Fourier modes $\sim e^{i\mathbf{k}\cdot\mathbf{x}}$ and we arrive at a linear system for the Fourier components $\partial_t(\rho_1, \psi_1, \phi_1)^T = M(\rho_1, \psi_1, \phi_1)^T$ with

$$M = \begin{pmatrix} -\mu k^2 & 0 & -\mu B\rho_0\phi_0(2s-1)(B\rho_0/\tilde{r}-1)k^2 \\ (2s-1)\omega & -\mu k^2 - \omega & -\mu B\rho_0\phi_0[(2s-1)^2 B\rho_0/\tilde{r} - 1]k^2 \\ -B^2\rho_0\phi_0(2s-1)/\tilde{r} & B\phi_0 & -k^2 - \tilde{r} \end{pmatrix}, \quad (2.30)$$

with $k = \|\mathbf{k}\|$. The eigenvalues of M can be shown to be always real which excludes oscillating patterns close to the threshold. We denote them by σ_i , with $\sigma_1 < \sigma_2 < \sigma_3$. Solving $\det M(k) = 0$ yields the modes for which temporal growth is marginal. In practice, we have $\det M = -\mu^2 k^2 Q(k^2)$, where $Q(X) = X^2 + q_1 X + q_2$ is degree 2 polynomial, with

$$q_1 = \frac{\omega}{\mu} + \tilde{r} - B^2\rho_0\phi_0^2 + \frac{B^3\rho_0^2\phi_0^2(2\tilde{r} - B\rho_0)(1-2s)^2}{\tilde{r}^2}, \quad (2.31)$$

$$q_2 = \frac{\omega}{\mu\tilde{r}^2} (\tilde{r}^3 - B^2\rho_0r^2\phi_0^2(1-2s)^2). \quad (2.32)$$

Three different physical cases must be distinguished, depending on the roots X_- , X_+ of Q .

- case (i): $q_1 \geq 0$ and $q_2 \geq 0$, or $q_2 < q_1^2/4$, then Q has no real positive roots. One can show that the three eigenvalues of M are negative: the homogeneous state is stable.
- case (ii): $q_2 < 0$ then Q has only one positive root X_+ . We set $k_+ \equiv X_+^{1/2}$. In this regime, unstable modes go from $k = 0$ to $k = k_+$ and we numerically observe either

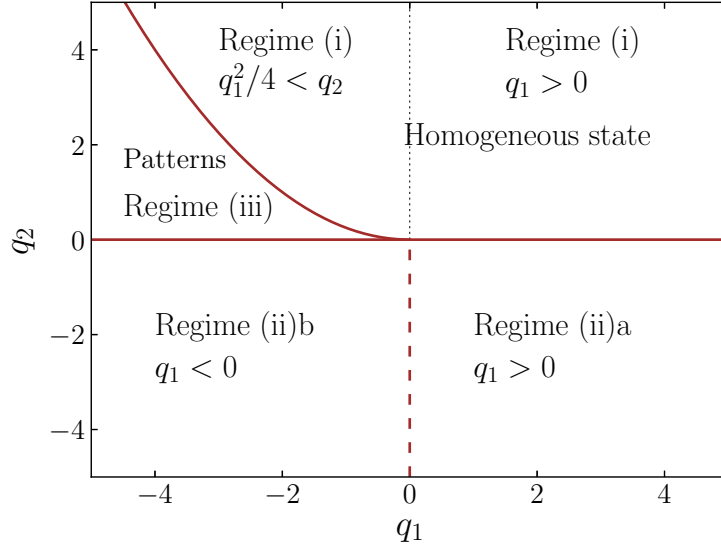


Figure 2.7 – Phase diagram from the linear stability analysis in space (q_1, q_2) . Solid brown line: boundaries between domains given by the LSA. Dashed brown: boundary from numerical solution of the PDEs. When $\omega = 0$ we observe coarsening if $q_1 < 0$ and a stable homogeneous state if $q_1 > 0$. Regime (i): the homogeneous state is stable. Regime (ii)a: we numerically observe coarsening. Regime (ii)b: we numerically observe pattern formation. In both regimes (ii)a and (ii)b, the LSA predicted unstable modes down to $k \rightarrow 0$, yet the system behavior can be very different from (ii)a to (ii)b. Regime (iii): finite wavelength patterns at stability threshold.

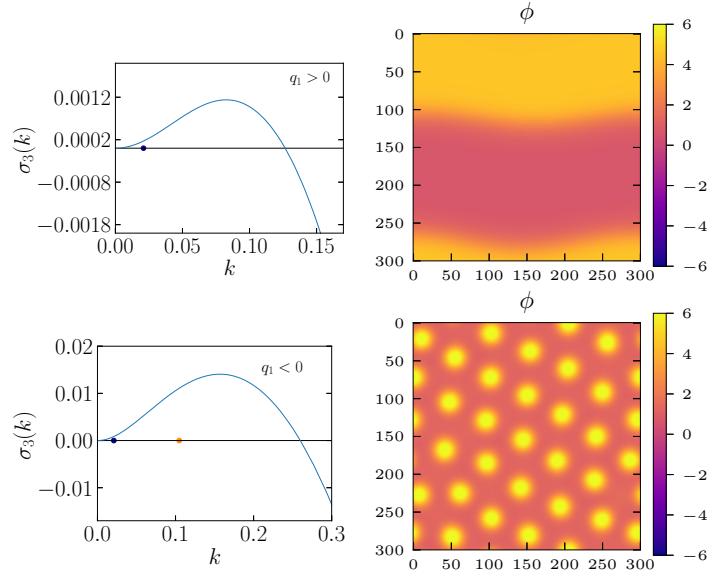


Figure 2.8 – Larger eigenvalue $\sigma_3(k)$ in regime (ii)a (top left) and regime ii(b) (bottom left), and the corresponding solution of the PDEs (right). In the left part, the other eigenvalues are strictly negative and are out of range of the plot. Blue dot: minimal wavenumber $k_{\min} = 2\pi/L$ sampled in the simulation. The instability is correctly captured in both cases. While the linear stability analysis gives similar results in both cases, the solution of PDEs (right column) shows coarsening in one case, and pattern formation in the other case. Parameters: $r = 0.02$, $B = 0.16$, $\rho_0 = 0.1$, $\phi_0 = 9$, $\mu = 5$, $s = 0.9$. **Top:** $\omega = 10\omega_c$. **Bottom:** $\omega = 0.5\omega_c$. Critical value ω_c defined in eq. (2.38).

coarsening, or pattern formation depending on the sign of q_1 , as shown in Fig. 2.8. When ω is non zero, we sit in regime (ii) where $q_2 < 0$ is equivalent to

$$(2s - 1)^2 > \frac{1}{B\phi_0^2} \left(1 + \frac{B\rho_0}{r}\right)^2 \left(1 + \frac{r}{B\rho_0}\right), \quad (2.33)$$

which surprisingly does not depend upon the dynamical parameters. Physically, the instability comes from the frustrated field ϕ whose value at rest and without particles is 0, different from ϕ_h in the presence of particles with non-symmetric flipping rates. This regime is referred to as type II_s in [CH93].

- case (iii): $q_1^2/4 \geq q_2 > 0$; patterns appear at finite wavelength (referred to as type I_s in [CH93]). We have $X_-, X_+ > 0$ and we set $k_{\pm} \equiv X_{\pm}^{1/2}$. The eigenvalue $\sigma_3(k)$ is positive for $k \in [k_-, k_+]$. At the onset of instability, the only growing mode is indexed by k_c with, at the threshold, $k_c = k_- = k_+$.

Note also that when $\omega = 0$ we observe an equilibrium coarsening of the two populations of particles, under the condition $q_1 < 0$ (which is equivalent to sitting in the equilibrium ordered phase).

In summary, (ii) and (iii) are the two regimes where the homogeneous state is destabilized. For nonzero flipping rates, the only way to transition from regime (i) to regime (ii), or from regime (iii) to (ii), is by changing the equilibrium parameters, namely r , B , ρ_0 , ϕ_0 and s . By contrast, at fixed equilibrium parameters, we transition from regime (i) to regime (iii) by changing ω or μ . In the following, we will focus on the transition caused by a change in the dynamics, and consequently, on instabilities starting at finite wavelength.

We begin our analysis with the simpler $s = 1/2$ symmetric case, where the number of particles of each spin is identical in the steady-state. This ensures, after Eq. (2.33), that we are always in the pattern forming regime (iii). The matrix M is now block diagonal and eigenvalues can be cast in a compact form:

$$\sigma_1 = -\mu k^2, \quad (2.34)$$

$$\sigma_2 = \frac{1}{2} \left(-\tilde{r} - \omega - (1 + \mu)k^2 - \sqrt{\Lambda} \right), \quad (2.35)$$

$$\sigma_3 = \frac{1}{2} \left(-\tilde{r} - \omega - (1 + \mu)k^2 + \sqrt{\Lambda} \right), \quad (2.36)$$

with

$$\Lambda = [k^2(\mu - 1) + \omega - \tilde{r}]^2 + 4\mu k^2 \rho_0 B^2 \phi_0^2 > 0. \quad (2.37)$$

For the purpose of discussion we use $\omega = \alpha + \gamma$ as the control parameter. Physically, we recall that for high flipping rates, the system remains homogeneous since particles locally efficiently mix, whereas for $\omega = 0$, the system undergoes an equilibrium coarsening (see phase diagram Fig. 2.4). Solving $q_1^2 - 4q_2 = 0$ yields a critical value of ω :

$$\omega_c = \mu(B\phi_0\sqrt{\rho_0} - \sqrt{\tilde{r}})^2, \quad (2.38)$$

below which the homogeneous system is no longer stable. To study the system close to this transition, we write $\omega = \omega_c - \varepsilon^2$, where the distance to the threshold $\varepsilon^2 > 0$ becomes our control parameter. Since we sit in regime (iii), destabilization occurs at a mode $k_c = k_{\pm} > 0$ when $\varepsilon = 0$. Thus, when $\omega < \omega_c$, $\sigma_3(k) \geq 0$ for $k \in [k_-, k_+]$, with

$$k_{\pm} = \frac{\sqrt{\rho_0 B^2 \phi_0^2 - \tilde{r} - \Omega \pm \sqrt{(\rho_0 B^2 \phi_0^2 - \tilde{r} - \Omega)^2 - 4\tilde{r}\Omega}}}{\sqrt{2}}, \quad (2.39)$$

and where $\Omega = \omega/\mu$. The condition of existence of the k_{\pm} modes (namely that X_{\pm} are real) is given by

$$B\phi_0\sqrt{\rho_0} \geq \sqrt{r + B\rho_0} + \sqrt{\omega/\mu}. \quad (2.40)$$

At $\omega = \omega_c$ equality is achieved in Eq. (2.40) and this allows us to infer the critical wavelength of patterns $\lambda_c \equiv 2\pi/k_c = 2\pi(\tilde{r}\omega_c/\mu)^{-1/4}$. This suggests that close to the threshold the patterns spatial periodicity λ_p could be the combination $\lambda_p = 2\pi/k_p = 2\pi(\tilde{r}\omega/\mu)^{-1/4}$.

This prediction has been checked in simulations of a quasi 1D system of size 1000×10 to force pattern formation along one direction, hence allowing us to achieve a good precision on the wavelength. We note on Fig. 2.9 that the prediction on the pattern periodicity λ_p applies beyond the pattern formation threshold. Interestingly enough, λ_p can be expressed as the geometric mean of the renormalized correlation length $\tilde{\xi}$ of the Gaussian field ϕ in presence of inclusions and of the typical diffusion length $\ell_d \sim \sqrt{\mu/\omega}$ of a particle between two flips. The formula $\lambda_p \sim (\tilde{\xi}\ell_d)^{1/2}$, expresses, at the level of a cluster, the balance between accretion via interactions vs. loss by diffusion. It would certainly be interesting to see λ_p emerge from a handwaving argument. Finally, it is worth noticing that close to threshold the selected wavelength does not depend upon the field mobility: it is only the particles' mobility with respect to the spins' flipping rate that matters. An estimate of the diffusion time of a particle over a characteristic correlation length $\tilde{\xi}$ of the field is $t_d \approx \tilde{\xi}^2/(2\mu)$. On the other hand, the correlation time t_{ϕ} of the field over a scale $\tilde{\xi}$ is given by $t_{\phi} \approx 1/(2\tilde{r})$. Hence particles are fast with respect to the field when $t_d \ll t_{\phi}$, or $1 \ll \mu$. In Fig. 2.9, one can indeed see that the selected wavelength does not change, whether particles are slow or fast with respect to the field. We now turn to an analysis of the patterns that form beyond threshold.

2.5.2 Weakly nonlinear analysis

In order to gain insight into nonlinear effects at $s = 1/2$, we can derive an amplitude equation for the fields by extending the approach of Swift and Hohenberg [SH77]. A direct, though naive, way of proceeding would be to extract the equations for the relevant fields for which we can find modes with exponential growth. In particular, in the basis where M is diagonal, there is only one direction (corresponding to eigenvalue σ_3) along which we observe the temporal growth of the Fourier modes (see Fig. 2.10). The eigenfields are given by the LSA. By denoting $D = P^{-1}MP$ where the transformation matrix

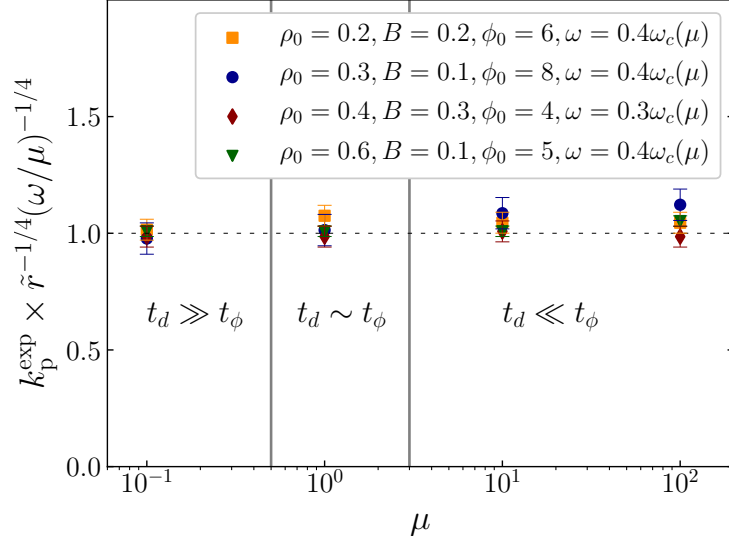


Figure 2.9 – Normalized wavenumber $k_p^{\text{exp}}(\tilde{r}\omega/\mu)^{-1/4}$ measured from the simulation as a function of the mobility μ of the particles. The wavenumber is given by the pattern wavelength and reads $k_p^{\text{exp}} = 2\pi/\lambda_p^{\text{exp}}$. Fixed parameters: $r = 0.01$, $s = 0.5$. We vary B , ϕ_0 and $\rho_0 \equiv N/(L_x L_y)$ for each simulation. We vary also μ and ω such that we always sit in the pattern forming regime. In particular, we set ω as a fraction of $\omega_c = \mu(B\phi_0\sqrt{\rho_0} - \sqrt{\tilde{r}})^2$. For $\omega = 0.3\omega_c$ the relation $k_p^{\text{exp}} = (\tilde{r}\omega/\mu)^{1/4}$ is still valid. This equality is no longer true when $\omega \lesssim 0.1\omega_c$. As μ changes from 10^{-1} to 10^2 , we sit in different regimes where the particles are slow or fast with respect to the field dynamics.

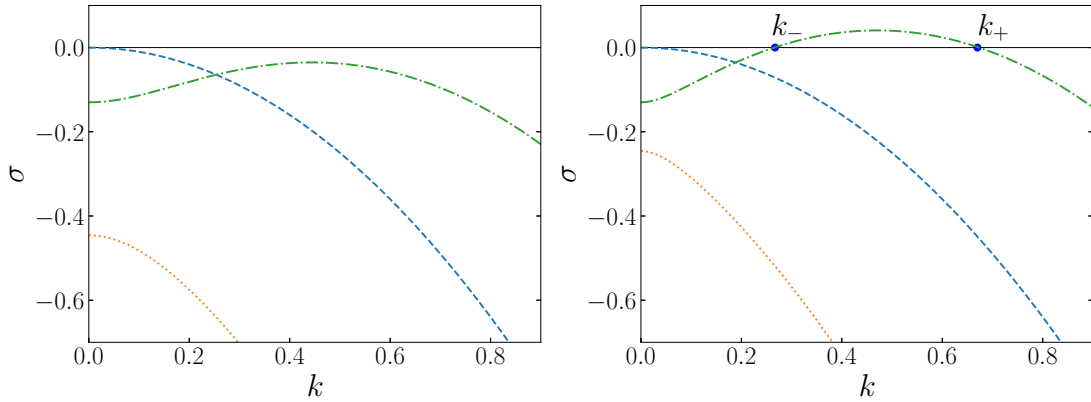


Figure 2.10 – Eigenvalues of M as a function of k in the homogeneous stable regime (left), and in the pattern forming regime (iii) (right). σ_3 is the highest eigenvalue and is positive in the pattern formation regime. **Left:** $\omega > \omega_c$. **Right:** $\omega < \omega_c$. Parameters: $r = 0.01$, $B = 0.3$, $\rho_0 = 0.4$, $\phi_0 = 5$, $\mu = 1$, $s = 0.5$.

P writes

$$P = \begin{pmatrix} 1 & 0 & 0 \\ 0 & a(k) & b(k) \\ 0 & 1 & 1 \end{pmatrix}, \quad (2.41)$$

with

$$a(k) = \frac{(1 - \mu)k^2 + \tilde{r} - \omega - \sqrt{\Lambda}}{2B\phi_0}, \quad (2.42)$$

$$b(k) = \frac{(1 - \mu)k^2 + \tilde{r} - \omega + \sqrt{\Lambda}}{2B\phi_0}, \quad (2.43)$$

we define $(U, V, W)^T = P^{-1}(\rho_1, \psi_1, \phi_1)^T$, with ρ_1 , ψ_1 and ϕ_1 which are no longer infinitesimally small perturbations. The new fields (U, V, W) now verify $U \sim e^{\sigma_1 t}$, $V \sim e^{\sigma_2 t}$ and $W \sim e^{\sigma_3 t}$. However, we have to be careful: the existence of the conserved quantity ρ implies that the mode $k = 0$ is marginal for the field U and has to be taken into account [CF85; Rie92b; MC00]. Indeed nonlinear terms couple modes $k \rightarrow 0$ with modes $k \sim k_c$ in products $O(UW)$. In the absence of a marginal growth, it would be correct to focus only on modes with exponential growth around k_c and we could expand σ_1 , σ_2 and σ_3 around $\varepsilon = 0$ and $k \sim k_c$. This would lead to neglect terms of the form $V^q W^p$ and $U^q W^p$ (for $q \geq 1$ and $p \geq 0$) since they exponentially go to 0 when $k \sim k_c$. Interestingly, one of the erroneous conclusions we would arrive at is that square patterns could never be stable, in conflict with observations of PDEs' solution. Now keeping both relevant fields U and W , the evolution equations read

$$\partial_t U = \sigma_1 U + \mathcal{N}_1(U, W), \quad (2.44)$$

$$\partial_t W = \sigma_3 W + \mathcal{N}_2(U, W), \quad (2.45)$$

where \mathcal{N}_1 and \mathcal{N}_2 are nonlinear operators that couple U and W . To lowest order in ε , we find that \mathcal{N}_1 contains terms $\sim O(W^2)$ and that \mathcal{N}_2 contains terms $\sim O(UW)$. Thus, U will saturate to $O(W^2)$, which renormalizes $O(W^3)$ terms in \mathcal{N}_2 . Of course, this previous analysis holds for the case $s = 1/2$, where equations are invariant upon the $(\rho, \psi, \phi) \rightarrow (\rho, -\psi, -\phi)$ symmetry. If $s \neq 1/2$, new terms appear in nonlinear equations (2.44) and (2.45). To lowest order, new terms in \mathcal{N}_2 will take the form $O((2s - 1)W^2)$, $O((2s - 1)^2 W)$ and $O((2s - 1)^2 W^3)$ such that the resulting equations remain consistent with the symmetry $(\rho, \psi, \phi, s) \rightarrow (\rho, -\psi, -\phi, \frac{1}{2} - s)$. These terms are directly responsible for the stability of hexagonal patterns [CM03] as confirmed in the numerical simulations (see Fig. 2.5). We are now going to derive, in a pragmatic fashion, the amplitude equations for the fields when $s = 1/2$. Our derivation is inspired by the methods presented in [Win06].

We sit in the regime where patterns appear and we ask what the selected patterns beyond threshold are? Weakly nonlinear analysis begins by noticing that $\sigma_3 \sim \varepsilon^2 - a(k_c^2 - k^2)^2$, above the pattern threshold. We work in units of the the slow time scale by defining $T = \varepsilon^2 t$; similarly in units of the large wavelength scale, we set $X = \varepsilon x$ which governs the evolution of the envelope of the fast growing patterns that develop at wavenumber k_c .

The stationary homogeneous solution is perturbed when $\omega < \omega_c$. We expand the fields in a power series of the parameter ε . In the symmetric case $s = 1/2$, the stable patterns are usually rolls and squares [CM03]. To study their relative stability in two dimensions, using $\psi_h = \phi_h = 0$, the expansion for the fields reads

$$\rho = \rho_0 + \varepsilon^2 R(X, Y) + \sum_{n=1}^{\infty} \varepsilon^n \rho_n(x, y, X, Y), \quad (2.46)$$

$$\psi = \sum_{n=1}^{\infty} \varepsilon^n \psi_n(x, y, X, Y), \quad (2.47)$$

$$\phi = \sum_{n=1}^{\infty} \varepsilon^n \phi_n(x, y, X, Y), \quad (2.48)$$

with $Y = \varepsilon y$, and where $R(X, Y)$ is the large scale envelope of the marginal mode $k = 0$ that has to be added in the expansion of the conserved field with the appropriate scaling to obtain a closure relation (see [CF85; MC00]). The functions ρ_n , ψ_n and ϕ_n are expected to be products of slow dynamics envelopes and fast growing patterns. These considerations allow us to write differential operators with the chain rule, namely, $\partial_x \rightarrow \partial_x + \varepsilon \partial_X$, $\partial_y \rightarrow \partial_y + \varepsilon \partial_Y$ and $\partial_t \rightarrow \varepsilon^2 \partial_T$. Next, we expand Eq. (2.19), (2.20), (2.21) to successive orders to get a closed set of equations. In the canonical case of the Swift-Hohenberg equation [SH77; CH93], the closed relation for the lowest order amplitude is obtained to order $O(\varepsilon^3)$. In our case of existence of a conserved quantity, we have to extract field evolution up to order $O(\varepsilon^4)$ to get a closed system of equations. We are going to proceed recursively to extract the evolution of the fields. To order $O(\varepsilon)$, we find the following system:

$$\mathcal{L} \begin{pmatrix} \rho_1 \\ \psi_1 \\ \phi_1 \end{pmatrix} = 0, \quad (2.49)$$

with

$$\mathcal{L} = \begin{pmatrix} \mu \nabla^2 & 0 & 0 \\ 0 & \mu \nabla^2 - \omega_c & -\mu B \rho_0 \phi_0 \nabla^2 \\ 0 & B \phi_0 & \nabla^2 - \tilde{r} \end{pmatrix}, \quad (2.50)$$

and where $\nabla^2 = \partial_x^2 + \partial_y^2$. The solution of this system reads

$$\rho_1(x, y, X, Y) = 0, \quad (2.51)$$

$$\psi_1(x, y, X, Y) = P_1(X, Y) e^{ik_c x} + Q_1(X, Y) e^{ik_c y} + c.c., \quad (2.52)$$

$$\phi_1(x, y, X, Y) = \lambda_1 \psi_1, \quad (2.53)$$

with $\lambda_1 = B \phi_0 / (\tilde{r} + k_c^2)$ a simple scalar coefficient, P_1 and Q_1 are scalar functions of X and Y , and where *c.c.* stands for complex conjugate. To order $O(\varepsilon^2)$, the system we

arrive at is

$$\mathcal{L} \begin{pmatrix} \rho_2 \\ \psi_2 \\ \phi_2 \end{pmatrix} = \zeta^{(2)}(\rho_1, \psi_1, \phi_1) \quad (2.54)$$

with $\zeta^{(2)} = (\zeta_1^{(2)}, \zeta_2^{(2)}, \zeta_3^{(2)})^T$ a vector which only depends on first order fields. The components of $\zeta^{(2)}$ read

$$\begin{aligned} \zeta_1^{(2)} = & \mu B [\phi_0 (\psi_1 \partial_x^2 \phi_1 + \partial_x \psi_1 \partial_x \phi_1) \\ & + \phi_0 (\psi_1 \partial_y^2 \phi_1 + \partial_y \psi_1 \partial_y \phi_1) \\ & - \rho_0 (\partial_x \phi_1)^2 - \rho_0 \phi_1 \partial_x^2 \phi_1 \\ & - \rho_0 (\partial_y \phi_1)^2 - \rho_0 \phi_1 \partial_y^2 \phi_1], \end{aligned} \quad (2.55)$$

$$\zeta_2^{(2)} = 2\mu [B\rho_0\phi_0(\partial_{xX} + \partial_{yY})\phi_1 - (\partial_{xX} + \partial_{yY})\psi_1], \quad (2.56)$$

$$\zeta_3^{(2)} = -2(\partial_{xX} + \partial_{yY})\phi_1. \quad (2.57)$$

The solution of Eq. (2.54) reads:

$$\begin{aligned} \rho_2 = & \lambda_2 P_1^2(X, Y) e^{2ik_c x} + \lambda_2 Q_1^2(X, Y) e^{2ik_c y} \\ & + 2\lambda_2 P_1(X, Y) Q_1(X, Y) e^{ik_c x + ik_c y} \\ & + 2\lambda_2 P_1(X, Y) Q_1^*(X, Y) e^{ik_c x - ik_c y} + c.c., \end{aligned} \quad (2.58)$$

$$\psi_2 = P_2(X, Y) e^{ik_c x} + Q_2(X, Y) e^{ik_c y} + c.c., \quad (2.59)$$

$$\begin{aligned} \phi_2 = & \lambda_1 [P_2(X, Y) + 2ik_c \frac{\lambda_1}{\tilde{r} + k_c^2} \partial_X P_1(X, Y)] e^{ik_c x} \\ & + \lambda_1 [Q_2(X, Y) + 2ik_c \frac{\lambda_1}{\tilde{r} + k_c^2} \partial_Y Q_1(X, Y)] e^{ik_c y} \\ & + c.c., \end{aligned} \quad (2.60)$$

with $\lambda_2 \equiv -B\lambda_1(\rho_0\lambda_1 - \phi_0)/2 = \lambda_1^2(k_c^2 + r)/2$ and where Q_1^* is the complex conjugate of Q_1 . At $O(\varepsilon^3)$, we find the equation on P_1 (resp. Q_1) by collecting the terms proportional to $e^{ik_c x}$ (resp. $e^{ik_c y}$) in the two equations involving ψ_3 and ϕ_3 . A linear combination of these equations allows us to eliminate the second order amplitudes P_2 and Q_2 and to extract the time evolution on P_1 and Q_1 . To order $O(\varepsilon^3)$ we arrive at the following equations:

$$\begin{aligned} \partial_T P_1 = & a_1 P_1 + a_2 \partial_{XX} P_1 \\ & - a_3 |P_1|^2 P_1 - a_4 |Q_1|^2 P_1 - a_5 R P_1 \end{aligned} \quad (2.61)$$

$$\begin{aligned} \partial_T Q_1 = & a_1 Q_1 + a_2 \partial_{YY} Q_1 \\ & - a_3 |Q_1|^2 Q_1 - a_4 |P_1|^2 Q_1 - a_5 R Q_1 \end{aligned} \quad (2.62)$$

with

$$a_1 = \frac{\tilde{r}}{\mu k_c^2 + \tilde{r}}, \quad (2.63)$$

$$a_2 = \frac{4\mu k_c^2 \sqrt{\tilde{r}}}{B\phi_0(\mu k_c^2 + \tilde{r})\sqrt{\rho_0}}, \quad (2.64)$$

$$a_3 = \frac{B^3 \mu k_c^2 \phi_0^2 \left(B\phi_0^2 \left((k_c^2 + \tilde{r})^2 - B^2 \rho_0^2 \right) + 2(k_c^2 + \tilde{r})^2 \right)}{2(k_c^2 + \tilde{r})^2 \left(\mu k_c^2 \rho_0 B^2 \phi_0^2 + (k_c^2 + \tilde{r})^2 \right)} \quad (2.65)$$

$$a_4 = \frac{2\mu k_c^2 B^3 \phi_0^2 \left(B^2 \rho_0 \phi_0^2 (k_c^2 + r) + (k_c^2 + \tilde{r})^2 \right)}{(k_c^2 + \tilde{r})^2 \left(\mu k_c^2 \rho_0 B^2 \phi_0^2 + (k_c^2 + \tilde{r})^2 \right)}, \quad (2.66)$$

$$a_5 = -\frac{\mu k_c^2 B^2 \phi_0^2 (k_c^2 + r)}{\mu k_c^2 \rho_0 B^2 \phi_0^2 + (k_c^2 + \tilde{r})^2}. \quad (2.67)$$

To order $O(\varepsilon^4)$, we close the system with the time evolution of $R(X, Y)$, which is obtained by extracting coefficients of the mode $k = 0$ in the ρ_4 equation. We obtain

$$\begin{aligned} \partial_T R = & \mu \tilde{\nabla} R + \kappa_1 (\partial_X^2 |P_1|^2 + \partial_Y^2 |Q_1|^2) \\ & + \kappa_2 (\partial_Y^2 |P_1|^2 + \partial_X^2 |Q_1|^2), \end{aligned} \quad (2.68)$$

with

$$\kappa_1 = \frac{\mu B^2 \phi_0^2 (k_c^2 - r)}{(k_c^2 + \tilde{r})^2}, \quad (2.69)$$

$$\kappa_2 = -\frac{\mu B^2 \phi_0^2 (k_c^2 + r)}{(k_c^2 + \tilde{r})^2}. \quad (2.70)$$

We then perform a change of scale to fall back onto the canonical system found in [CM03; MC00]. Setting

$$T \rightarrow T/a_1; \quad (2.71)$$

$$X \rightarrow X\sqrt{a_2/a_1} \quad ; \quad Y \rightarrow Y\sqrt{a_2/a_1}; \quad (2.72)$$

$$P_1 \rightarrow P_1\sqrt{a_1/a_3} \quad ; \quad Q_1 \rightarrow Q_1\sqrt{a_1/a_3}; \quad (2.73)$$

$$R \rightarrow R a_1/a_5, \quad (2.74)$$

we define

$$g = \frac{a_4}{a_3} > 0, \quad (2.75)$$

$$b_1 = \frac{\mu}{a_2} > 0, \quad (2.76)$$

$$b_2 = \frac{(\kappa_1 + \kappa_2)a_5}{2a_2a_3} > 0, \quad (2.77)$$

$$b_3 = \frac{(\kappa_1 - \kappa_2)a_5}{2a_2a_3} < 0, \quad (2.78)$$

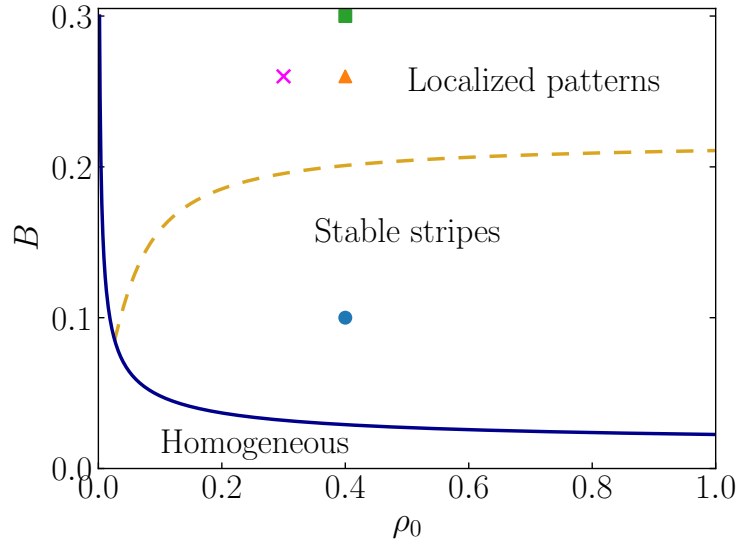


Figure 2.11 – Pattern phase diagram predicted from the weakly nonlinear analysis. Blue line: existence of critical frequency ω_c . Yellow dashed line: $g = 1$ is the stability boundary of roll with respect to squares when $\omega \lesssim \omega_c$. Blue bullet, orange triangle and green square correspond to different simulations performed with same density $\rho_0 = 0.4$ but different B and ω to keep $\omega = 0.9\omega_c$. Blue bullet: $B = 0.1$, we observe stripes in PDE solution and large clusters in Monte Carlo simulations. Orange triangle: $B = 0.26$, we observe pattern localization in PDE solution and small clusters in the simulation. Green square: $B = 0.3$, we observe square patterns in PDE solution and small clusters in the simulation. The blue bullet, the orange triangle and the green square correspond to the patterns shown in Figs. 2.12a, d and c, respectively. Magenta cross: $L_x = L_y = 175$ yields square patterns similar to Fig. 2.12c, whereas $L_x = L_y = 300$ yields localized stripes similar to Fig. 2.12d.

and we finally obtain

$$\begin{aligned} \partial_T P_1 = & P_1 + \partial_{XX} P_1 \\ & - |P_1|^2 P_1 - g|Q_1|^2 P_1 - R P_1 \end{aligned} \quad (2.79)$$

$$\begin{aligned} \partial_T Q_1 = & Q_1 + \partial_{YY} Q_1 \\ & - |Q_1|^2 Q_1 - g|P_1|^2 Q_1 - R Q_1 \end{aligned} \quad (2.80)$$

$$\begin{aligned} \partial_T R = & b_1 \tilde{\nabla}^2 R + b_2 \tilde{\nabla} (|P_1|^2 + |Q_1|^2) \\ & + b_3 (\partial_X^2 - \partial_Y^2) (|P_1|^2 - |Q_1|^2), \end{aligned} \quad (2.81)$$

with $\tilde{\nabla} \equiv \partial_X^2 + \partial_Y^2$.

2.5.3 Roll and square stability

As we now deal with amplitude equations (2.79), (2.80) and (2.81) in a canonical form, the results obtained by [CM03] are now directly transposable to our analysis. In particular, we can extract the stability boundaries of roll and square patterns, and predict modulational instabilities. The outcome of this analysis is that

- when $b_2 + b_3 > b_1$, rolls are unstable to one-dimensional disturbances (phase or amplitude modulation along the wave vector of patterns);

- if $b_2 - b_3 > b_1$ rolls undergo a two-dimensional instability, which is expressed through a transverse modulation of the rolls; see the dashed line in the phase diagram of Fig 2.11;
- if $g > 1$, squares are unstable to rolls. Squares also undergo a modulational instability when $b_2 > (1 + g)b_1/2$ (we do not observe such patterns in the PDE solution); it turns out that in our model the condition for rolls to be unstable to squares is the same as the two-dimensional instability for rolls, and is thus described by the same dashed line in Fig 2.11.

Since we have $b_3 < 0$, the condition $b_2 - b_3 > b_1$ preempts $b_2 + b_3 > b_1$; it is shown in [CM03] that the former then controls pattern formation. This explains why we observe the two-dimensional instability for rolls in Fig 2.12d. In our model, squares and transverse modulated rolls may exist separately at the same point of parameter space but they are ultimately selected by the geometry, the size, and the aspect ratio of the system (see magenta cross, Fig 2.11).

2.6 From equilibrium system to active system

So far, we have focused on the active system where spin flips are driven by a noise independent of temperature. Our analysis of the corresponding reaction-diffusion equations has shown the existence of a wealth of stationary patterns controlled by the values of the parameters of our model. These patterns simply do not exist in equilibrium when flips are controlled by temperature. To what extent does restoring a fraction of equilibrium spin flips within active flips suppresses the patterns we have obtained? Conversely, is adding a bit of activity over otherwise equilibrium flips sufficient to drive the system to a patterned stationary state? This section is about exploring the model system obtained by interpolating between fully active spin flips and equilibrium ones.

To implement both active and temperature controlled flips, the flipping rate $w(S_k, \phi)$ for spin S_k is now the sum of the active rate and the equilibrium rate which depends on the field value at the particle's location $\phi_k \equiv \phi(\mathbf{r}_k)$:

$$w(S_k, \phi) = \begin{cases} s\omega + \eta e^{B\phi_k\phi_0} \equiv w_k^- & \text{if } S_k = -1 \\ (1-s)\omega + \eta e^{-B\phi_k\phi_0} \equiv w_k^+ & \text{if } S_k = +1 \end{cases}, \quad (2.82)$$

and where η is the equilibrium flipping rate if spins did not interact with the Gaussian field.

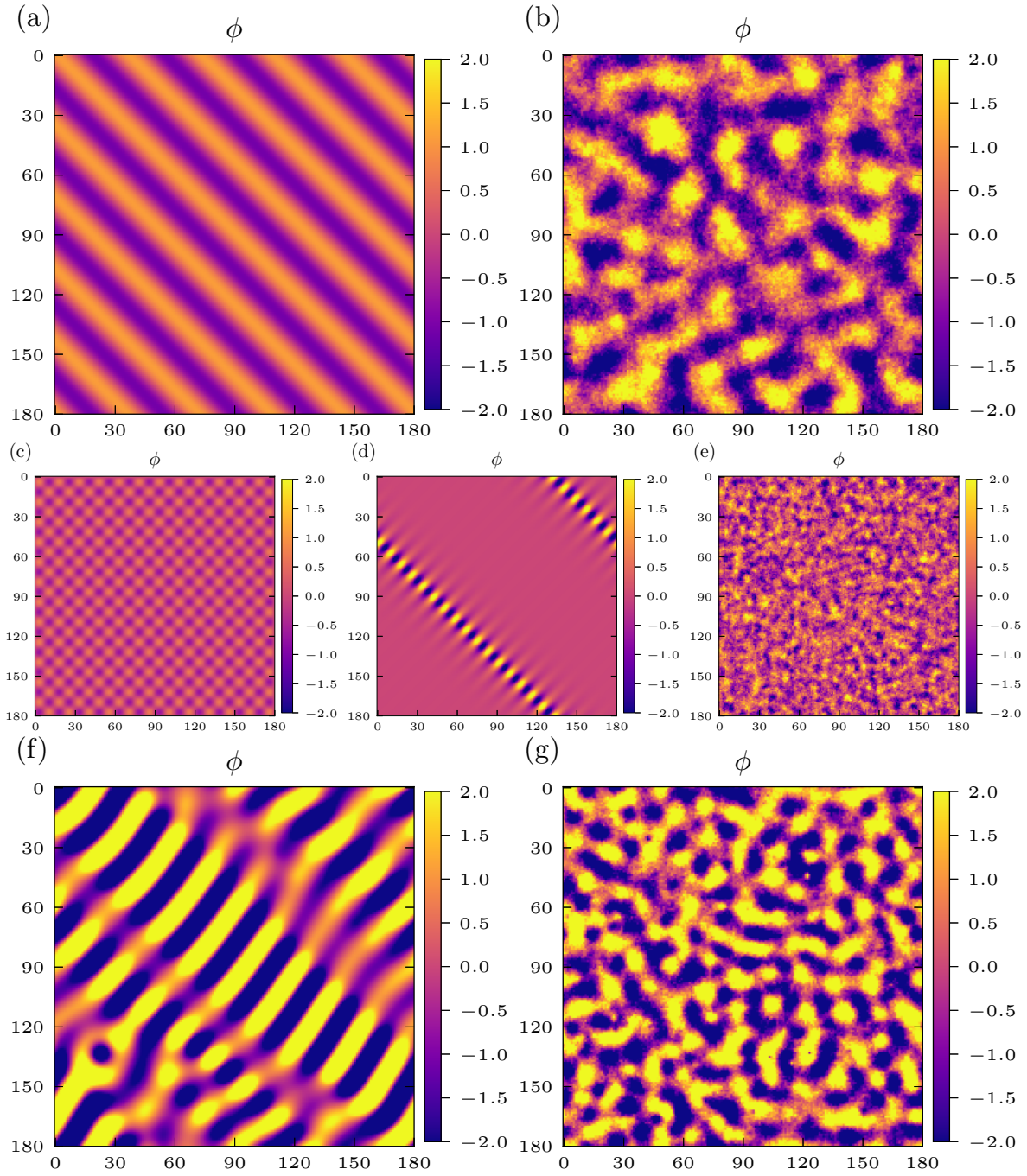


Figure 2.12 – Simulation and solution of the PDEs close to pattern apparition threshold (a,b,c,d,e), and for ω far below ω_c (f,g). Shared parameters: $r = 0.01$, $\rho_0 = 0.4$, $\phi_0 = 8$, $\mu = 5$. For (a), (b), (c), (d) and (e) we have $\omega = 0.9\omega_c$. For (f) and (g) we have $\omega = 0.2\omega_c$. (a) $B = 0.1$, PDEs solution shows stripes in agreement with Fig. 2.11. (b) $B = 0.1$, Monte Carlo (MC) simulation shows structures of same size. (c) $B = 0.3$, square pattern (PDE). (d) $B = 0.26$, pattern localization (PDE). (e) $B = 0.26$, micro clusters (MC). (f) $B = 0.22$, stripes and localized clusters (PDE). (g) $B = 0.22$, stripes, clusters and lumps (MC).

2.6.1 Mean-field analysis

The mean-field equations are the same as Eq. (2.16) – (2.18) with α (resp. γ) changed into w^- (resp. w^+):

$$\partial_t \rho^+ = \mu \nabla \cdot [\rho^+ \nabla \frac{\partial f_{\text{MF}}}{\partial \rho^+}] + w^- \rho^- - w^+ \rho^+, \quad (2.83)$$

$$\partial_t \rho^- = \mu \nabla \cdot [\rho^- \nabla \frac{\partial f_{\text{MF}}}{\partial \rho^-}] - w^- \rho^- + w^+ \rho^+, \quad (2.84)$$

$$\partial_t \phi = \nabla^2 \phi - r \phi - B \rho^+ (\phi - \phi_0) - B \rho^- (\phi + \phi_0). \quad (2.85)$$

First, we search for a homogeneous stationary solution of this system. The self-consistent equation now verified by ϕ_h is more involved. We find that a homogeneous solution has

$$\rho_h = \rho_0, \quad (2.86)$$

$$\phi_h = G(\phi_h) \quad (2.87)$$

$$\psi_h = \frac{\tilde{r}}{B \phi_0} \phi_h, \quad (2.88)$$

where the function $G(\phi_h)$ is given by

$$G(\phi_h) = \frac{B \rho_0}{\tilde{r}} \frac{(2s - 1)\omega + 2\eta \sinh(B \phi_h \phi_0)}{\omega + 2\eta \cosh(B \phi_h \phi_0)} \phi_0. \quad (2.89)$$

We show a graphical solution of $G(\phi_h) = \phi_h$ in Fig. 2.13. We remark on Fig. 2.13(a) that the active fraction s does not play a significant role when equilibrium flips are of the same order of magnitude as the active flip ω . By contrast, when equilibrium flips are negligible, the homogeneous state is completely controlled by the fraction s (see Fig. 2.13b). The most interesting regime is for $2\eta/\omega \sim 10^{-1}$ where the self-consistent equation has up to five solutions for some parameters (see Fig. 2.13c), unlike what we can observe in equilibrium (one or three solutions) or for the full active regime (one solution only). Finding out about the relative stability of these solutions comes first. This is the purpose of the following subsection.

2.6.2 Linear stability analysis

We now perform a linear stability analysis of equations (2.83), (2.84) and (2.85), and study the stability for the different solutions of the self-consistent equation $\phi_h = G(\phi_h)$. We restrict ourselves to the case $s = 1/2$ which contains already rich physics. With this choice of s , we still have an up down symmetry for the spins, thus $\phi_h = 0$ is always a homogeneous and stationary solution. We perform LSA around this solution and the results are shown on Fig. 2.14(a). The results are interesting when compared to the existence of other solutions of the self-consistent equations (see Fig. 2.14(b)). In particular, the homogeneous state develops patterns before other solutions for ϕ_h appear (case $\omega = 0.45$ for instance). In addition, we observe in the explicit PDEs' solutions that the final state of the system depends on initial conditions: even if the homogeneous state $\phi_h = 0$ is not

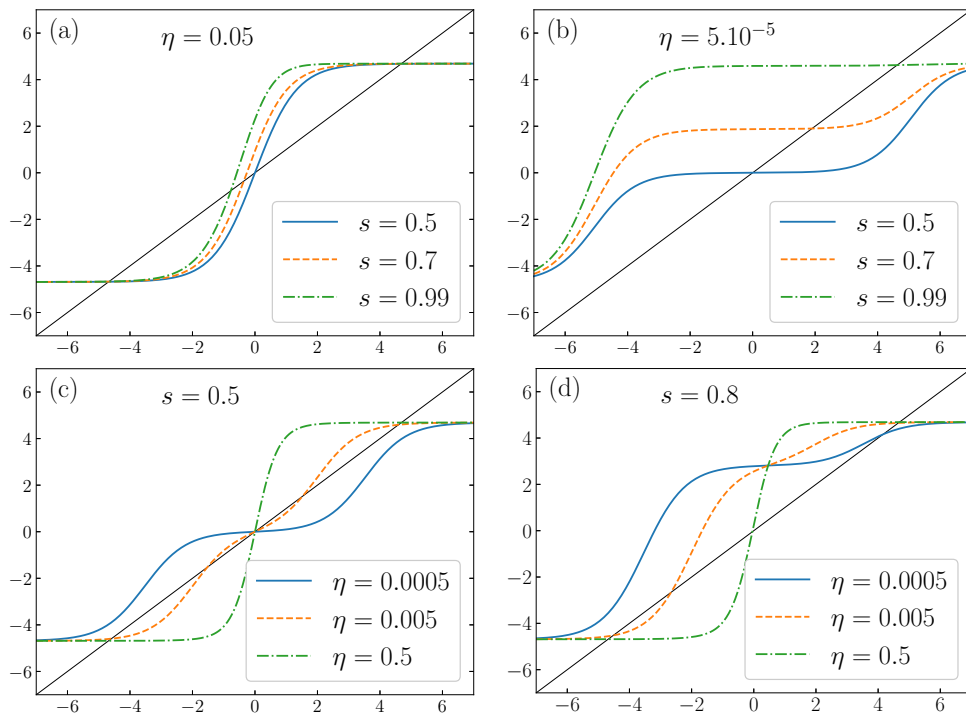


Figure 2.13 – Graphic solution of equation $G(\phi_h) = \phi_h$. Parameters: $r = 0.01$, $B = 0.3$, $\rho_0 = 0.5$, $\phi_0 = 5$, $\mu = 1$ and $\omega = 0.1$. When $\eta \sim \omega$ the solution is close to the equilibrium one and s does not play important role.

stable, the system may prefer creating patterns instead of having a full ferromagnetic order, which is also stable. To predict, at low cost, as a way of rationalizing our results, the final state of the system in this bi-stability regime, we can exhibit a mean field “free energy” F whose minima are the possible homogeneous solutions for ϕ (F is not a free energy since we are far from equilibrium). For a homogeneous density ρ_0 , the evolution equation of the homogeneous field ϕ simply becomes

$$\partial_t \phi = -\frac{\partial F}{\partial \phi}, \quad (2.90)$$

with $F(\phi) = (r + B\rho_0)\phi^2/2 - \rho_0 \ln(\omega + 2\eta \cosh(B\phi_0\phi))$ an even function of ϕ displayed on Fig. 2.14(c) for different values of ω . The global minimum of the function F corresponds indeed to the final state of the magnetization, namely $\langle \phi \rangle = 0$ or $\langle \phi \rangle > 0$, as observed in the PDE solution (see Fig. 2.15).

To sum up this section, we have seen that introducing a small amount of equilibrium in the dynamics of particle flip does not destroy the patterns. Furthermore, depending on its initial state, the system is now able to display either patterns, or ferromagnetic order, in striking contrast with a full active or equilibrium case where only one option is accessible. We now turn to the analysis of energy dissipation in the active system, and more precisely, we address the question of origin and of the location of entropy production.

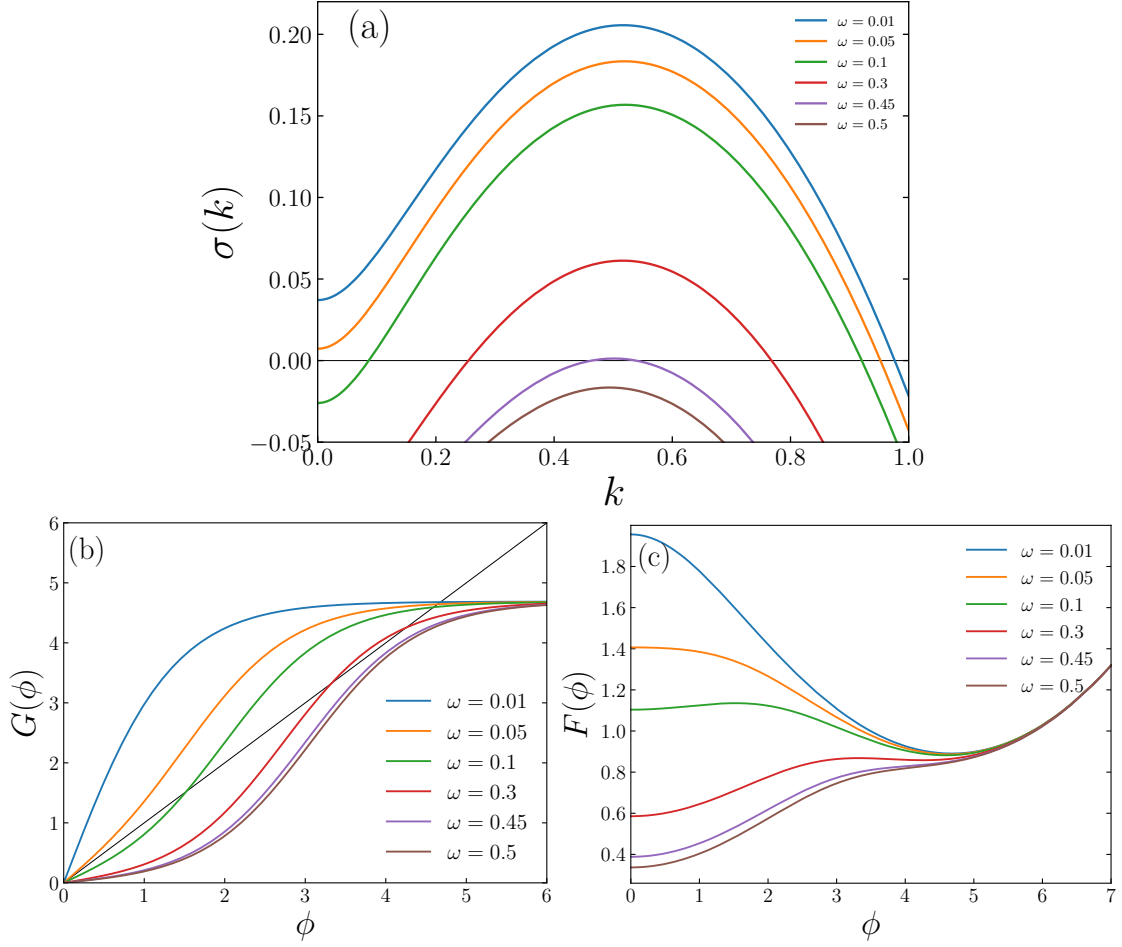


Figure 2.14 – For different values of ω : (a) Most unstable eigenvalues from linear instability analysis around $\phi_h = 0$. (b) Graphical solving of the self-consistent equation for the 'magnetization' field ϕ . (c) Mean field free energy $F(\phi)$. Starting from the value $\omega = 0.5$ and decreasing ω yields different regimes. We observe successively a homogeneous state with zero magnetization, a patterned phase, and then a homogeneous ferromagnetic phase when such a state has the minimum energy. Other parameters: $r = 0.01$, $B = 0.3$, $\rho_0 = 0.5$, $\phi_0 = 5$, $\mu = 1$, $\eta = 0.005$ and $s = 0.5$.

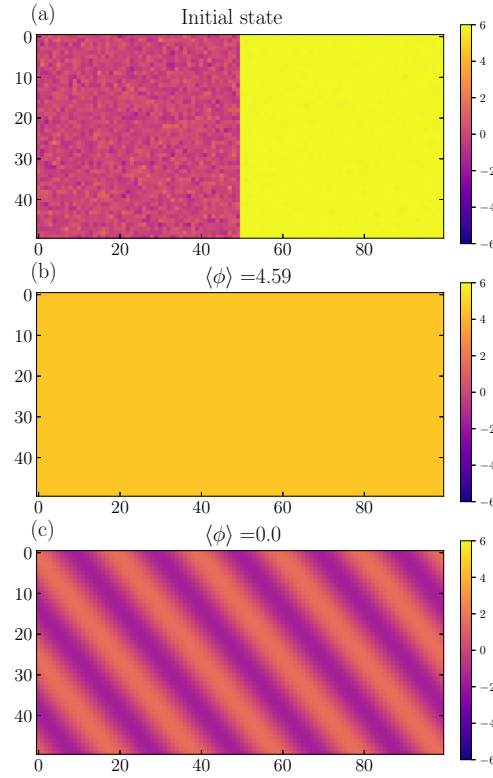


Figure 2.15 – Stationary state for the field ϕ as given by the PDE evolution Eqs. (2.83), (2.84), (2.85) from a non-homogeneous initial state. (a) Initial conditions for the field ϕ with $\langle\phi\rangle = 0$ in the left part of the box and $\langle\phi\rangle = 6$ in the right part of the box, and $\rho = 0.5 + (\text{noise})$ everywhere. (b) Steady state for ϕ when $\omega = 0.1$. (c) Steady state for ϕ when $\omega = 0.3$. Other parameters: $r = 0.01$, $B = 0.3$, $\rho_0 = 0.5$, $\phi_0 = 5$, $\mu = 1$, $\eta = 0.005$ and $s = 0.5$.

2.7 Entropy production

Entropy production is a quantity that provides a measure of the degree of irreversibility of the dynamics of the system. In some cases it can simply be connected to the rate of energy dissipated by the system into the environment. We view entropy production as an elegant way to pinpoint the physical ingredients that are responsible for driving the system out of equilibrium. When spatially resolved, in the spirit of [Nar+17], entropy production may be used to connect the emerging structures, at a local level, with dissipation. While the nonequilibrium drive has been identified as the key ingredient for the generation of patterns, whether the genuinely nonequilibrium processes operate at the pattern boundaries, or within the bulk of the system, is a question of interest to us.

To estimate the total entropy production along a trajectory (in the whole phase space), we have to evaluate the probability of a trajectory relative to the probability of the time reversed trajectory [LS99]. This question can be asked for various collections of degrees of freedom; we choose to focus on a single particle of position $X(t) \equiv X_t$ interacting with the Gaussian field $\phi(x, t) \equiv \phi_t(x)$. We restrict our derivation to a one dimensional system to keep the notation simple. The system evolves according to Eqs. (2.3) and (2.5) with $T = \Gamma = 1$, and the spin flips from $+1$ to -1 (resp. from -1 to $+1$) with finite rate γ (resp. α). The spin S_t jumps a finite number of times over an interval $[0, t_F]$, and S_t is right continuous. The Hamiltonian H will also be right continuous as a function of time. On an interval $[0, t_F]$ we define $t_j = jt_F/N$ and $t_{j+1} - t_j = t_F/N = \Delta t$. The probability of a noise history for the particle is given by

$$P[\xi|\xi_I] = \exp\left(-\frac{1}{2} \sum_{j=0}^{N-1} \Delta \xi_j^2\right). \quad (2.91)$$

Using the Itô convention, the probability of a trajectory $\{X(t)\}_{0 \leq t \leq t_F}$ is equal to the probability of observing the corresponding noise history. We thus have

$$P[X|X_I] = P[\xi|\xi_I] \quad (2.92)$$

$$= \exp \frac{-1}{4\mu} \sum_{j=0}^{N-1} \Delta t \left[\dot{X}_{t_j} + \mu \frac{\partial H}{\partial X_{t_j}}[X_{t_j}, \phi_{t_j}(X_{t_j})] \right]^2 \quad (2.93)$$

$$\simeq \exp \frac{-1}{4\mu} \int_0^{t_F} d\tau \left[\dot{X}_\tau + \mu \frac{\partial H}{\partial X_\tau}[X_\tau, \phi_\tau(X_\tau)] \right]^2, \quad (2.94)$$

where the set of points at which H is discontinuous is of measure zero. At initial time $t_I = 0$, we start with $X(0) = X_I$, $\phi(x, 0) = \phi_I(x)$ and $S(0) = S_I$ and the system evolves to a final time t_F . We can define the time reversed noise history through $\tilde{\xi}(\tau) = \xi(t_F - \tau)$ and the reversed trajectory is then $\tilde{X}(\tau) = X(t_F - \tau)$ such that $\tilde{X}(0) = X(t_F) \equiv \tilde{X}_I$.

Entropy creation along a path is given by

$$\begin{aligned} & \ln \frac{P[X(\tau)|X_I]}{P[\tilde{X}(\tau)|\tilde{X}_I]} \\ &= -\frac{1}{4\mu} \int_0^{t_F} (\dot{X}_\tau + \mu \frac{\partial H}{\partial X_\tau})^2 - (\dot{X}_\tau - \mu \frac{\partial H}{\partial X_\tau})^2 d\tau \end{aligned} \quad (2.95)$$

$$= -\int_0^{t_F} \dot{X}_\tau \frac{\partial H}{\partial X_\tau} d\tau. \quad (2.96)$$

Similarly, since we have a Langevin equation for the field ϕ , entropy creation of a field trajectory reads

$$\ln \frac{P[\phi(x, \tau)|\phi_I(x)]}{P[\tilde{\phi}(x, \tau)|\tilde{\phi}_I(x)]} = -\int_0^{t_F} d\tau \int_x \partial_\tau \phi(x, \tau) \frac{\delta H}{\delta \phi(x, \tau)}. \quad (2.97)$$

We also have entropy creation related to the realization of the sequence of flips. If we start from a down configuration and if we slice time into intervals of duration Δt then entropy creation for a flip history writes

$$\ln \frac{P[S(\tau)|S_I]}{P[\tilde{S}(\tau)|\tilde{S}_I]} = \delta_{t_F} \ln \frac{\alpha}{\gamma}, \quad (2.98)$$

where $\delta_{t_F} = -1, 0$ or 1 , depending on the initial and final values of the spin. We want to relate these previous results to the energy difference between the final time and the initial time. Let us start from the energy difference to see what terms appear in the calculation. We have

$$H(t_F) - H(0) = \sum_{j=0}^{N-1} H[X_{t_{j+1}}, \phi_{t_{j+1}}, S_{t_{j+1}}] \quad (2.99)$$

$$\begin{aligned} & - H[X_{t_j}, \phi_{t_j}, S_{t_j}] \\ &= \sum_{j=0}^{N-1} \Delta t \dot{X}_{t_j} \frac{\partial H}{\partial X} [X_{t_j}, \phi_{t_j}, S_{t_{j+1}}] \\ & \quad + \Delta t \int_x \dot{\phi}_{t_j} \frac{\delta H}{\delta \phi(x)} [X_{t_j}, \phi_{t_j}, S_{t_{j+1}}] \\ & \quad + H[X_{t_j}, \phi_{t_j}, S_{t_{j+1}}] - H[X_{t_j}, \phi_{t_j}, S_{t_j}] \\ & \quad + o(\Delta t) \end{aligned} \quad (2.100)$$

$$\begin{aligned} & \simeq \int_0^{t_F} d\tau \left[\dot{X}_\tau \frac{\partial H}{\partial X_\tau} [X_\tau, \phi_\tau, S_\tau] \right. \\ & \quad \left. + \int_x \dot{\phi}_\tau \frac{\delta H}{\delta \phi(x)} [X_\tau, \phi_\tau, S_\tau] \right] \\ & \quad + \sum_{t_\alpha} \left[H[X_{t_\alpha^+}, \phi_{t_\alpha^+}, S_{t_\alpha^+}] \right. \\ & \quad \left. - H[X_{t_\alpha^-}, \phi_{t_\alpha^-}, S_{t_\alpha^-}] \right], \end{aligned} \quad (2.101)$$

and where the spin flips at time t_α , with t_α^+ and t_α^- denoting the times right after and right before the flip, respectively. We can now compute the entropy produced along any path:

$$\ln \frac{P[X_\tau, \phi_\tau(x), S_\tau | X_I, \phi_I(x), S_I]}{P[\tilde{X}_\tau, \tilde{\phi}_\tau(x), \tilde{S}_\tau | \tilde{X}_I, \tilde{\phi}_I(x), \tilde{S}_I]} = - \int_0^t d\tau \left(\dot{X}_\tau \frac{\partial H}{\partial X} + \int_x \partial_\tau \phi(x, \tau) \frac{\delta H}{\delta \phi(x, \tau)} \right) + \delta_{t_F} \ln \frac{\alpha}{\gamma} \quad (2.102)$$

$$= - [H(t_F) - H(0)] + \delta_{t_F} \ln \frac{\alpha}{\gamma} + \sum_{t_\alpha} \left[H[X_{t_\alpha^+}, \phi_{t_\alpha^+}, S_{t_\alpha^+}] - H[X_{t_\alpha^-}, \phi_{t_\alpha^-}, S_{t_\alpha^-}] \right] \quad (2.103)$$

$$= - [H(t_F) - H(0)] + \delta_{t_F} \ln \frac{\alpha}{\gamma} + \sum_{t_\alpha} 2B\phi_0 S_{t_\alpha^-} \phi_{t_\alpha}(X_{t_\alpha}). \quad (2.104)$$

Dividing this result by t_F and taking the limit $t_F \rightarrow \infty$ yields the entropy production rate σ . We immediately see that the first two terms in Eq. (2.104) vanish when divided by the total duration t_F as t_F is taken asymptotically large, since they are bounded. In the stationary state, the entropy production thus simplifies into

$$\sigma = \lim_{t_F \rightarrow \infty} \frac{2B\phi_0}{t_F} \sum_{0 < t_\alpha < t_F} S_{t_\alpha^-} \phi_{t_\alpha}(X_{t_\alpha}) \quad (2.105)$$

$$= \lim_{t_F \rightarrow \infty} \frac{2B\phi_0}{t_F} N_{t_F} \langle S_{t_\alpha^-} \phi_{t_\alpha}(X_{t_\alpha}) \rangle, \quad (2.106)$$

with N_{t_F} the number of flips in $[0, t_F]$. For a variable that flips between two states at fixed rates α and γ , this number is given by

$$N_{t_F} = 2 \frac{\alpha\gamma}{\alpha + \gamma} t_F, \quad (2.107)$$

when $t_F \rightarrow \infty$, and thus scales like $O(t_F)$. We can further simplify the expression of entropy production:

$$\sigma = 4B\phi_0 \frac{\alpha\gamma}{\alpha + \gamma} \langle S_{t_\alpha^-} \phi_{t_\alpha}(X_{t_\alpha}) \rangle \quad (2.108)$$

$$= 4B\phi_0 \omega s(1-s) \langle S_{t_\alpha^-} \phi_{t_\alpha}(X_{t_\alpha}) \rangle. \quad (2.109)$$

The average $\langle S_{t_\alpha^-} \phi_{t_\alpha}(X_{t_\alpha}) \rangle$ is however more complicated to compute because it depends on the whole dynamics. We are now considering two important limiting cases: (i) the time between two flips is large with respect to the particle-field dynamics, (ii) the time between two flips is small in that respect. In (i), we typically witness pattern formation. In this situation, the field at the particle's location has the same sign as the spin before the flip, and thus scales like $O(\phi_0 S_{t-})$. We can further say that the field can equilibrate between flips, thus the field ϕ is equal to $\phi_{s.c.}$ which satisfies the self-consistent equation

$\phi_{\text{s.c.}} = B\phi_0\rho_0 \tanh(B\phi_0\phi_{\text{s.c.}})/(r + B\rho_0)$ (see Section 2.4.1) in the bulk of each microphase. In this case the entropy production rate reads:

$$\sigma_{\omega \ll \omega_c}^{\max} = 4B\phi_0\phi_{\text{s.c.}}\omega s(1-s). \quad (2.110)$$

In regime (ii) of fast flipping, patterns disappear, and $S(t)$ and $\phi_t(X_t)$ are almost uncorrelated. We can actually predict that the entropy production rate saturates when $\omega \rightarrow \infty$. We notice that for N particles we have, by definition, $\psi(x, t) = \sum_{k=1}^N S_k(t)\delta(x - X_k(t))$ and thus for one particle $\psi(x, t) \sim S_t$. We thus approximate $\langle S_{t_\alpha}^- \phi_{t_\alpha}(X_{t_\alpha}) \rangle$ with its continuum description, namely $\langle \psi_t \phi_t(X_t) \rangle$. From the evolution equations of the fields, we compute $\phi \times \partial_t \psi + \psi \times \partial_t \phi$ (where $\partial_t \psi$ is given in Eq. (2.20) and $\partial_t \phi$ is given in Eq. (2.21)) to reconstruct a time derivative of a correlation, which is 0 in steady state. In the particular case of symmetric flips $s = 1/2$, we have:

$$\begin{aligned} 0 &= \partial_t \langle \psi \phi \rangle \\ &= \left\langle \phi \left(\mu \nabla^2 \psi + \mu B \nabla \cdot [(\psi \phi - \rho \phi_0) \nabla \phi] - \omega \psi \right) \right. \\ &\quad \left. + \psi \left(\nabla^2 \phi - r \phi - B \rho \phi + B \phi_0 \psi \right) \right\rangle \end{aligned} \quad (2.111)$$

$$\stackrel{\omega \rightarrow \infty}{=} -\omega \langle \psi \phi \rangle + B \phi_0 \langle \psi^2 \rangle, \quad (2.112)$$

which yields $\langle \psi \phi \rangle \xrightarrow{\omega \rightarrow \infty} B \phi_0 \langle \psi^2 \rangle / \omega$, from which we infer the produced entropy for $s = 1/2$:

$$\sigma_{\omega \rightarrow \infty} \propto B^2 \phi_0^2. \quad (2.113)$$

In our numerical experiments, we start to measure entropy production at time 0 and we define the entropy production rate for a particle k at time t as

$$\sigma_k(t) = \frac{2B\phi_0}{t} \sum_{0 < t_{\alpha k} < t} S_{t_{\alpha k}}^k \phi_{t_{\alpha k}}(X_{t_{\alpha k}}^k), \quad (2.114)$$

where the $t_{\alpha k}$ are the time of flips of particle k . In Fig. 2.16 (left), we display the convergence of the entropy production rate towards its stationary state value for 100 particles (out of $N = 6479$ in the simulation), starting from a homogeneous state $\langle \phi \rangle = 0$ and all particles spin up. Measuring entropy production for different values of ω , we recover that entropy production rate saturates when $\omega \rightarrow \infty$, and we find the value we predicted in Eq. (2.110) for $\omega \rightarrow 0$. These results are displayed in Fig. 2.16 (right), where the graph also shows that the critical flipping rate predicted by the LSA matches the transition observed in entropy production.

Finally, another way to extract interesting information from our calculation for entropy production is to define a local entropy production rate or density of entropy production such that $\sigma = \int d^2r \sigma(\mathbf{r})$. Returning to a two-dimensional system, from Eq. (2.105),

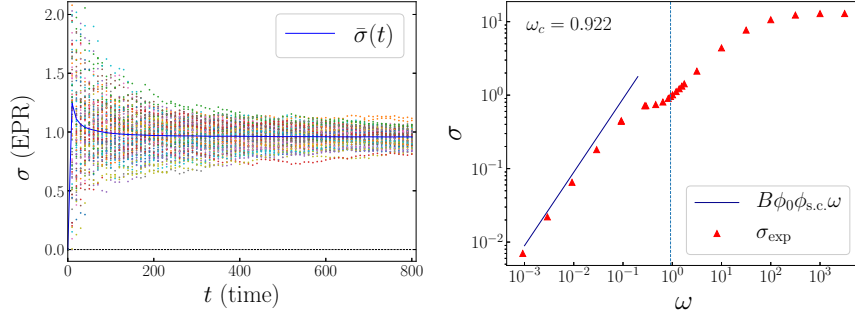


Figure 2.16 – Left: Entropy Production Rate of 100 particles out of $N = 6479$ particles in the simulation. Each dot represents the entropy production rate $\sigma_k(t)$ of a particle k at time t . Blue line: average entropy production rate $\bar{\sigma}(t) = \frac{1}{N} \sum_{k=1}^N \sigma_k(t)$. Parameters: $r = 0.01$, $B = 0.18$, $\rho_0 = 0.2$, $\phi_0 = 8$, $\mu = 5$, $s = 0.5$, $\omega = 0.922$. **Right:** Entropy production rate as a function of the flipping parameter ω . The dashed blue vertical line indicates the pattern apparition threshold ω_c predicted by mean field analysis. Parameters: $r = 0.01$, $B = 0.18$, $\rho_0 = 0.2$, $\phi_0 = 8$, $\mu = 5$ and $s = 0.5$.

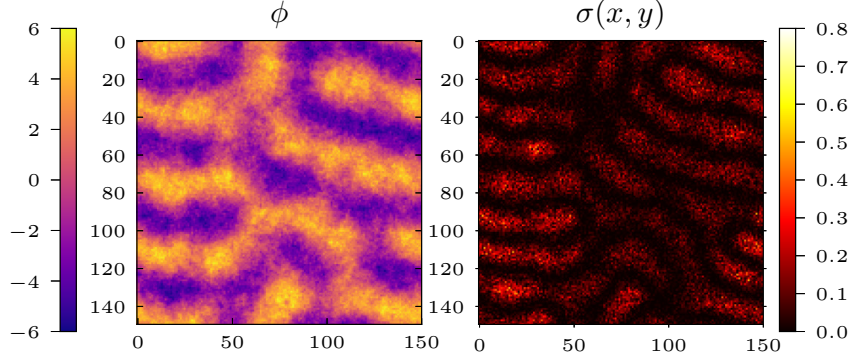


Figure 2.17 – Snapshot of the system. Left: field ϕ . Right: entropy production density. Parameters: $r = 0.01$, $B = 0.106$, $\rho_0 = 0.3$, $\phi_0 = 8$, $\mu = 5$.

we can identify such an entropy production density for a system with N particles:

$$\sigma(\mathbf{r}) = \lim_{t \rightarrow \infty} \frac{1}{t} \sum_{k=1}^N 2B\phi_0 \sum_{t_{\alpha k} < t} S_{t_{\alpha k}}^k \phi_{t_{\alpha k}}(\mathbf{r}) \delta(\mathbf{r} - \mathbf{X}_{t_{\alpha k}}^k), \quad (2.115)$$

where the $(t_{\alpha k})_{\alpha \in \mathbb{N}}$ are the instants of flip of particle k , and where \mathbf{X}_t^k is the position of particle k at time t . We are now able to establish a map of the entropy production rate within the stationary state. In our simulations, though we observe diffusion of the whole pattern, the entropy production rate converges over a much smaller time scale, and we thus reach a “stationary state” before pattern blurring. In Fig. 2.17, we see that entropy production is localized within the bulk of the stripes. In other words, dissipation occurs in the bulk and not specifically at the boundaries of patterns. While the existence of patterns is a genuine nonequilibrium effect, one cannot interpret the role of the nonequilibrium drive in terms of a stabilizing effective surface tension at the boundaries of the ordered domains.

2.8 Conclusion

Our goal was to explore and predict the emergence of collective phenomena in assemblies of active particles whose interactions are mediated by a fluctuating medium. We have done so on the basis of a minimal model in which particles diffuse while locally constraining the medium deformation. Activity is introduced by means of an internal degree of freedom that controls the interaction with the background field. This internal degree of freedom fluctuates independently of the bath temperature, and thus breaks the equilibrium nature of the dynamics of the whole system.

By means of Monte Carlo simulations and of a mean-field analysis of the dynamical equations, we have shown that this system displays a wealth of pattern formation regimes. When patterns appear, their wavelength is given by the geometric mean of the characteristic correlation length of the underlying elastic field and of the diffusion length of particles between two active flips. This geometric mean property is reminiscent of the typical wavelength emerging in crystal growth and in the Mullins-Sekerka instability [LM77]. This coincidence might *a posteriori* be perceived as little surprising since we have at stake, in both systems, interactions favoring phase separation (a surface tension ingredient) competing with a diffusive process. In addition, as the number of particles is conserved in the system, patterns can be localized on a small fraction of the system size [MC00; CM03]. Recent theoretical work also suggests that pattern analysis in systems with a conserved quantity can be carried out far from pattern apparition threshold [HF18]. Applying such analysis to our system would certainly enrich our conclusions. We have also examined how to interpolate between equilibrium dynamics and active dynamics for the flips since we reasonably expect that the flips might also feature temperature induced fluctuations. This interpolation has shown that the patterns could survive a moderate amount of equilibrium. Finally, we addressed the question of energy dissipation and entropy production in the active system. We have seen that entropy production vanishes for low flipping rates, as expected, and that it saturates for large flipping rates. We have also seen that entropy is produced within the bulk of the patterns, as opposed to other active systems where it is localized at the phase boundaries [Nar+17].

We are now at a stage where our model should be made more realistic. This may be achieved in a variety of directions. The Hamiltonian for the field can be adapted to specific systems we want to describe. Typically, we could use a Helfrich Hamiltonian to work on biological membranes. The field dynamics may also be changed. If the field now stands for a molecular density, we expect it to evolve according to a conserved dynamics (Cahn-Hilliard, Allen-Cahn). To focus on active proteins in the biological membrane, we also believe that hydrodynamic effects should be taken into account. This would certainly imply dealing with non-local equations, with the drag in a two-dimensional liquid layer (the lipid leaflet), and with the three-dimensional bulk liquid, which drives the system to another level of complexity, along with a (probably) richer behavior.

Chapter 3

Colloidal particles in lamellar phases

In this chapter, we build an equilibrium model that accounts for experimental results obtained for colloidal particles embedded in a lamellar phase. Our approach takes into account the finite size of the colloids, the discrete nature of the layers, and includes the Casimir-like effect of fluctuations. We will focus on two possible interactions between the colloids and the lamellae: either i) colloids are strongly adherent to the adjacent membranes, or ii) the colloids and lamellae undergo excluded-volume interactions only. In a second part, we present the results of Monte Carlo simulations based on the two-body effective interaction derived for two colloids. Both models i) and ii) predict finite-size aggregates. Model i) agrees semi-quantitatively, without any adjustable parameters, with the experimental data measured on silica nanospheres inserted within lyotropic lamellar phases. The results of this chapter have been published in [\[Zak+19\]](#).

3.1 Introduction

Assembling nanoparticles into structured macroscopic materials is one of the Holy Grail of material science (see Chapter 1). One of the aims of such realizations is to create versatile materials that present both electronic, optic or magnetic properties of some inorganic materials, and the mechanical properties (elasticity, viscosity) of organic materials. In addition, endowing these materials with bio-compatibility opens the route for many medical applications such as accurate imaging, tumor tracking, or drug delivery [\[Guo+10\]](#). Materials designed from lyotropic liquid crystals seem particularly promising.

Before focusing on the specific system we consider in this chapter, let us recall the definitions of the two main classes of liquid crystals. We usually distinguish between thermotropic and lyotropic liquid crystals. Thermotropic liquid crystals are made of one compound, and the temperature is their only control parameter. At low temperature, they may display both positional order and orientational order. In latter case, the liquid-crystal phase is referred to as smectic or discotic. At higher temperature, positional order is destroyed and orientational order may still exist: this is the nematic phase. For even higher temperatures, order is destroyed and we recover an isotropic liquid.

Lyotropic liquid crystals are quite different in their composition. They are obtained by the dissolution of one or several compounds into a solvent (often water). These compounds can self-assemble in such entities as micelles or bilayers. The structure of the phase depends on two control parameters which are the temperature and the concentration of the solute.

Both categories of liquid crystals are used to design hybrid materials with original properties. In 1970, Brochard and de Gennes suggested that including magnetic particles into nematic liquid crystals would strongly enhance the magnetic response of the material [BG70]. Experimental realizations followed for magnetic inclusions in lyotropic phases [LM79]. Practically, thermotropic liquid crystals are intensively used in the display technologies. They also offer a good medium to achieve a bottom-up self-assembly of nano-particles [Pra+09; LYS14; Woj+09; Cou+12; Lew+13]. Lyotropic liquid crystals, however, may appear as better candidates to achieve self-assembly of particles at nanoscale and microscale. There are several reasons. First, their elastic moduli are lower than those of thermotropics, so that the induced interactions between particles can be weaker (comparable to $k_B T$). Second, their physical properties (spacing, flexibility, electrical charge, etc.) are easily tuned via the composition [Liu+10; Ven+11]. Third, they are intrinsically heterogeneous (alternating layers of amphiphilic molecules and water), and thus offer the possibility of hosting, in the bulk phase, particles with different chemical affinities [WER99; Fir+01]. Hence, they can be used as a host phase for the particles, or even used as physical templates for nano-particle synthesis [Sur+05].

We draw our attention to the lyotropic lamellar phases. Here, our objective is to build a generic model from which we can analytically extract the effective interactions between the particles embedded into the lamellar phases. We call effective interactions, the attractive or repulsive interactions between the particles, mediated by the lamellar phase. With the effective interactions, it will be possible to predict the particles' phase behavior (size and formation of particle aggregates, stability of the phases).

This chapter will be structured as follows. In Section 3.2, we define the model for the lamellar phase only (without the particles). We use a discrete Gaussian model to describe each lamella individually, a common approach for lyotropic lamellar phases [Hol91; LSB95; Saf94]. What is new, however, is our way to implement the coupling between the colloidal particles and the lamellae. In Section 3.3, we consider two specific limit cases. We will first treat the case of colloids that are strongly adherent to their adjacent lamellae. Then, we will focus on colloids that display excluded-volume interactions only. In both cases the couplings to the lamellae are nonlinear, which implies that the effective interactions possess both an elastic component (coming from the elasticity of the medium), and a Casimir-like component (coming from the thermal fluctuations of our constrained lamellar phase). Our approach takes these two components into account. Finally, in Section 3.4, we will relate our results to real experiments. We will recall the different orders of magnitude for the physical parameters at stake. By means of Monte Carlo simulations we will be able to discriminate between our different models when we compare the *in silico* structure factor to the experimental one. I have mostly contributed to Sections 3.2 and 3.3. In Section 3.5, we present the results of our collaboration with Doru Constantin and Paolo Galatola. The different contribution are the following: Doru

Constantin directed the experiments and extracted the structure factor in experimental systems, and Paolo Galatola implemented the Monte Carlo simulations. This work was accomplished under the supervision of Jean-Baptiste Fournier.

3.2 Lamellar phase model

Lamellar phases are stacks of membranes in an aqueous environment. Membranes interact through different mechanisms: attractive Van der Waals forces, repulsive hydration forces at very short separations, screened electrostatic forces, and the so-called Helfrich long-range repulsion arising from the loss of entropy associated with the confinement of the transverse membrane fluctuations [Hel78]. The latter may dominate for membranes with weak bending rigidities, i.e., typically for surfactant systems [RS88]. There may also be attractive fluctuation-induced interactions originating from counterion correlations [Jho+10].

Lipids form lamellar phases of bilayer membranes where the layer spacing d is usually comparable to the membrane thickness δ , i.e., a few nm. Conversely, surfactant systems can form lamellar phases with $d \gg \delta$, and even unbound lamellar phases. An exact theoretical modelization of the elasticity of lamellar phases, taking into account all the different interactions, is very difficult to achieve. We therefore limit ourselves to the discrete Gaussian elastic theory of lamellar phase [Hol91; LSB95; Saf94], as described below.

3.2.1 Definition

We consider a lamellar phase consisting of N parallel membranes of thickness δ (see Fig. 3.1). We assume that in the homogeneous, equilibrium state, the thickness of the water layers between the membranes is w and the repeat distance is d , with

$$d = w + \delta. \quad (3.1)$$

In a Cartesian reference frame $(\mathbf{r}, z) \equiv (x, y, z)$, we parametrize the shape of the n -th membrane by the height function $z_n(\mathbf{r}) = nd + h_n(\mathbf{r})$, which represents its elevation above the plane $z = 0$. In addition to the bending energy of each membrane [Hel73], the elastic energy \mathcal{H} , or Hamiltonian, includes the most general interaction that is quadratic in the h_n 's, couples only adjacent membranes, and complies with global translational invariance. Note that the effects induced by the membrane tension become relevant at the micrometer scale, far beyond the typical size of the embedded particles, their interaction range and the size of the lamellar structure. The tension is then neglected in the Hamiltonian, which thus reads [Hol91; LSB95; Saf94]:

$$\mathcal{H} = \sum_{n=0}^{N-1} \int d^2r \left[\frac{\kappa}{2} (\nabla^2 h_n)^2 + \frac{B}{2} (h_{n+1} - h_n)^2 \right]. \quad (3.2)$$

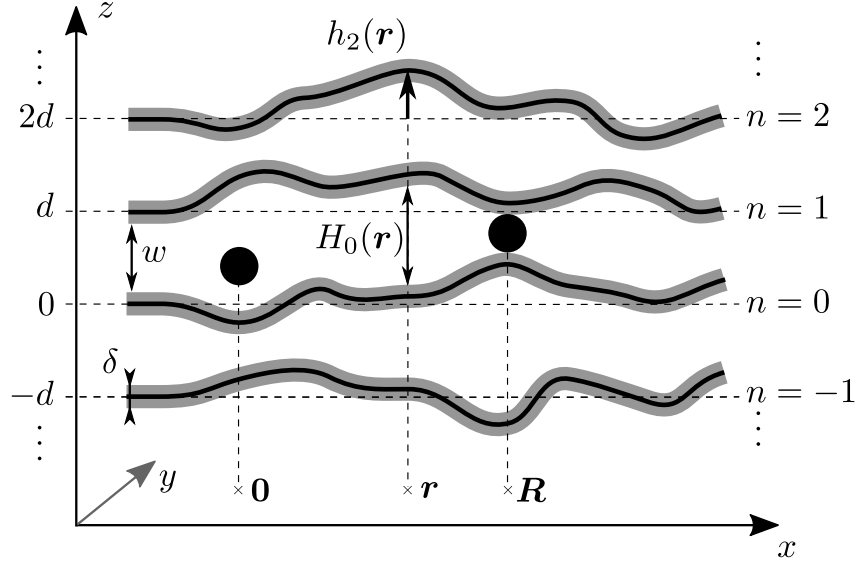


Figure 3.1 – Parametrization of the lamellar phase (cross section). The membranes, of thickness δ , are drawn in gray and their midsurfaces are represented as black lines. The average lamellar spacing and water thickness are d and w , respectively. The layer displacements are described by the functions $h_n(\mathbf{r})$ and the gap between the layers by the functions $H_n(\mathbf{r})$, as indicated. Two colloidal particles are represented as black disks: the one on the left is a membrane-excluding colloidal particle having only excluded volume interactions with the membranes, the one on the right is a membrane-binding colloidal particle that sticks to the membranes.

Here, κ is the bending stiffness of the membranes and B is an effective compression modulus, which accounts for all the interactions between the layers. As such, nothing in the model prevents the layers to cross each other. We have simply assumed that the membrane undulations are gentle enough so that the Gaussian approximation of the curvature energy can be used [Hel73]. The bulk moduli for layer compression and layer curvature [Gen69] are $B_3 = Bd$ and $K = \kappa/d$, respectively.

It is convenient to work with dimensionless quantities. We use $k_B T$ to normalize the energies, $\xi = (\kappa/B)^{1/4}$ to normalize \mathbf{r} and all the lengths parallel to (x, y) , and $\xi_{\parallel} = \xi \sqrt{k_B T / \kappa}$ to normalize h_n and all the lengths parallel to z , including d , δ , w and the colloidal particles diameters, hereafter called a and b . From now on, unless otherwise specified, all quantities will be in dimensionless form (i.e., normalized). Thus, the Hamiltonian (3.2) becomes

$$\mathcal{H} = \sum_{n=0}^{N-1} \int d^2 r \left[\frac{1}{2} (\nabla^2 h_n)^2 + \frac{1}{2} (h_{n+1} - h_n)^2 \right]. \quad (3.3)$$

It is also convenient to work in Fourier space. We thus define

$$h_{Q,q} = \frac{1}{L\sqrt{N}} \sum_{n=0}^{N-1} \int_0^L \int_0^L h_n(\mathbf{r}) e^{-iQnd} e^{-i\mathbf{q}\cdot\mathbf{r}} d^2 \mathbf{r}, \quad (3.4)$$

with L the lateral size of the membrane, and the inverse Fourier transform

$$h_n(\mathbf{r}) = \frac{1}{L\sqrt{N}} \sum_{Q,q} h_{Q,q} e^{iQnd} e^{i\mathbf{q}\cdot\mathbf{r}}, \quad (3.5)$$

Assuming periodic boundary conditions in all directions, the wavevectors are quantified according to $Q = 2\pi m/(Nd) \in [-\pi/d, \pi/d[$ and $\mathbf{q} = (q_x, q_y) = (2\pi m/L, 2\pi \ell/L)$, with $m, \ell \in \mathbb{Z}$. The elastic Hamiltonian takes then the simple form [Saf94]:

$$\mathcal{H} = \sum_{Q,q} \frac{1}{2} A(Q, q) h_{Q,q} h_{-Q,-q}, \quad (3.6)$$

with

$$A(Q, q) = q^4 + 2(1 - \cos Qd). \quad (3.7)$$

3.2.2 Fluctuations

The fluctuations of the lamellar phase (in the absence of colloidal particles) are obtained in a standard way by adding an external field $J_{Q,q}$ to the partition function [CL95]:

$$\begin{aligned} Z[J] &= \int \left(\prod_{n=0}^{N-1} \mathcal{D}[h_n] \right) \exp \left(-\mathcal{H} + \sum_{Q,q} J_{-Q,-q} h_{Q,q} \right) \\ &= Z_0 \exp \left(\sum_{Q,q} \frac{J_{Q,q} J_{-Q,-q}}{A(Q, q)} \right), \end{aligned} \quad (3.8)$$

where Z_0 is the partition function of the lamellar phase and $\mathcal{D}[h_n]$ denotes functional integration over all shapes of membrane n . We shall denote by $\langle \dots \rangle$ the statistical average over the membrane fluctuations. By differentiation, we obtain

$$\langle h_{Q,q} h_{Q',q'} \rangle = \frac{\partial^2 \ln Z}{\partial J_{-Q,-q} \partial J_{-Q',-q'}} \Big|_{J=0} = \frac{\delta_{Q+Q'} \delta_{q+q'}}{A(Q, q)}. \quad (3.9)$$

The *gap* between layers p and $p+1$, at position \mathbf{r} , is given by

$$H_p(\mathbf{r}) = w + h_{p+1}(\mathbf{r}) - h_p(\mathbf{r}). \quad (3.10)$$

Its average $\langle H_p(\mathbf{r}) \rangle$ is w . Using eqns (3.5) and (3.9), we obtain its correlation function

$$\langle H_0(\mathbf{0}) H_p(\mathbf{r}) \rangle - w^2 = \frac{2}{NL^2} \sum_{Q,q} \frac{1 - \cos Qd}{A(Q, q)} e^{iQpd} e^{i\mathbf{q}\cdot\mathbf{r}} \equiv \frac{G_p(r)}{2\pi}, \quad (3.11)$$

where the factor 2π was introduced for later convenience. In the thermodynamic limit,

$$G_p(r) = \frac{1}{\pi} \int_{-\pi}^{\pi} d\phi \int_0^{\infty} dq \frac{q(1 - \cos \phi) \cos(p\phi) J_0(qr)}{q^4 + 2(1 - \cos \phi)}, \quad (3.12)$$

with, in particular, $G_0(0) = 1$, $G_0(r) = 2J_1(r)K_1(r)$, where J_1 and K_1 are Bessel functions (see [Weia; Weib]), $G_p(0) = 1/(1 - 4p^2)$ and $G_p(\infty) = 0$.

It follows that the standard deviation of the gap, or, equivalently of the layer spacing, is given by $\sigma = \sqrt{G_0(0)/(2\pi)} = 1/\sqrt{2\pi}$. In dimensionful form, this gives $\sigma = \xi\sqrt{k_B T/(2\pi\kappa)}$ (in agreement with ref. [Pet+98]). Note that our Gaussian Hamiltonian (3.2) takes into account the repulsion of the layers by means of a soft harmonic repulsive potential. Since the layers cannot physically interpenetrate, the consistency of the model requires $w \gtrsim \sigma$, i.e., in dimensionless form, $w \gtrsim 1/\sqrt{2\pi} \simeq 0.4$. Note that this condition is true for the parameters given in Table 3.1, for both lipid and surfactant lamellar phases.

Let us also compute the correlation $\langle H_0(\mathbf{0})h_p(\mathbf{r}) \rangle$ between the membrane gaps and the layer displacements. This correlation will show up in the calculation of the deformation of the lamellar phase induced by the colloidal particles. We have

$$\langle H_0(\mathbf{0})h_p(\mathbf{r}) \rangle = \frac{1}{NL^2} \sum_{Q,q} \frac{e^{-iQd} - 1}{A(Q, q)} e^{iQpd} e^{iq \cdot \mathbf{r}} \equiv \frac{\Gamma_p(r)}{2\pi}. \quad (3.13)$$

In the thermodynamic limit,

$$\Gamma_p(r) = \frac{1}{2\pi} \int_{-\pi}^{\pi} d\phi \int_0^{\infty} dq \frac{q(e^{-i\phi} - 1)e^{ip\phi} J_0(qr)}{q^4 + 2(1 - \cos \phi)}, \quad (3.14)$$

with, in particular, $\Gamma_p(0) = 1/(4p - 2)$ and $\Gamma_p(\infty) = 0$.

3.3 Interactions between colloidal particles

Sens and Turner studied the interactions between particles in lamellar phases in a series of papers [PM97; TS97; TS98; ST01]. They described the particles by pointlike couplings inducing either a local pinching, a local stiffening or a local curvature of the membrane. Dealing with both thermotropic and lyotropic smectics, they used the three-dimensional smectic elasticity expressed in terms of a continuous layer displacement function [GP93]. This approach yields the asymptotic interaction between colloidal particles and thus the collective phase behavior when the colloidal particles are dispersed, but the obtained interaction has a peculiar divergence for colloidal particles in the same layer.

An approximate cure to this problem was proposed in ref. [TFL13] by the introduction of a high wavevector cutoff of the order of the inverse smectic spacing, i.e., a microscopic cutoff length at the scale where the continuous description fails. Another difficulty, inherent to linear couplings, is that the fluctuation corrections to the interactions are not accounted for. For smectics, since colloidal particles are always significantly larger than the smectic period, modeling a colloidal particle in a more realistic manner requires introducing a multipolar development [TS98], or an effective coat larger than the particle where the deformation is small enough to use a multipolar approach [TFL13]. Choosing the multipoles coefficients is difficult, however, in particular because enforcing strict boundary conditions make them in general dependent on the distances between the col-

loidal particles. Finally, as shown in ref. [SK03], rotational invariance and the associated non-linear effects can yield important modifications in the far-field deformations and thus in the interaction potentials.

In this study, as discussed in Section 3.1, we use a different approach, based on a discrete model for the layers. This approach applies to lyotropic lamellar phases, but not to continuous smectic phases. It has the advantage, however, that the colloidal particle-lamellar coupling is taken into account in an almost exact manner. We therefore expect to obtain reliable interactions at all separations, including in particular the fluctuation-induced corrections.

3.3.1 Membrane-binding colloidal particles

a. Partition function

Let us start by considering colloidal particles that adhere strongly to the neighboring bilayers, as the particle on the right in Fig. 3.1. We consider a first colloidal particle of diameter a binding to layers $n = 0$ and $n = 1$ at the in-plane position $(x, y) = \mathbf{0}$, and a second one of diameter b binding to layers $n = p$ and $n = p + 1$ at the in-plane position $(x, y) = \mathbf{R}$. We model their binding as a simple constraint on the gaps between their neighboring membranes on the axis normal to the undeformed membranes:

$$H_0(\mathbf{0}) = a, \quad H_p(\mathbf{R}) = b. \quad (3.15)$$

The partition function of the system (at fixed projected positions, $\mathbf{0}$ and \mathbf{R} , of the colloidal particles) is therefore given by

$$Z_{\text{bind}} = \int \left(\prod_{n=0}^{N-1} \mathcal{D}[h_n] \right) \delta(H_0(\mathbf{0}) - a) \delta(H_p(\mathbf{R}) - b) e^{-\mathcal{H}}. \quad (3.16)$$

Note that, in our treatment, in-plane and out-of-plane thermal fluctuations of the particle positions are decoupled: Brownian motion *along the layer normal* is accounted for in the model, implicitly for membrane-binding colloidal particles, since we integrate over the fluctuations of the layers to which the particles are bound, and explicitly for membrane-excluding particles (see Section 3.3.2), since we integrate over their heights. We thus obtain their effective interaction potential at fixed projected in-plane positions. In Section 3.5, we shall use this potential to investigate the collective behavior of the particles using a Monte Carlo Metropolis algorithm.

Note also that for the sake of simplicity we account for electrostatic effects only via an effective hard-core radius, measured in aqueous solution (see Section 3.5.2.)

Using the Fourier representation both of the delta functions and of the layer displace-

ments yields

$$\delta(H_0(\mathbf{0}) - a) = \int_{-\infty}^{\infty} \frac{d\lambda}{2\pi} e^{i\lambda(w-a) + \frac{i\lambda}{L\sqrt{N}} \sum_{Q,q} h_{Q,q}(e^{iQd}-1)} \quad (3.17)$$

$$\delta(H_p(\mathbf{R}) - b) = \int_{-\infty}^{\infty} \frac{d\mu}{2\pi} e^{i\mu(w-b) + \frac{i\mu}{L\sqrt{N}} \sum_{Q,q} h_{Q,q}(e^{iQd}-1)e^{iQpd}e^{i\mathbf{q}\cdot\mathbf{R}}} \quad (3.18)$$

The partition function then reads

$$Z_{\text{bind}} = \int \left(\prod_{n=0}^{N-1} \mathcal{D}[h_n] \right) \frac{d\lambda}{2\pi} \frac{d\mu}{2\pi} e^{i\lambda(w-a) + i\mu(w-b)} \\ \times e^{-\sum_{Q,q} \left[\frac{1}{2} A(Q,q) h_{Q,q} h_{-Q,-q} - h_{Q,q} S_{-Q,-q} \right]}, \quad (3.19)$$

with

$$S_{Q,q} = i\lambda \frac{e^{-iQd} - 1}{L\sqrt{N}} + i\mu \frac{e^{-iQd} - 1}{L\sqrt{N}} e^{-iQpd} e^{-i\mathbf{q}\cdot\mathbf{R}} + J_{Q,q}, \quad (3.20)$$

where we have added an external field $J_{Q,q}$ that will be used to compute the average deformation of the lamellar phase in the presence of the colloidal particles. Performing the Gaussian integrals, and discarding irrelevant constant factors, yields

$$Z_{\text{bind}} = \int d\lambda d\mu e^{i\lambda(w-a) + i\mu(w-b)} e^{\frac{1}{2} \sum_{Q,q} \frac{1}{A(Q,q)} S_{Q,q} S_{-Q,-q}} \\ = (\det M)^{-1/2} e^{-\frac{1}{2}(s,s') M^{-1}(s,s')^T + \frac{1}{2} \sum_{Q,q} \frac{1}{A(Q,q)} J_{Q,q} J_{-Q,-q}}, \quad (3.21)$$

where $M(R, p)$ is a symmetric 2×2 matrix with elements:

$$M_{11} = M_{22} = \frac{2}{NL^2} \sum_{Q,q} \frac{1 - \cos Qd}{A(Q,q)} = \frac{G_0(0)}{2\pi}, \\ M_{12} = \frac{2}{NL^2} \sum_{Q,q} \frac{1 - \cos Qd}{A(Q,q)} \cos(Qpd + \mathbf{q} \cdot \mathbf{R}) = \frac{G_p(R)}{2\pi}, \quad (3.22)$$

where we recognize the correlation function of the layer spacing, and

$$s = w - a + \frac{1}{L\sqrt{N}} \sum_{Q,q} J_{Q,q} \frac{e^{iQd} - 1}{A(Q,q)}, \quad (3.23)$$

$$s' = w - b + \frac{1}{L\sqrt{N}} \sum_{Q,q} J_{Q,q} \frac{e^{iQd} - 1}{A(Q,q)} e^{iQpd} e^{i\mathbf{q}\cdot\mathbf{R}}. \quad (3.24)$$

Taking the thermodynamic limit $N \rightarrow \infty$ and $L \rightarrow \infty$, we obtain for $J_{Q,q} = 0$, apart from an irrelevant constant factor,

$$Z_{\text{bind}} = \left(1 - G_p(R)^2 \right)^{-1/2} \\ \times \exp \left(-\pi \frac{(a-w)^2 + (b-w)^2 - 2G_p(R)(a-w)(b-w)}{1 - G_p(R)^2} \right). \quad (3.25)$$

b. Interaction free energy

The total free energy $-\ln(Z_{\text{bind}})$ of the system yields, after subtracting the value for infinitely separated colloidal particles, the interaction free energy of the two colloidal particles:

$$F_{\text{bind}}(R, p) = F_{\text{bind}}^{\text{Cas}}(R, p) + F_{\text{bind}}^{\text{el}}(R, p) \quad (3.26)$$

with

$$F_{\text{bind}}^{\text{Cas}} = \frac{1}{2} \ln(1 - G_p(R)^2), \quad (3.27)$$

$$F_{\text{bind}}^{\text{el}} = -\frac{2\pi G_p(R)}{1 + G_p(R)} \left[(a - w)(b - w) - \frac{1}{2} \frac{G_p(R)(a - b)^2}{1 - G_p(R)} \right]. \quad (3.28)$$

In order to get the dimensionful form of these interactions, one has to multiply these expressions by $k_B T$ and add an extra factor $\sqrt{\kappa B}/k_B T$ in front of $(w - a)(w - b)$ and $(a - b)^2$.

The interaction $F_{\text{bind}}^{\text{Cas}}$, which is thus directly proportional to the temperature, is a Casimir-like interaction, caused by the restriction of the layer fluctuations induced by the binding of the colloidal particles. Casimir interaction between extended manifolds immersed in correlated fluids, including smectic lamellar phase, are well-known (although usually difficult to measure) [FG78; Gam+09b; APP91; LK92]. A peculiarity, here, is that the objects (the colloidal particles) are smaller than the fluctuating elements of the medium (the layers). The interaction $F_{\text{bind}}^{\text{el}}$ is an athermal “elastic” interaction, proportional to $\sqrt{\kappa B}$ (it depends on temperature only through κ and B) and it is caused by the deformation of the layers induced by the colloidal particles. Note that if $a = b = w$, in which case the colloidal particles do not deform the layers, the elastic interaction vanishes while the fluctuation-induced Casimir interaction remains.

c. Average deformation

The average deformation of the lamellar phase is given by

$$\langle h_{-Q, -q} \rangle_{\text{bind}} = \left. \frac{\partial \ln Z_{\text{bind}}}{\partial J_{Q, q}} \right|_{J=0} = -\frac{1}{2} \left. \frac{\partial \left[(s, s') M^{-1}(s, s')^T \right]}{\partial J_{Q, q}} \right|_{J=0}, \quad (3.29)$$

yielding, for a layer n ,

$$\begin{aligned} \langle h_n(\mathbf{r}) \rangle_{\text{bind}} &= \frac{a - w - G_p(R)(b - w)}{1 - G_p(R)^2} \Gamma_n(r) \\ &+ \frac{b - w - (a - w)G_p(R)}{1 - G_p(R)^2} \Gamma_{n-p}(|\mathbf{r} - \mathbf{R}|), \end{aligned} \quad (3.30)$$

where Γ_n is the correlation function (3.13). The deformation $\langle h_n^{(1)}(\mathbf{r}) \rangle$ induced by just one colloidal particle, of diameter a , is obtained by taking $R \rightarrow \infty$ (infinite separation of the colloids) in the right-hand side of eqn (3.30). Since $G_p(R) = 0$ and $\Gamma_{n-p}(|\mathbf{r} - \mathbf{R}|) = 0$

in this limit, this deformation writes

$$\langle h_n^{(1)}(\mathbf{r}) \rangle_{\text{bind}} = (a - w)\Gamma_n(r). \quad (3.31)$$

Note that the deformation set by two colloidal particles is not simply the superposition of the deformations set by each individual colloidal particle. This non-linearity comes from the membrane thickness constraint imposed by the particles.

The deformation above a single colloidal particle, of diameter a , placed between layers 0 and 1, is therefore given by

$$\langle h_n^{(1)}(\mathbf{0}) \rangle_{\text{bind}} = \frac{a - w}{4n - 2}. \quad (3.32)$$

It is independent of the elastic constants since a , w , and h_n are normalized with respect to the same length.

For the consistency of our model, we must verify that the gap between the membranes bound to the colloidal particles and the adjacent ones remain positive despite the deformation. In particular, we must have $\langle H_1(\mathbf{0}) \rangle > 0$. Given eqns (3.32) and (3.10), this yields the consistency condition $0 < a < 4w$ for a colloidal particle of diameter a .

3.3.2 Membrane-excluding colloidal particles

a. Partition function and free energy

Let us now consider colloidal particles that interact with the membranes only through excluded volume forces, as the particle on the left in Fig. 3.1. We take a first colloidal particle of diameter a placed between layers $n = 0$ and $n = 1$ at the in-plane position $(x, y) = \mathbf{0}$, and a second one of diameter b placed between layers $n = p$ and $n = p + 1$ at the in-plane position $(x, y) = \mathbf{R}$. We model their presence in between the layers by imposing that the gaps between their neighboring membranes, on the axis normal to the undeformed membranes, cannot be smaller than their diameter. Such a constraint corresponds to the Hamiltonians of the infinite well type:

$$\mathcal{H}_a(z_a) = \begin{cases} 0 & \text{if } z_a \in [z_0(\mathbf{0}) + \frac{\delta+a}{2}, z_1(\mathbf{0}) - \frac{\delta+a}{2}], \\ +\infty & \text{otherwise,} \end{cases} \quad (3.33)$$

$$\mathcal{H}_b(z_b) = \begin{cases} 0 & \text{if } z_b \in [z_p(\mathbf{R}) + \frac{\delta+b}{2}, z_{p+1}(\mathbf{R}) - \frac{\delta+b}{2}], \\ +\infty & \text{otherwise,} \end{cases} \quad (3.34)$$

where z_a (resp. z_b) is the height of the particle of diameter a (resp. b) and $z_p(\mathbf{r}) = pd + h_p(\mathbf{r})$ is the height of the center of the membrane number p at the in-plane position \mathbf{r} .

The partition function, at fixed projected positions $\mathbf{0}$ and \mathbf{R} of the colloidal particles,

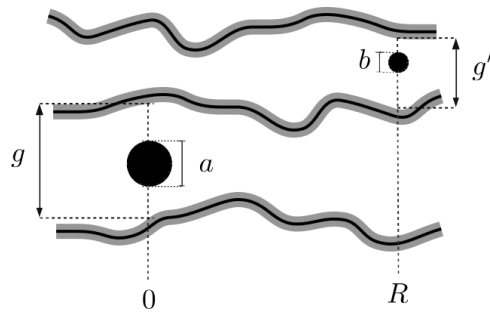


Figure 3.2 – Zoom on two colloids of diameter a and diameter b , interacting *via* excluded-volume interaction with the lamellae. We denote by g and g' the gaps at their respective position.

is then given by

$$Z_{\text{ex}} = \int \left(\prod_{n=0}^{N-1} \mathcal{D}[h_n] \right) dz_a dz_b e^{-[\mathcal{H} + \mathcal{H}_a(z_a) + \mathcal{H}_b(z_b)]}. \quad (3.35)$$

Integrating the Boltzmann weights associated to the infinite wells gives simply

$$\int dz_a e^{-\mathcal{H}_a(z_a)} = (H_0(\mathbf{0}) - a) \Theta(H_0(\mathbf{0}) - a), \quad (3.36)$$

$$\int dz_b e^{-\mathcal{H}_b(z_b)} = (H_p(\mathbf{R}) - b) \Theta(H_p(\mathbf{R}) - b), \quad (3.37)$$

where $H_0(\mathbf{0}) - a$ (resp. $H_p(\mathbf{R}) - b$) is the gap available to the first (resp. second) colloidal particle and the Heaviside functions Θ are such that the integrals vanish when the gaps are smaller than the colloidal particles diameters. Using the relation $\Theta(x-a) = \int_a^\infty dg \delta(x-g)$, the partition function becomes

$$Z_{\text{ex}} = \int \left(\prod_{n=0}^{N-1} \mathcal{D}[h_n] \right) \int_a^\infty dg \int_b^\infty dg' (H_0(\mathbf{0}) - a)(H_p(\mathbf{R}) - b) \times \delta(H_0(\mathbf{0}) - g) \delta(H_p(\mathbf{R}) - g') e^{-\mathcal{H}}. \quad (3.38)$$

Using the constraint $H_0(\mathbf{0}) = g$ and $H_p(\mathbf{R}) = g'$, then integrating on the layer displacement, we can map the problem onto that of binding colloidal particles, yielding

$$Z_{\text{ex}}(R, p) = \int_a^\infty dg \int_b^\infty dg' (g - a)(g' - b) Z_{\text{bind}}(g, g'), \quad (3.39)$$

where $Z_{\text{bind}}(g, g')$ is the partition function for binding colloidal particles of diameters g and g' , obtained by replacing a and b by g and g' in eq. (3.25). This expression can be understood if one thinks of integrating first over the gaps $g \in [a, \infty]$ and $g' \in [b, \infty]$ of the layers surrounding the colloidal particles, then over the other degrees of freedom at fixed gaps: the integration of the membrane degrees of freedom at fixed gaps gives the partition function (3.25) for membrane-binding colloidal particles, while the integration over the particle positions gives the entropic contributions $g - a$ and $g' - b$, see Fig. 3.2.

The interaction free energy for two membrane-excluding colloidal particles is therefore

given by

$$F_{\text{ex}}(R, p) = -\ln \frac{Z_{\text{ex}}(R, p)}{Z_{\text{ex}}(+\infty, p)}, \quad (3.40)$$

which can be easily calculated numerically by a double integration. Note that it is no longer possible here to extract separately an elastic contribution and a Casimir one.

b. Average deformation of the layers

The average deformation of the layers can be calculated by adding to the partition function (3.35) an external field J as in eqns (3.19)–(3.20). From the relation $\langle h_{-Q, -q} \rangle_{\text{ex}} = (1/Z_{\text{ex}}) \partial Z_{\text{ex}} / \partial J_{Q, q}|_{J=0}$, using $\partial Z_{\text{bind}}(g, g') / \partial J_{Q, q}|_{J=0} = \langle h_{-Q, -q} \rangle_{\text{bind}} \times Z_{\text{bind}}(g, g')$ yields in direct space:

$$\langle h_n(\mathbf{r}) \rangle_{\text{ex}} = \frac{1}{Z_{\text{ex}}} \int_a^\infty dg \int_b^\infty dg' (g - a)(g' - b) \langle h_n(\mathbf{r}) \rangle_{\text{bind}} Z_{\text{bind}}(g, g'), \quad (3.41)$$

with $\langle h_n(\mathbf{r}) \rangle_{\text{bind}}$ the average layer deformation at projected position \mathbf{r} for two colloidal particles of diameters g and g' . This expression can also be understood intuitively, since $\langle h_n(\mathbf{r}) \rangle_{\text{bind}} Z_{\text{bind}}$ is the integral over all the microstates corresponding to fixed gaps g and g' of $h_n(\mathbf{r})$ multiplied by $\exp(-\mathcal{H})$.

Since for one isolated binding colloidal particle of radius g we have $\langle H_0 \rangle_{\text{bind}} = g$ and $Z_{\text{bind}} = C \exp[-\pi(g - w)^2]$ (see eqn (3.25)), the average gap $\langle H_0^{(1)} \rangle$ set by one hard-core colloidal particle of radius a is given by

$$\begin{aligned} \langle H_0^{(1)} \rangle_{\text{ex}} &= \frac{\int_a^\infty (g - a) g e^{-\pi(g-w)^2}}{\int_a^\infty (g - a) e^{-\pi(g-w)^2}} \\ &= w + \left(2\pi(w - a) + \frac{2e^{-\pi(a-w)^2}}{\text{erfc}[\sqrt{\pi}(a - w)]} \right)^{-1}. \end{aligned} \quad (3.42)$$

In what follows, we compare the mediated interactions experienced by binding colloids to the one experienced by membrane-excluding colloids.

3.4 Typical results

3.4.1 Orders of magnitude

For the sake of completeness, we give here the parameters we can typically encounter in experiments. We consider two types of lyotropic lamellar phases: lamellar phases made of phospholipids such as the water/eggPC mixture, and lamellar phases made of surfactants and co-surfactants such as the C_{12}E_5 /hexanol/water mixture. Typical values for the elastic parameters of lipid and surfactant lamellar phases are given below and listed in Table 3.1.

Table 3.1 – Elastic parameters for typical lipid and surfactant membranes. The last three lengths are in dimensionless units.

	κ (J)	B (J m ⁻⁴)	$\xi; \xi_{\parallel}$ (nm)	δ	w	d
Egg PC	0.5×10^{-19}	1×10^{15}	2.7; 0.75	5.3	1.3	6.6
C ₁₂ E ₅	3.7×10^{-21}	6×10^8	50; 52	0.06	0.74	0.79

a. Lipid membranes

For lamellar phases made of egg PC lipids [Pet+98], the elastic constants are $\kappa \simeq 0.5 \times 10^{-19}$ J, and typically $B \simeq 1 \times 10^{15}$ J m⁻⁴ for $w \simeq 1$ nm, with $\delta \simeq 4$ nm and $d \simeq 5$ nm. We thus obtain $\xi = (\kappa/B)^{1/4} \simeq 2.7$ nm and $\xi_{\parallel} = \sqrt{k_B T}/(B\kappa)^{1/4} \simeq 0.75$ nm, yielding in dimensionless form $\delta \simeq 5.3$, $w \simeq 1.3$ and $d \simeq 6.6$. The structural formula of an egg PC lipid is given in Fig. 3.3.

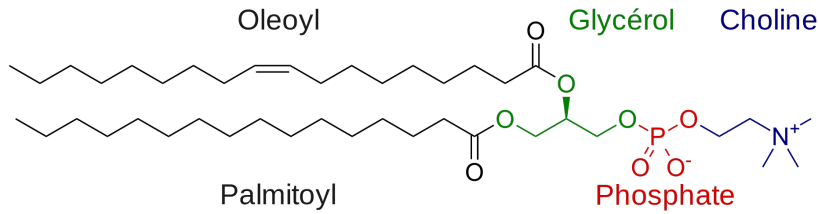


Figure 3.3 – Structural formula of an egg phosphatidylcholine (referred to as eggPC). Reproduced from Wikipedia.

b. Surfactant membranes

For the C₁₂E₅/hexanol/water system [FNR96; Bén+08], with typically a hexanol/C₁₂E₅ ratio of 0.35 and a membrane fraction of $\phi \simeq 7\%$, the elastic constants are $\kappa \simeq 3.7 \times 10^{-21}$ J and $B \simeq 6 \times 10^8$ J m⁻⁴, with $\delta \simeq 2.9$ nm, $d = \delta/\phi \simeq 41.5$ nm and $w \simeq 38.5$ nm. We thus obtain $\xi = (\kappa/B)^{1/4} \simeq 50$ nm, $\xi_{\parallel} = \sqrt{k_B T}/(B\kappa)^{1/4} \simeq 52$ nm, yielding in dimensionless form $\delta \simeq 0.055$, $w \simeq 0.74$ and $d \simeq 0.79$. The structural formula of C₁₂E₅ is given in Fig. 3.4.

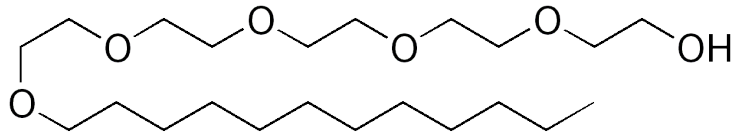


Figure 3.4 – Structural formula of C₁₂E₅, a non ionic surfactant. The addition of hexanol in the water/C₁₂E₅ mixture lowers the temperature at which the lamellar phase is stable [JS92]. Experiments can then be carried out at room temperature. Reproduced from Wikipedia.

3.4.2 Results for binding colloids

Lamellar phases made with lipids have a layer spacing typically comparable, or even smaller, than the membrane thickness $\simeq 4$ nm, so that only nano-particles will fit in such

systems (see Section 3.4.1a.). We show in Fig. 3.5a the typical interaction energy between membrane-binding colloidal particles and the corresponding lamellar phase deformation. The values correspond to egg PC lipids with colloidal particles of diameters $\simeq 3$ nm. Two colloidal particles in the same layer attract each other, while colloidal particles in different layers repel one another. The maximum interaction energies are large with respect to $k_B T$. When the colloidal particles are separated by more than one empty layer, their interaction becomes negligible compared to $k_B T$. For such lipid lamellar phases the Casimir component of the interaction energy is always negligible with respect to the elastic one. In Fig. 3.5b we show the corresponding interaction energy and associated lamellar phase deformation for two colloidal particles of different radii.

Lamellar phases made of surfactants can have a much larger layer spacing (see Section 3.4.1a.), so that larger colloidal particles can fit in. They also have weaker elastic constants, so that fluctuation effects are larger. We show in Figs. 3.5c and 3.5d the typical interaction energy and the corresponding lamellar phase deformation. The values correspond to $C_{12}E_5$ surfactants with colloidal particles of diameter $\simeq 27$ nm, as in the experiments of ref. [Bén+08]. The behaviors are similar to those of lipid membranes, but the energies are much smaller. Also the contribution of the Casimir interaction is no longer negligible.

3.4.3 Results for excluded-volume colloids

We now compare in Fig. 3.6a the interaction energies between membrane-excluding and membrane-binding colloidal particles for a lamellar phase made of egg PC lipids with colloidal particles of diameters $\simeq 3$ nm, which is indeed the size of gold nanoparticles in Ref. [Pan+11]. In Fig. 3.6b, we compare the interaction energies between membrane-excluding and membrane-binding colloidal particles for a lamellar phase made of $C_{12}E_5$ surfactants with colloidal particles of diameter $\simeq 27$ nm, as in Fig. 3.5 [Bén+08].

In the case of egg PC lipids, the colloidal particles diameters are much larger than the average water thickness. Then, the configurations that are effectively sampled by the fluctuations do not significantly depend on whether the colloidal particles stick to the layers or not, as spreading the layers further away from the colloidal particles costs a large energy. This is why the interaction energies for the membrane-excluding and membrane-binding cases are very close (see Fig. 3.6a).

Conversely, in the case of $C_{12}E_5$ surfactants, the colloidal particles diameters are taken slightly smaller than the average water thickness. Therefore, the interaction between membrane-excluding colloidal particles is of pure fluctuating (Casimir) origin: in the absence of fluctuations, the colloidal particles sit anywhere in between the layers without producing any deformation, whatever their distance. As seen in Fig. 3.6b, in this case, the interaction energies for the membrane-excluding and membrane-binding cases differ significantly, even though the overall behavior is similar. Due to the various contributions to the free energies (elastic deformations, entropy associated to the fluctuations of the membranes and of the colloidal particles) and their differences in the two situations, it is difficult to get a qualitative understanding of the interaction energy variations between the two situations.

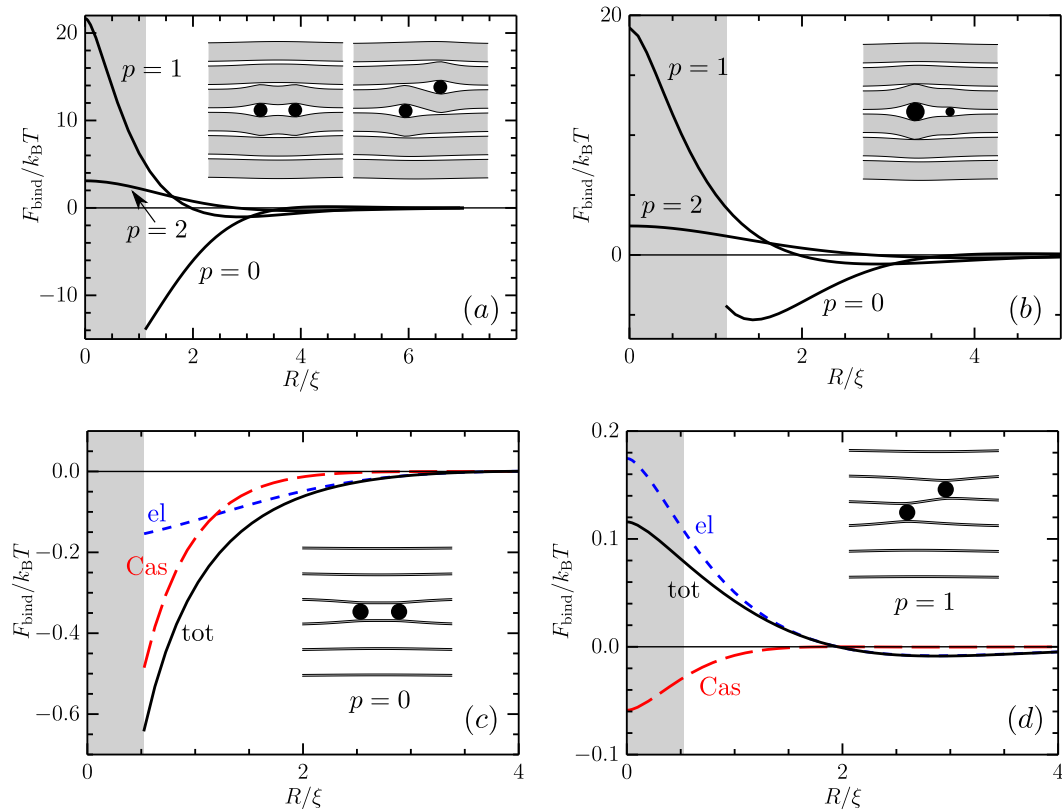


Figure 3.5 – (a) Interaction energy as a function of separation for membrane-binding colloidal particles with diameters $a = b = 3w$ in a lamellar phase with the parameters of egg PC (see Section 3.4.1a.). The Casimir contribution to the interaction is less than 1% of the elastic part. colloidal particles in the same layer ($p = 0$), one layer apart ($p = 1$), two layers apart ($p = 2$). Insets: Deformations of the lamellar phase, calculated numerically using eqn (3.30), for $R/d = 1.5$ and $N = 100$. The membranes, in gray, and the colloidal particles, in black, are represented at scale. (b) Same as (a) for colloidal particles of diameter $a = 4w$ and $b = 2w$. (c) Interaction energy as a function of separation for binding colloidal particles of diameter $a = b = 0.7w$ placed in the same layer in a lamellar phase with the parameters of C₁₂E₅ (see Section 3.4.1b.). Black solid line (tot): total interaction F_{bind} . Blue dashed line (el): elastic interaction $F_{\text{bind}}^{\text{el}}$. Red long-dashed line (Cas): Casimir interaction $F_{\text{bind}}^{\text{Cas}}$. Inset: numerically calculated deformation of the lamellar phase, using eqn (3.30), for $R/d = 1.5$ and $N = 100$. The membranes and the colloidal particles are represented at scale. (d) Same but for colloidal particles one layer apart ($p = 1$).

3.5 Comparison with experiments

We now focus on only one experimental system made of silica colloidal particles of diameter 27 nm embedded in a lamellar phase made of the C₁₂E₅/hexanol/water mixture described in Section 3.4. The structure factor related to the particles position in this system has been obtained with small-angle X-ray scattering [Con10]. In order to have clues on the interaction type between the silica beads and the lamellae (membrane-binding or membrane-excluding), we perform Monte Carlo simulations (for each type of interactions) of an ensemble of particles subjected to the pairwise forces we have analytically computed in Section 3.3. The structure factors obtained in the different simulations are

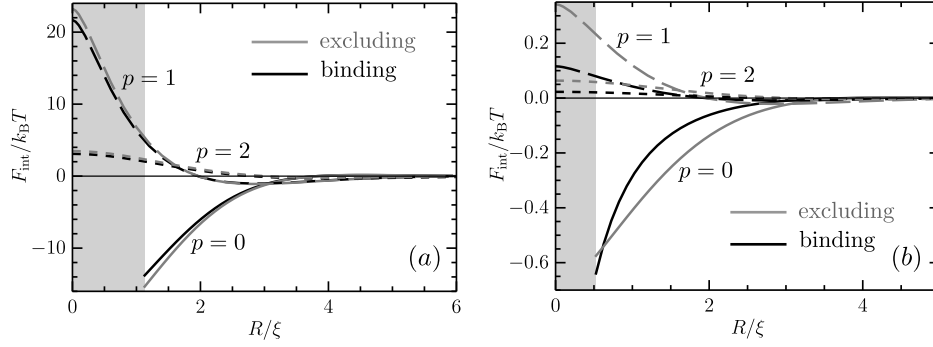


Figure 3.6 – Comparison between the interaction energies of membrane-excluding colloidal particles (gray lines) and of membrane-binding colloidal particles (black lines, same curves as in Fig. 3.5a, c and d). Solid lines: colloidal particles in the same layer ($p = 0$), long-dashed lines: colloidal particles one layer apart ($p = 1$), dashed-line: colloidal particles two layers apart ($p = 2$). (a) Lamellar phase with the parameters of egg PC and colloidal particles of diameter $a = b = 3w$. (b) Lamellar phase with the parameters of $C_{12}E_5$ and colloidal particles of diameter $a = b = 0.7w$.

then compared to the experimental ones. This offers a way to discriminate between the different possible colloid-lamellae interactions.

Let's write here a small comment on the Monte Carlo simulations (details are given in Appendix A.1). Specifically, we do not simulate the different layers, since we can use the effective potential that we have calculated in the previous sections, which effectively integrates out the layers. We model the colloidal particle-lamellar phase system as a finite number M of stacks of identical colloidal particles orthogonal to z -direction, each one consisting of the same finite number N of particles confined in a disk of radius R_d . We suppose that the particles cannot change stack. Once we have fixed the layer in which a particle diffuses, we know its two-body interaction with its neighbors from any layers. Of course, forces are not really pairwise additive, neither in the model, nor in the experimental system. However, we expect that such a simulation yields trustworthy results for low density systems. The pairwise interaction we have computed takes into account fluctuation-induced forces transmitted by the layers, and the vertical diffusion of the beads.

We will first show some typical snapshots of the simulations, and then we compare the different structure factors to the real system ones.

3.5.1 Monte Carlo simulations for colloids in the $C_{12}E_5$ lamellar phase

In Fig. 3.7 we show a typical Monte Carlo snapshot of three successive layers (blue, red, and green disks) for membrane-excluding colloidal particles of diameter 27 nm embedded in a lamellar phase with the parameters of $C_{12}E_5$. The corresponding interaction energy is displayed in Figs. 3.5c and 3.5d. To the membrane-mediated energy we added a hard core interaction with an effective core diameter of 34 nm, as measured in aqueous solution (see Ref. [Bén+08; Zak+19]). Clearly, the colloidal particles in each layer tend to

aggregate in large clusters. Moreover, the clusters are statistically anticorrelated between adjacent layers: clusters in a layer tends to face voids in the adjacent layers. This organization originates from the attractive interaction between two colloidal particles sitting in the same layer (as shown in Fig. 3.5c), and from the repulsive interaction between two colloidal particles sitting one layer apart (see Fig. 3.5d).

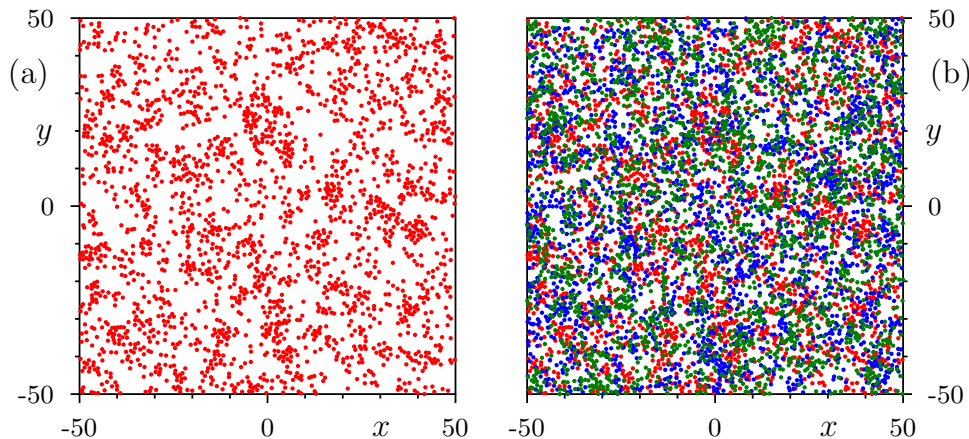


Figure 3.7 – Typical snapshot of a Monte Carlo simulation of the membrane-excluding colloidal particles (after equilibration) for the parameters of $C_{12}E_5$ (see Section 3.4.1b.) for particles of diameter $a = 27$ nm and hard-core distance between colloidal particles of 34 nm. The colloidal particles volume fraction is 2%. The colloidal particles in one layer are represented as red disks. The blue and green disks represent the colloidal particles in the two adjacent layers. The diameter of the disks corresponds to the hard-core distance. (a) Colloidal particles in one layer. (b) Red disks: same layer of colloidal particles as in (a); blue and green disks: colloidal particles in the two layers flanking the red one for the same snapshot. *Simulation by Paolo Galatola.*

For the same parameters, the membrane-binding colloidal particles tend also to form clusters, although they are less marked (see Fig. 3.8). To assess them, we show in the inset of Fig. 3.8 the intra-layer structure factor S_0 (solid line). For comparison, we also show (dashed line) the structure factor S_0 obtained by switching off the interactions, thus taking into account only the hard core contribution. The first maximum at $q \simeq 0.16 \text{ nm}^{-1}$ corresponds to the hard core diameter of the particles. At smaller wavevectors, the structure factor in the presence of interaction shows a rise for $q \rightarrow 0$ that is absent in the case of hard core only interaction (dashed line). This can be understood as due to the form factor of random fluctuating clusters with a distribution of sizes down to $2\pi/q_{\min}$, where q_{\min} is the position of the minimum of S_0 close to $q = 0$. Indeed, q_{\min} gives an upper estimate of the size of the peak at $q = 0$. In the snapshot we have indicated this size by surrounding small clusters in two adjacent layers. This is compatible with the fact that, as shown in Fig. 3.6b, the interaction energy for membrane-binding colloidal particles has the same overall shape, but lower amplitude in comparison with membrane-excluding ones. Increasing the particle concentration results in a similar cluster structure in a denser system.

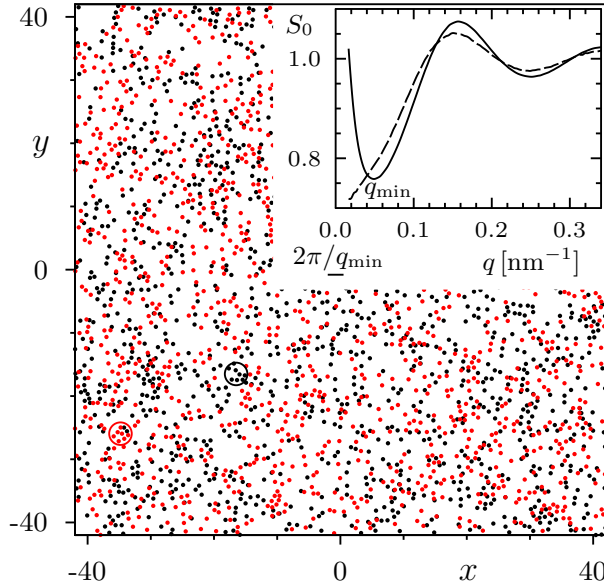


Figure 3.8 – Typical snapshot of a Monte Carlo simulation of membrane-binding colloidal particles (after equilibration) for the same parameters as in Fig. 3.7. The black disks are in one layer and the red disks in an adjacent one. The diameter of the disks corresponds to the hard core of the colloidal particles. Inset: structure factor $S_0(q)$ inside the layers, in the presence of the interparticle interaction (continuous line) and only with hard core repulsion (dashed line), as a function of the in-plane wavevector q . The position q_{\min} of the minimum of $S_0(q)$ gives an upper estimate of the width of the peak at $q = 0$. The corresponding length $2\pi/q_{\min}$ is materialized by the bar and by the diameter of the black and red circles surrounding small clusters in two adjacent layers. *Simulation by Paolo Galatola.*

3.5.2 Experimental structure factors

We compare the experimental structure factors with the structure factors from the Monte Carlo simulations, described in Appendix A.1. Clearly, using only the hard-core repulsion (dashed blue line in Fig. 3.9a), with an effective core diameter of 34 nm describing the interaction measured in aqueous solution (the core is larger than the nominal diameter of 27 nm due to the electrostatic repulsion), does not fully account for the experimental data on the left of the structure peak ($q < 0.15 \text{ nm}^{-1}$).

Including the membrane-binding colloidal particles interaction, with the elastic parameters of C_{12}E_5 surfactants given in Table 3.1, captures quantitatively, with no adjustable parameters, the experimental points down to the small-angle increase ($q > 0.05 \text{ nm}^{-1}$). The latter ($q < 0.05 \text{ nm}^{-1}$) is described qualitatively by the complete model, while it is obviously absent in a hard-core system.

The membrane-excluding model (Fig. 3.9b) also predicts a small-angle increase, which is however less important than for the binding case; overall, this model agrees less well with the experimental data.

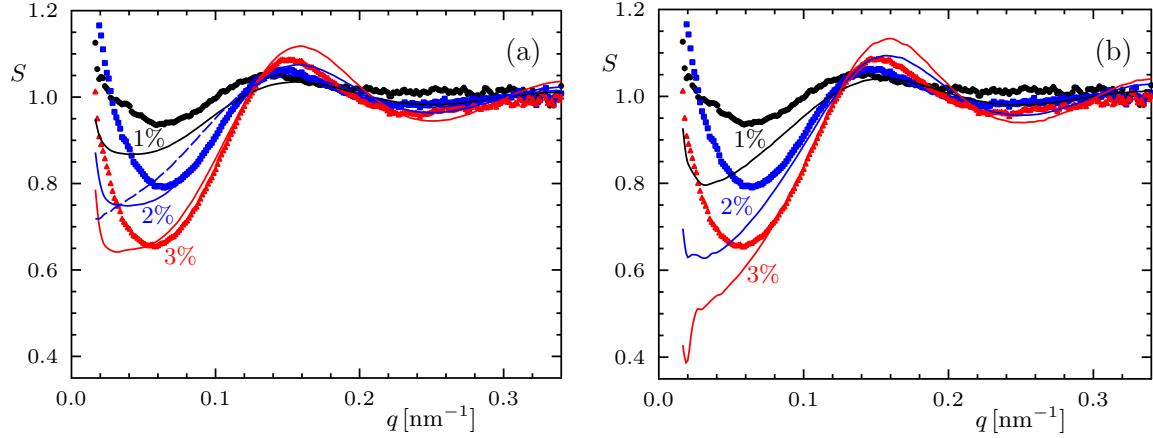


Figure 3.9 – Experimental in-plane structure factors, as a function of the in-plane wavevector q , for silica nanoparticles confined in lamellar phases at three different volume concentrations ϕ [Bén+08] (black circles: $\phi = 1\%$; blue squares: $\phi = 2\%$; red triangles: $\phi = 3\%$) and Monte Carlo predictions according to our model with the parameters given in Section 3.4.1b. (solid lines). (a) Membrane-binding inclusions. (b) Membrane-excluding inclusions. Black solid lines: $\phi = 1\%$; blue solid lines: $\phi = 2\%$; red solid lines: $\phi = 3\%$. The dashed blue line in (a) is the simulated structure factor for $\phi = 2\%$ with only hard-core interactions. To obtain convergence, in the membrane-binding [resp. membrane-excluding] case, the Monte Carlo averages are performed on 10^7 (resp. 2×10^8) steps after equilibration on a system consisting of 7 layers having a reduced radius $R = 20$ (resp. $R = 80$). The membrane-excluding Monte Carlo simulations at 3% volume fraction (figure b) are likely affected by small finite volume effects at the smallest wavevectors.

3.6 Conclusion

We treated in detail the interaction between hard spherical inclusions in lyotropic smectics, for the limiting cases of membrane-excluding and membrane-binding particles. In both cases, the interaction range is of the order of the elastic correlation length $\xi = (\kappa/B)^{1/4}$ defined in Section 3.2. For membrane-binding colloidal particles of identical diameters a , the interaction energy (3.26) at contact, in the limit $a \ll \xi$, is approximatively given, in dimensionful form, by

$$F_{\text{bind}}^{\text{contact}} \simeq \frac{k_B T}{2} \log C + \frac{\pi}{4} (C - 4) \sqrt{B\kappa} (a - w)^2, \quad (3.43)$$

where

$$C = \left(\frac{a}{\xi}\right)^2 \left[\ln\left(\frac{\xi}{a}\right) + \frac{3}{4} + \log 2 - \gamma \right], \quad (3.44)$$

with $\gamma \simeq 0.577$ the Euler constant. This contact energy varies from tens of $k_B T$ for lipid systems to fractions of $k_B T$ in dilute phases of single-chain surfactants. For systems of the latter type we compared our predictions to experimental structure factors measured at three concentrations of silica nanoparticles in a dilute lamellar phase of nonionic surfactant, C_{12}E_5 here. We obtain semi-quantitative agreement with no adjustable parameters. Remarkably, this agreement is significantly better for the membrane-binding model than for the membrane-excluding one, consistent with strong adsorption of these surfactants

onto silica surfaces, a result widely accepted in the literature (see, e.g., the discussion in ref. [SAK10].)

The presence of the particles acts as a constraint on the membrane fluctuations, leading to an attractive “Casimir-like” component of the interaction, which is quite significant (or even dominant) for the surfactant systems discussed above.

For strongly attractive systems, the liquid phase of particles is unstable with respect to aggregation. The peculiar nature of the interaction (overall attractive in the plane of the layers and repulsive across the layers) leads to the formation of flat, compact and size-limited aggregates. As a concrete application, one could consider dispersing the particles into a host lamellar phase with suitably chosen parameters so that they remain well separated, and then inducing their aggregation by an external stimulus (temperature change, controlled drying, etc) that increases the interparticle attraction. The resulting assemblies could then be stabilized by various strategies [BET16].

Part II

Surface tension of active fluids

An elusive quantity?

Self-propelled active particles are driven out of equilibrium through a dissipative exchange of energy and momentum with their environment, which endows them with anomalous thermomechanical properties [Di +10; Sok+10; Mal+14; TYB14; YMM14; Sol+15; Bia+15; SGJ17; Jun+17; Viz+17; Fil+17]. Among these, the pressure exerted by active systems on their confining vessels has recently attracted a lot of interest [Mal+14; TYB14; YMM14; Sol+15; Nik+16; SJ16; MMM16; SGJ17; Jun+17; Fil+17; Gin+18; Fal+16]. In particular, the existence of an equation of state for the pressure extends to a large subclass of these non-equilibrium and momentum-non-conserving systems. Their defining feature is a self-propulsion force whose dynamics is independent of the positional and angular degrees of freedom [Fil+17]. In particular, this includes the standard models of active particles, such as run-and-tumble particles (RTPs), active Brownian particles (ABPs) or active Ornstein-Uhlenbeck particles (AOUPs), in the presence of momentum-conserving pairwise forces. For such systems, macroscopic mechanical properties echo the equilibrium case with, for instance, equality of pressures in coexisting phases. There is thus hope of a generalized thermodynamics for these systems, which are the focus of this second part.

While pressure controls the bulk thermodynamic state of a system in equilibrium, its interfacial properties rely on surface tension, perhaps the most elusive thermomechanical quantity [Ber71; Mar+11] whose microscopic origin has been the topic of long-standing debates [RW82]. Surface tension indeed controls a wealth of phenomena, from the demix-

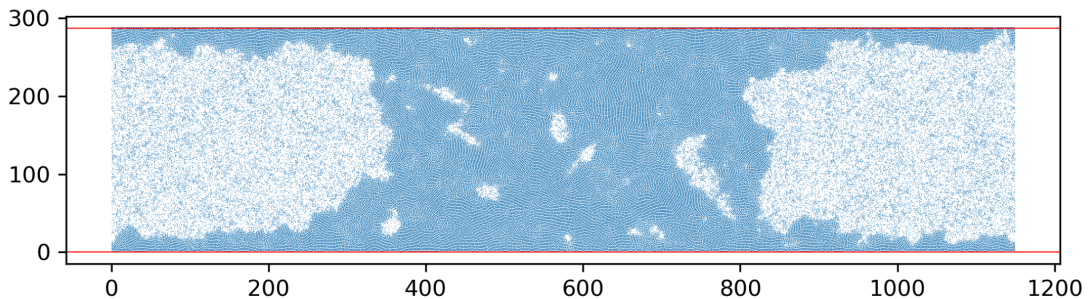


Figure 3.10 – Snapshot of a fluid of active Brownian particles confined by walls (red lines) along the vertical direction. Periodic boundary conditions are taken along the x -direction. Particles interact through pairwise forces. We observe a Motility-Induced Phase Separation (MIPS) between the vapor (light region) and the liquid (dark region). In steady state, the liquid completely wets the walls. *Image courtesy of Yongfeng Zhao.*

ing of binary mixtures to the wetting of surfaces, or the instability of thin films and jets. Given the atypical properties of active matter at interfaces, from the accumulation on hard walls to the wetting of soft gels by swarming bacteria, the fate of surface tension for active systems has naturally attracted attention [Bia+15; Pal+17]. In particular, the surface tension of active particles at a liquid-gas interface in a system undergoing Motility-Induced Phase Separation (MIPS) has been measured using an expression derived by Kirkwood and Buff for Hamiltonian systems [KB49; Buf55]. Despite stable interfaces [Bia+15; Sol+18; Pat+18], this liquid-gas surface tension has, somewhat surprisingly, been found negative [Bia+15]. Its thermodynamic role has nevertheless been confirmed: it controls the pressure drop through the boundary of a circular droplet of radius R through a Laplace pressure given by $\Delta P = \frac{\gamma}{R}$ [Sol+18]. This combination of surprising and familiar aspects of interfacial physics provides the incentive to clarify the microscopic origin of surface tension in these active systems and in particular its mechanical implications, which have been ignored so far.

Accounting for capillary and wetting phenomena in active matter is a formidable program which we attack by elucidating the interfacial properties of active fluids in contact with a solid boundary. To do so, in the absence of an established thermodynamic route, we will revert to mechanics. This second Part starts with an introductory chapter on surface tension where we review the different definitions of surface tension and their physical meaning. By introducing historical devices used to measure surface tension in equilibrium (see Chapter 4), we pave the road for a mechanical definition of surface tension for active fluids. In Chapter 5, regarding surface tension as a macroscopic force whose action is localized, we suggest a new approach based on the Virial to define and to compute the surface tension of active fluids. Finally, in Chapter 6, we present our *in silico* measurements of the surface tension of active fluids inspired by the setups presented in Chapter 4. We point out geometries in which such measurements are dressed by macroscopic forces specific to nonequilibrium systems. Chapter 6 will expose both new analytical results and new numerical results. The work presented in Chapter 6 arises from a collaboration with Yongfeng Zhao, Milos Knezevic, Adrian Daerr and Yariv Kafri. This work was accomplished under the joint supervision of Julien Tailleur and Frédéric van Wijland.

Chapter 4

What is surface tension?

We begin this second part with a selected review on surface tension. We first start with the macroscopic, phenomenological definitions of surface tension: surface tension as a surface energy and surface tension as a force on a contact line. Then, we say a few words about its mechanical origin. Finally, focusing on a specific setup inspired by the Langmuir balance [Lan17], we will relate the free energy definition to a force measurement. As we show, the mechanical approach we present in this chapter will prove relevant to define the surface tension of active fluids.

4.1 The macroscopic approach

4.1.1 First contact

In order to increase the contact area between two phases, an operator has to perform some work. At constant volume V and temperature T , and at fixed number of particles N , the work δW we have to provide to the system is $\delta W = \gamma \delta A$, with γ the surface tension and δA the newly created surface. Formally, the surface tension reads

$$\gamma = \left. \frac{\partial \mathcal{F}}{\partial A} \right|_{T,V,N}, \quad (4.1)$$

with \mathcal{F} the free energy of the system. The definition endows γ with the meaning of an energy per unit area.

Let us take a simple wetting example where thinking in term of energy per surface unit is relevant. We consider a system in equilibrium made of a liquid and its vapor, confined by a solid container. At our disposal, we have the solid-liquid, solid-vapor and liquid-vapor surface tensions, denoted γ_{SL} , γ_{SV} and γ_{LV} , respectively. If the condition $\gamma_{SV} > \gamma_{SL} + \gamma_{LV}$ is fulfilled, it means that the (free) energy cost of creating a solid-vapor interface is larger than the energy needed to create at the same time a liquid-vapor and a liquid-solid interface. In other words, it is favorable to have a liquid layer between the solid and the vapor: the liquid will completely wet the solid. Reciprocally, if we have

$\gamma_{SL} > \gamma_{SV} + \gamma_{LV}$, the solid ends up being completely dry.

Actually, this energetic approach of surface tension was developed alongside with the mechanical approach. In 1804, working on capillary phenomena, Thomas Young first suggested that the pressure drop $P_A - P_B$ across an interface is related to the surface tension and to the mean curvature of the interface:

$$P_A - P_B = \gamma \left(\frac{1}{R_1} + \frac{1}{R_2} \right), \quad (4.2)$$

R_1 and R_2 being the radii of curvature of the interface along two orthogonal directions [You05]. Later, Laplace gave mathematical grounds to this theory and thus attached his name to the formula which is now known as the Laplace-Young formula. Young has also addressed the theory of wetting on a solid. Typically, a drop of liquid laid on a solid features a contact angle θ with the solid at its wetting edges. In the case of partial wetting, as opposed to the total wetting seen previously, the formula that relates the three surface tensions and the wetting angle is the following:

$$\gamma_{SV} - \gamma_{SL} = \gamma_{LV} \cos \theta, \quad (4.3)$$

with $\theta \in [0, \pi]$. In what follows, we shall put aside the theory of wetting that would lead us too far. The interested reader is referred to [RW82; Gen85; GBQ04] and references therein.

4.1.2 Measurement: the Wilhelmy plate experiment

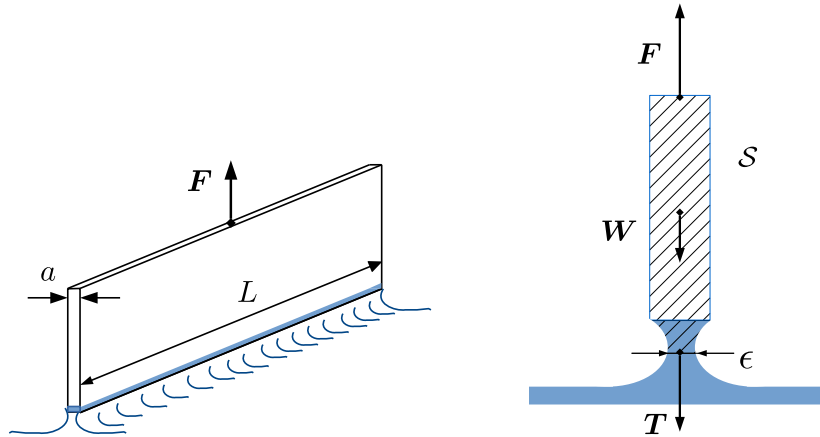


Figure 4.1 – **Left:** Plate of length L and width a , dipped in a liquid. **Right:** zoom on the system S and the forces applied on it.

Several methods are currently used to measure the surface tension. In order to measure the surface tension between two fluids, one can use the static, geometric approach suggested by the formula (4.2) and (4.3). For instance, knowing the pressures P_A and P_B in each phase, one can easily measure the radius of curvature of a spherical drop of fluid A inside fluid B and thus deduce the surface tension γ_{AB} . The pendant drop method relies on this measurement [Sta65].

We also remind the reader that the surface tension, being a surface energy, can also be interpreted as a linear force. This approach is widely used in practice to measure a liquid-vapor surface tension. We are going to focus on the Wilhelmy plate apparatus, which first, provides good insight into surface tension and, second, will prove relevant to define the surface tension of the liquid-vapor interface of active liquids undergoing a phase separation, see Section 6.3.1.

The Wilhelmy plate is made of an inert, easy to clean, material (typically platinum) of length L and of small width a . The coating of the material plays no role as long as the liquid has a strong affinity with the material. The plate is dipped in the liquid and we pull it until breaking the double interface we have created, see Fig. 4.1. Indeed, the theory of the measurement is not trivial [Mar+11], but it becomes easier to analyze when the plate detaches from the liquid. The plate is attached to a Newton-metre. It measures the force $\mathbf{F} = F\mathbf{e}_z$ needed to balance all the other forces that applies to a chosen system \mathcal{S} , see Fig. 4.1. The system \mathcal{S} is made of the plate (mass m_p) and of the small liquid drop (unknown mass for the moment) that will remain on the plate once the plate has detached from the bulk of the liquid. The liquid exerts, on the system \mathcal{S} , a tension $\mathbf{T} = -T\mathbf{e}_z$ that contains both the surface tension force and a hydrostatic pressure force. The system weight is $\mathbf{W} = -W\mathbf{e}_z$, $W > 0$. Denoting by ϵ the liquid width where it is the smallest, the total perimeter is $(2L + 2\epsilon)$ and the contact surface between \mathcal{S} and the liquid below is ϵL . Since the contact surface tends to 0 when the width of liquid that constitutes the double meniscus goes to 0, the only contribution to \mathbf{T} will be the surface tension force. With a quasi-static protocol, the sum of the forces on \mathcal{S} is null. The sum writes

$$F - W - T = 0 \quad (4.4)$$

which reads before breaking at time $t = t_b^-$

$$F(t_b^-) = W + 2\gamma_{LV}(L + \epsilon), \quad (4.5)$$

where γ_{LV} is the (liquid-vapor) surface tension that we want to determine. When the meniscus breaks, we have to wait for the system to relax to its new equilibrium position. Then the force is given by

$$F(t_b^+) = W. \quad (4.6)$$

Hence with this new equilibrium we can have access to γ_{LV} , which now reads

$$\gamma_{LV} = \frac{F(t_b^-) - F(t_b^+)}{2L}. \quad (4.7)$$

In Fig. 4.2a), we show a typical measurement of the force as a function of the height of the plate. For a fluid with surfactants, the air-liquid interface is stabilized and a vertical liquid film of constant width may appear between the plate and the liquid bulk. The force needed to pull the plate on a distance dz levels off (see Fig. 4.2b), and this force also yields the surface tension of the liquid-gas interface. With this apparatus we do not need to know the surface tension of the liquid-solid interface, nor the one of the solid-vapor

interface.

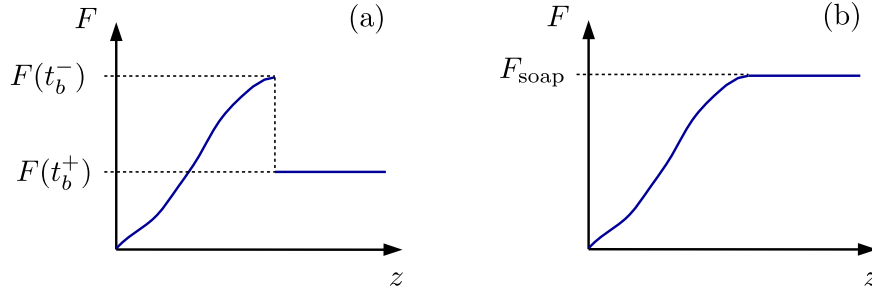


Figure 4.2 – Idealized measurements with the Wilhelmy plate experiment with and without surfactants. (a) Without surfactants. The interface breaks at time t_b . Pulling the plate then occurs at constant force (compensates exactly the weight). This is the most common case. (b) Pulling from a solution with surfactants (a soap film forms between the plate and the liquid). The force plateaus and the double meniscus does not break.

To summarize, we have presented here the macroscopic definitions of the surface tension. We now turn to its microscopic origin.

4.2 The microscopic origin

The starting point of the “Statistical Mechanical Theory of Surface Tension” by Kirkwood and Buff [KB49] is based on a mesoscopic observation: the system is anisotropic close to the interface and, as opposed to the isotropic and homogeneous bulk pressure in each phase, there is an excess average force per unit area (or average stress) close to the interface, in the direction parallel to the interface. This excess force per unit area can be easily visualized with molecular dynamics simulations, as presented in [Mar+11], adapted in Fig. 4.3. The tensor that encodes the (local) momentum flux density in all the directions is called the stress tensor. We recall that a momentum flux density is commensurable to a force per unit area, or a pressure. This tensor is commonly used in the literature, and this is why, for the sake of completeness, we define this tensor in this introductory chapter. We could however introduce surface tension by means of mesoscopic forces only and this is what we will do in Chapter 5.

Here we focus on the interface between two fluids. Measuring macroscopic forces in such a system is hard to perform without some solid probe (like the Wilhelmy plate for instance), which we do not want to consider in this simple two-fluid system. Introducing the concept of stress tensor can be useful if we want to consider the local force, or momentum flux, exchanged between two subsystems separated by a fictitious interface.

For pairwise interacting particles, the stress tensor is the sum of two contributions: a one-body (isotropic) contribution that comes from the flux of momentum across a surface¹, and a two-body contribution that comes from the pairwise forces between the particles. To assess the two-body component of the local stress tensor, we compute locally the force per unit area across a surface whose extension is comparable to the

¹The pressure of an ideal gas contains this one-body component only. Indeed, for an ideal gas, no force exists, neither between particles, nor between two subsystems separated by an imaginary interface.

intermolecular force range. The complete stress tensor, for a fluid in equilibrium with pairwise interactions, thus reads:

$$\sigma = -k_B T \rho(\mathbf{r}) I_d + \sigma^{(2)}, \quad (4.8)$$

with $\rho(\mathbf{r})$ the average local density, I_d the identity matrix, and $\sigma^{(2)}$ the stress coming from the particles interactions. The stress tensor σ is actually defined up to a zero divergence stress tensor whose consideration plays no role for the final value of the surface tension. These questions on the definition of the stress tensor have been closely examined by Schofield and Henderson in [SH82].

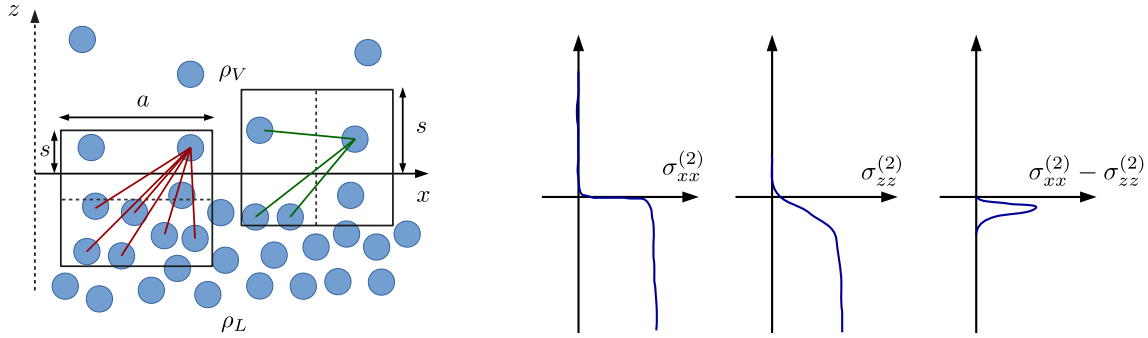


Figure 4.3 – **Left:** Schema of a liquid-vapor interface and links contributing to the stress tensor parallel to the interface (green), and orthogonal to the interface (red). **Right:** components of the two-body stress tensor $\sigma^{(2)}$ close to the interface. (Drawings adapted from Berry [Ber71] and Marchand *et al.* [Mar+11]).

Without performing the complete computation of Kirkwood and Buff, we can still write down a few equations suggested by Berry who explains that “the tangentially oriented test surfaces used to define the normal pressure *see* the depletion of molecules in the liquid surface before the normally oriented test surfaces used to define the tangential pressure” [Ber71]. In dimension $d = 2$, let us take a square test box, of side a , with a the typical range of the particles’ attractive interaction. As argued by Berry, the liquid-vapor surface tension originates from the anisotropy of the attractive forces. The repulsive forces being short range, their contribution is approximately isotropic [Ber71; Mar+11]. The one-body contribution is also isotropic. These isotropic contributions eventually simplifies in the computation of surface tension [KB49], and this is why we can focus on the attractive force contribution only. The virtual square box crosses the interface such that the length in the liquid is $(a - s)$ and the length in the vapor is s . To evaluate the different components of the stress tensor, we can count the bonds, joining two particles, that cross the test segment that splits the square in half. The bonds crossing the vertical segment contribute to σ_{xx} , while the bonds crossing the horizontal segment contribute to σ_{zz} . In an idealized vision of the interface, we consider the constant densities ρ_L and ρ_V of the liquid and the vapor on each side of the interface located at $z = 0$. The number of bonds contributing to σ_{xx} is simply

$$N_{\parallel} = \left(\frac{a}{2} (\rho_V s + \rho_L (a - s)) \right)^2, \quad (4.9)$$

while the number of bonds contributing to σ_{zz} is

$$N_{\perp} = \begin{cases} \rho_L \frac{a^2}{2} \left(as\rho_V + a\left(\frac{a}{2} - s\right)\rho_L \right), & \text{if } s \leq a/2 \\ \rho_V \frac{a^2}{2} \left(a(a-s)\rho_L + a\left(s - \frac{a}{2}\right)\rho_V \right), & \text{if } s > a/2 \end{cases} \quad (4.10)$$

The number of bonds in excess along x is thus

$$N_{\parallel} - N_{\perp} = \begin{cases} \left(\frac{a}{2}\right)^2 (\rho_L - \rho_V)^2 s^2, & \text{if } s \leq a/2 \\ \left(\frac{a}{2}\right)^2 (\rho_L - \rho_V)^2 (a-s)^2, & \text{if } s > a/2. \end{cases} \quad (4.11)$$

This number is always positive, and maximal when $s = a/2$ and null for $s = 0$ and $s = a$. This dependence on s is in agreement with the $\sigma_{xx} - \sigma_{zz}$ displayed in Fig. 4.3d. In the bulk of each phase we recover $N_{\parallel} - N_{\perp} = 0$, which corresponds to the isotropy of the stress tensor. This computation shows that there is an excess of attractive bonds in the direction parallel to the interface, thus creating a positive stress, or tension, in that direction.

At this point we would like to add an important comment. With the computation above, we see that we can correctly interpret the stress anisotropy in term of local excess tension if the system displays bulk phases in which the stress tensor is homogeneous and isotropic. In other words, the stress tensor always contains the pressure and surface tension contributions, but these two concepts appear only in the macroscopic limit when we *choose* to call ‘pressure’ the contribution of the stress tensor in the bulk, and ‘surface tension’ the stress in excess with respect to this bulk pressure close to the interface. Translated into a mathematical formula, the surface tension is defined as the macroscopic stress in excess with respect to the isotropic pressure P that already apply to a stripe of length ℓ ($\ell \gg a$), perpendicular to the interface:

$$\gamma_{LV} = \int_{-\ell/2}^{\ell/2} \sigma_{xx} dz + P\ell. \quad (4.12)$$

Using the fact that the normal component of the stress tensor σ_{zz} is constant everywhere (and equal to $-P$) because we have mechanical equilibrium in the z -direction, we get from Eq. (4.12) the celebrated Kirkwood-Buff formula [KB49]:

$$\gamma_{LV} = \int_{-\ell/2}^{\ell/2} (\sigma_{xx} - \sigma_{zz}) dz, \quad (4.13)$$

or more explicitly, after some calculations,

$$\gamma_{LV} = \frac{1}{2S} \iint d\mathbf{r}_a d\mathbf{r}_b \rho^{(2)}(\mathbf{r}_a, \mathbf{r}_b) \frac{(x_a - x_b)^2 - (z_a - z_b)^2}{r_{ab}} \frac{dU}{dr_{ab}}, \quad (4.14)$$

with S the interface area, $\mathbf{r}_{ab} = |\mathbf{r}_a - \mathbf{r}_b|$, $U(r)$ the potential of interaction, and $\rho^{(2)}(\mathbf{r}_a, \mathbf{r}_b) = \sum_i \sum_{j \neq i} \langle \delta(\mathbf{r}_a - \mathbf{r}_i) \delta(\mathbf{r}_b - \mathbf{r}_j) \rangle$ the pair correlation function. Eq. (4.14) is widely used in practice to compute the surface tension in molecular dynamics simulations [RL76].

We have thus presented the microscopical mechanical definition of surface tension. At the beginning of this chapter, we have also seen that the surface tension could be defined as the variation of the free energy with respect to a change of the interface area, while keeping all other parameters constant. These two definitions lead to the same results (see [OK60; NB77]), which confirms, in equilibrium, the interchangeability of the two approaches. The thermodynamic approach is treated by Ono and Kondo in [OK60]. Similar computations with the free energy were later performed by Navascués and Berry [NB77] to compute the surface tension between a fluid and a solid.

In the next section, we will focus on a purposely simple system, namely an ideal gas in a container. We will be able to explicitly link the transverse force on a wall to a surface tension derived from the free energy. This system will play the role of a model system on our route to the definition of the surface tension for active fluids.

4.3 Free energy and closed container

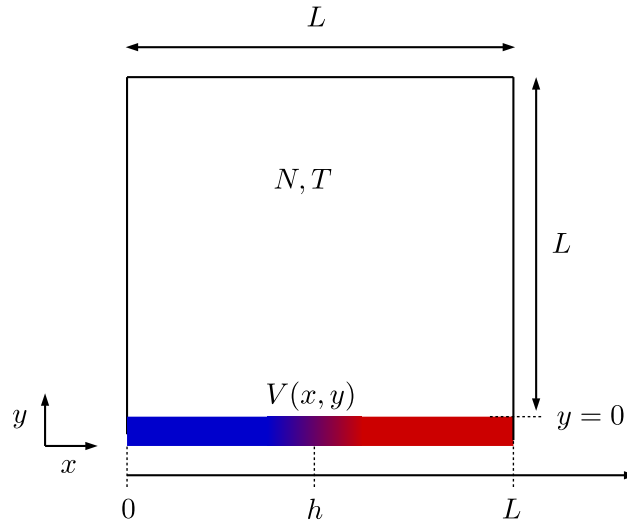


Figure 4.4 – Ideal gas at temperature T in a box. The bottom wall is made of a repulsive potential $V(x, y)$. In the domain $y \leq 0$, for $x \lesssim h$ we have $U = \frac{\lambda_1}{2}y^2$ (blue part), while for $x \gtrsim h$ we have $V = \frac{\lambda_2}{2}y^2$ (red part). The potential interpolates smoothly between the two domains.

We consider N non interacting particles in a two-dimensional box. The system is depicted on Fig. 4.4. The position of particle i is denoted by $\mathbf{r}_i = (x_i, y_i)$, with $0 \leq x_i \leq L$ and $y_i \leq L$. If $y_i \leq 0$, the particles are submitted to an external potential $V(x, y)$. This potential plays the role of a confining wall. We consider that the wall is made of two materials with a transition region that extends over a width w close to abscissa $x = h$, with $w \ll L$. More explicitly, for $y \leq 0$, the shape of the potential is the following:

$$V(x, y) = \begin{cases} \frac{\lambda_1}{2}y^2, & \text{if } x \in [0, h - w], \\ \frac{\lambda_2}{2}y^2, & \text{if } x \in [h + w, L], \\ g(x, y), & \text{if } x \in [h - w, h + w], \end{cases} \quad (4.15)$$

with $g(x, y)$ any smooth and monotonous interpolation of $V(x, y)$ between the points $h - w$ and $h + w$. For $y \geq 0$, $V(x, y) = 0$. The system is in equilibrium at temperature T . The local density of particles is thus given by the Boltzmann-Gibbs distribution

$$\rho(x, y) = Ce^{-\beta V(x, y)} \quad (4.16)$$

with $\beta = (k_B T)^{-1}$ and C a constant fixed by the normalization $\iint dx dy \rho(x, y) = N$. This normalization yields $C = N(\int_0^L dx \int_{-\infty}^L dy e^{-\beta V(x, y)})^{-1}$, or more precisely:

$$C = \frac{N/L^2}{1 + L^{-2} \int_0^L dx \int_{-\infty}^0 dy e^{-\beta V(x, y)}} = \frac{N/L^2}{1 + \frac{h\ell_1 + h\ell_2 + O(w\ell_1)}{L^2}}, \quad (4.17)$$

with $\ell_j = \sqrt{\pi/2} \sqrt{k_B T / \lambda_j}$ the penetration length of the particles in wall j (with $j = 1, 2$). In the thermodynamic limit, $N \rightarrow \infty$ and $L \rightarrow \infty$ with $N/L^2 = \rho_0$ fixed, and we have $C = \rho_0$. We can define the mechanical pressure exerted by the particles on the bottom wall as the force per unit length (we are in $d = 2$) exerted by the particles on the wall, projected along the normal \mathbf{e}_y . We can find this pedagogical computation for the pressure in [Sok10]. Since particles experience the force $-\nabla V$, the force they exert on the wall is ∇V . Since the potential vanishes for $y \geq 0$, we integrate the force density along y from $-\infty$ to any point y_b in the bulk. The pressure is thus defined as

$$P = \frac{1}{L} \int_0^L dx \int_{-\infty}^{y_b} dy C e^{-\beta V(x, y)} \partial_y V(x, y) \quad (4.18)$$

$$= \frac{1}{L} k_B T C \int_0^L dx e^{-\beta V(x, y=y_b)} \quad (4.19)$$

$$= k_B T C, \quad (4.20)$$

which reduces to $P = k_B T \rho_0$ in the thermodynamic limit, as expected. We also remark that the details of the potential V play no role in the thermodynamic pressure.

Similarly, we can compute the total transverse force f_{\parallel} applied by the particles on the bottom wall. The force has to be projected along x this time. We determine f_{\parallel} from

$$f_{\parallel} = \int_0^L dx \int_{-\infty}^{y_b} dy C e^{-\beta V(x, y)} \partial_x V(x, y) \quad (4.21)$$

$$= C \int_{-\infty}^{y_b} dy \left[\frac{e^{-\beta V(x=L, y)}}{-\beta} - \frac{e^{-\beta V(x=0, y)}}{-\beta} \right] \quad (4.22)$$

$$= k_B T C (\ell_1 - \ell_2), \quad (4.23)$$

which reduces to $f_{\parallel} = k_B T \rho_0 (\ell_1 - \ell_2)$ in the thermodynamic limit. How can we interpret this force? We remark that its sign depends on the relative repulsion of the particles on each part of the wall. For instance, if the left part ($j = 1$) is more repulsive than the right part ($j = 2$), we have $\ell_1 < \ell_2$ and the force is negative. If the bottom wall could move, it would go to the left. In other words, the length of the most repulsive part shrinks. Furthermore, the force does not depend upon the interpolation $g(x, y)$ between the two

parts of the wall. What we have here is actually an example of a Langmuir balance, used to measure a difference of surface tensions for fluids [Lan17]. The parallel force f_{\parallel} is the difference of the solid-gas surface tensions γ_1 and γ_2 of parts 1 and 2, respectively. Defining $\gamma_j = -k_B T \rho_0 \ell_j$, we have $f_{\parallel} = \gamma_2 - \gamma_1$.

To confirm this interpretation of the force f_{\parallel} , it is possible to rely on a free energy computation. Let us add a comment on the definition of surface tension of a solid-fluid interface at this stage. Experimentally, to increase the area of such an interface, the solid material can be stretched. Such a procedure yields to a displacement of atoms in the solid, which thus modifies the energy profile felt by the fluid at the solid interface. In short, surface free energy is stretching dependent and has to be distinguished from surface tension (or surface stress) which, multiplied by the area variation, yields the work needed to stretch the interface. This distinction has been pointed out by Shuttleworth in [Shu50] (see [DQ08; AS20] for a recent review). In our approach, the solid is not stretched but the variation of interaction area between the solid and the fluid should be thought as derived from a macroscopic displacement of the solid. This leads us to identify surface tension with surface energy, in equilibrium. Out of equilibrium however, surface tension will be accessed only through the forces (but no longer through the energy).

Let us come back to the free energy computation. To vary the length h by an amount dw while keeping L^2 (the volume), T and N constant, we provide, by definition, an energy $\gamma_1 dw$ and we recover $\gamma_2 dw$, such that the variation of the free energy of the system is $d\mathcal{F} = \gamma_1 dw - \gamma_2 dw$. The free energy is given by $\mathcal{F} = -k_B T \ln \mathcal{Z}^N$, with \mathcal{Z} the partition function of a single particle, defined up to a multiplicative constant:

$$\mathcal{Z} = \int_0^L dx \int_{-\infty}^L dy e^{-\beta V(x,y)} \quad (4.24)$$

$$= L^2 + \int_0^L dx \int_{-\infty}^0 dy e^{-\beta V(x,y)}. \quad (4.25)$$

We thus have:

$$\gamma_1 - \gamma_2 = \left. \frac{\partial \mathcal{F}}{\partial h} \right|_{L^2, T, N} = - \frac{k_B T N}{\mathcal{Z}} \left. \frac{\partial \mathcal{Z}}{\partial h} \right|_{L^2, T, N}. \quad (4.26)$$

The dependence on h is hidden in $V(x, y)$ whose definition actually depends on h . We can define $\tilde{V}(x - h, y) = V(x, y)$, with \tilde{V} independent of h , so that we have $\partial V / \partial h = \partial \tilde{V}(x - h) / \partial h = -\partial \tilde{V}(x - h) / \partial x$, which yields

$$\gamma_1 - \gamma_2 = - \frac{k_B T N}{\mathcal{Z}} \int_0^L dx \int_{-\infty}^L dy (-\partial_x e^{-\beta \tilde{V}}) \quad (4.27)$$

$$= - \frac{k_B T N}{\mathcal{Z}} \int_{-\infty}^L dy [e^{-\beta \tilde{V}(-h, y)} - e^{-\beta \tilde{V}(L-h, y)}] \quad (4.28)$$

$$= - \frac{k_B T N}{\mathcal{Z}} \int_{-\infty}^L dy [e^{-\beta V(0, y)} - e^{-\beta V(L, y)}]. \quad (4.29)$$

This equation suggests that we can split the contribution of each wall according to

$$\gamma_1 = -\frac{k_B T N}{\mathcal{Z}} \int_{-\infty}^0 dy e^{-\beta V(0,y)} = -k_B T \rho_0 \ell_1, \quad (4.30)$$

$$\gamma_2 = -\frac{k_B T N}{\mathcal{Z}} \int_{-\infty}^0 dy e^{-\beta V(L,y)} = -k_B T \rho_0 \ell_2, \quad (4.31)$$

where we have taken the thermodynamic limit to simplify N/\mathcal{Z} . This result confirms our identification of the contributions of f_{\parallel} , given in Eq. (4.23). The fact that the surface tension is negative should not be puzzling for two reasons. First, we also find a negative surface tension for hard spheres on a hard wall [NT79; HL99]. Second, we notice that in the case of a soft confining wall (like the potential V), the total volume occupied by the particles cannot be precisely defined. Keeping the occupied volume L^2 constant – instead of $L(L + \ell_1)$ for instance – when taking the derivative of the free energy with respect to h might seem somehow arbitrary. This leads us to define a solid-gas surface tension, among many others, up to an additive constant. In fact, the additive constant simplifies away when we want to compute the total force f_{\parallel} (a difference of surface tensions) felt by the wall (and which has a clear physical meaning!). These considerations were carefully addressed by Nijmeijer and Van Leeuwen in [NvL90].

Finally, in the case of the ideal gas, in the hard wall limit (stiffness $\lambda_j \rightarrow \infty$), the penetration length of the particles in the wall goes to 0 and the surface tension defined in (6.5) is 0. This makes sense since the free energy then only depends on the total volume occupied by the particles, on the number of particles and on the temperature T . These parameters being kept constant in the definition of the surface tension, we necessarily have $\gamma_{\text{ideal gas}} = 0$.

In the following chapters, we will focus on the surface tension of active systems. We will not be able to rely on the free energy to define the surface tension. However, the mechanical route is still accessible. In the next chapter, we present a new Virial construction to derive the solid-fluid surface tension for active systems. Macroscopic forces will be our starting point.

Chapter 5

A Virial approach to surface tension

In this chapter, we introduce a novel derivation for the microscopic expression of the liquid-solid and liquid-vapor surface tension. Our derivation is valid for both equilibrium systems and active liquids. The proofs we are going to present are based on a Virial approach. We first review the Virial derivation that relates the pressure to the fluid properties and we rigorously show its link to the microscopic description. Second, we derive the microscopic expression for the solid-liquid surface tension of an active fluid. The proof and the result are new. We also recover the Laplace law for an active fluid confined in a spherical container.

5.1 The Virial for the pressure

In order to introduce our derivation of the microscopic equation for the surface tension, we first derive the expression of pressure in an active fluid. The Virial derivation for the pressure in the literature was historically presented for particles with Hamiltonian dynamics or underdamped dynamics. The Virial is particularly convenient to derive the expression of the pressure of an ideal gas, or to derive the pressure of a fluid of particles with pairwise interactions. Indeed, the Virial route is usually concise, technically simple, and thus appealing. Nonetheless, several hypotheses are needed to follow this route and they are rarely mentioned in the literature. One of the goals of this chapter is to clarify the underlying hypotheses of the Virial. We choose here to reproduce the proof for overdamped particles in contact with a thermal bath. We also add the active force for more generality, on top of interactions and of thermal noise.

We consider a general case of N interacting active particles, confined in a box. The Langevin equation of motion for particle i reads

$$\dot{\mathbf{r}}_i = \mu \mathbf{F}_i^w + \mu \sum_j \mathbf{F}_{ji} + \mu \mathbf{F}_i^a + \sqrt{2k_B T} \mu \boldsymbol{\xi}_i, \quad (5.1)$$

with μ the mobility of particles, \mathbf{F}_i^w the force exerted by the wall on particle i , \mathbf{F}_{ji} the force exerted by particle j on particle i , \mathbf{F}_i^a the active force, $\boldsymbol{\xi}_i$ a zero mean, unit variance,

Gaussian white noise, and T is the temperature. We define $\mathcal{V} = \sum_i (\mathbf{r}_i \cdot \mathbf{r}_i)/2$ the quantity analogous to the Virial adapted to overdamped Langevin dynamics. If the particles are confined in a volume V_d , then the noise averaged quantity $\langle \mathcal{V} \rangle$ is constant in steady state, and its time derivative is zero. We thus have

$$0 = \sum_i \langle \mathbf{r}_i \cdot \frac{d\mathbf{r}_i}{dt} \rangle + \sum_i d\mu k_B T \quad (5.2)$$

$$= \left(\sum_i \langle \mathbf{r}_i \cdot \mathbf{F}_i^w \rangle + \sum_i \sum_j \langle \mathbf{r}_i \cdot \mathbf{F}_{ji} \rangle + \sum_i \langle \mathbf{r}_i \cdot \mathbf{F}_i^a \rangle \right) + dNk_B T, \quad (5.3)$$

where we have used Itô's lemma to obtain the second term in the rhs of Eq. (5.2) and d is the dimension of space.

The pressure is the force exerted by the walls on the fluid of particles. In Eq. (5.3), the pressure is thus hidden in the term $\sum_i \langle \mathbf{r}_i \cdot \mathbf{F}_i^w \rangle$. We want to arrive at the identity $\sum_i \langle \mathbf{r}_i \cdot \mathbf{F}_i^w \rangle = -dPV_d$, which is valid only when the range of the potential is much smaller than the system size, which is guaranteed in the thermodynamic limit of interest to us in this work.

We suggest two complementary approaches that will shed light on the vision we have of the Virial. First one can adopt a mesoscopic approach. A pedagogical computation from [WWG15] is reproduced here. Given a container of area S , one decomposes S in surface elements δS , and the sum is split accordingly:

$$\sum_i \langle \mathbf{r}_i \cdot \mathbf{F}_i^w \rangle = \sum_{\delta S} \sum_{i|\mathbf{r}_i \in \delta S} \langle \mathbf{r}_i \cdot \mathbf{F}_i^w \rangle. \quad (5.4)$$

In the limit $\delta S \rightarrow 0$, the \mathbf{r}_i are all identical when belonging to the same surface element. Now using the mesoscopic definition of the pressure, the average force exerted by a surface element is nothing but the pressure exerted by the container to confine the particles: $\sum_{i|\mathbf{r}_i \in \delta S} \langle \mathbf{F}_i^w \rangle \equiv -P \delta S \mathbf{n}$, with \mathbf{n} a unitary vector normal to the surface element δS . With this definition, Eq. (5.4) becomes

$$\sum_i \langle \mathbf{r}_i \cdot \mathbf{F}_i^w \rangle = \sum_{\delta S} \mathbf{r} \cdot \sum_{i|\mathbf{r}_i \in \delta S} \langle \mathbf{F}_i^w \rangle \quad (5.5)$$

$$= - \sum_{\delta S} \mathbf{r} \cdot \mathbf{n} P \delta S \quad (5.6)$$

$$= - \oint_S \mathbf{r} \cdot P d\mathbf{S}. \quad (5.7)$$

Finally, assuming that the pressure is homogeneous in the container, by using the Stokes-Ostrogradski theorem, one obtains

$$\sum_i \langle \mathbf{r}_i \cdot \mathbf{F}_i^w \rangle = -P \iiint_{V_d} \nabla \cdot \mathbf{r} d^3\mathbf{r} = -dPV_d. \quad (5.8)$$

Strictly speaking, the pressure is not homogeneous in the system, and close to the corners of the box the correlator $\langle \mathbf{r}_i \cdot \mathbf{F}_i^w \rangle$ is expected to vary a lot (over distances much smaller than the system size). The previous computation has actually swept under the rug the

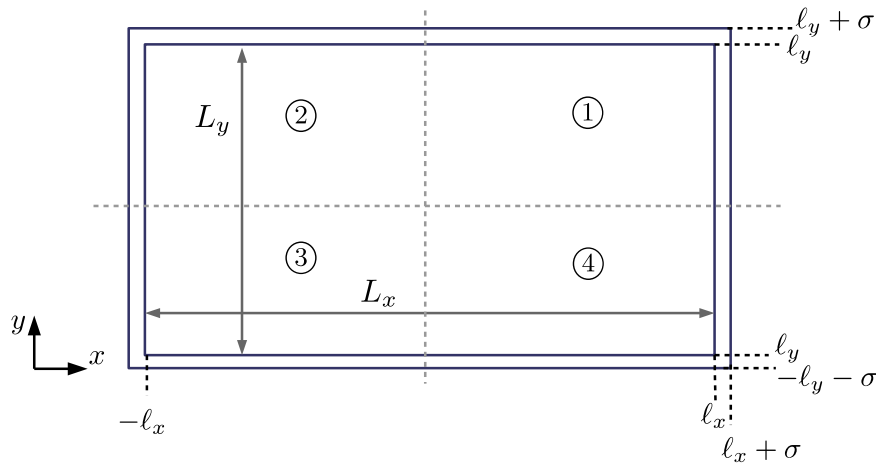


Figure 5.1 – Rectangular box that confines the active liquid. We demonstrate the Virial formula in this geometry.

difficulty of treating the edges of the container, and there is obviously a contribution to the force from the parts where the pressure varies rapidly.

The second derivation that establishes $\sum_i \langle \mathbf{r}_i \cdot \mathbf{F}_i^w \rangle = -dPV_d$ is new. For pedagogical reasons, we introduce here this rigorous proof to reinforce the foundations of the Virial approach, and to give a flavor of the coming computation on surface tension. We here express the sum with the particle density and we consider that the wall is described by a confining potential $V(\mathbf{r})$ that has a small spatial extension. The force is thus defined as the gradient of the potential: $\mathbf{F}^w = -\nabla V$. By means of this potential, we can rigorously write:

$$-\sum_i \langle \mathbf{F}_i^w \cdot \mathbf{r}_i \rangle = -\int d^d \mathbf{r} \rho(\mathbf{r}) \mathbf{F}^w(\mathbf{r}) \cdot \mathbf{r}, \quad (5.9)$$

where $\rho(\mathbf{r}) = \sum_i \langle \delta(\mathbf{r} - \mathbf{r}_i) \rangle$. Let us consider the two-dimensional case to simplify subsequent manipulations. Consider a rectangular box as depicted in Fig. 5.1, where the confining wall is defined as repulsive potential $V(x, y)$ that starts at position ℓ_x on the x axis, and extends to the position $\ell_x + \sigma$, where it diverges. Similarly for $x < 0$, the wall extends from $-\ell_x$ to $-\ell_x - \sigma$. On the y axis, the wall starts at position ℓ_y (resp. $-\ell_y$) and extends to position $\ell_y + \sigma$ (resp. $-\ell_y - \sigma$). The force exerted by the wall is thus null in the region $\mathbf{r} \in [-\ell_x, \ell_x] \times [-\ell_y, \ell_y]$. Let us focus on the term that comes from the wall located at $x = \ell_x$. The potential of the wall is translation invariant along y when $y_i \in [-\ell_y, \ell_y]$, i.e.: one can write $\mathbf{F}^w(\mathbf{r}) = \mathbf{F}^w(x)$ in this region of space. The term of interest reads:

$$-\int_{\ell_x}^{\ell_x + \sigma} \int_{-\ell_y - \sigma}^{\ell_y + \sigma} dx dy \rho(\mathbf{r}) \mathbf{F}^w(\mathbf{r}) \cdot \mathbf{r} = \int_{\ell_x}^{\ell_x + \sigma} \int_{-\ell_y}^{\ell_y} \rho(\mathbf{r}) (-\mathbf{F}^w(x)) \cdot \mathbf{r} dx dy + I_c \quad (5.10)$$

$$= \int_{\ell_x}^{\ell_x + \sigma} \int_{-\ell_y}^{\ell_y} \rho(x, y) \partial_x V(x) x dx dy + I_c \quad (5.11)$$

where

$$I_c = -\left(\int_{\ell_x}^{\ell_x+\sigma} \int_{-\ell_y}^{-\ell_y-\sigma} dx dy \rho(\mathbf{r}) \mathbf{F}^w(\mathbf{r}) \cdot \mathbf{r}\right) - \left(\int_{\ell_x}^{\ell_x+\sigma} \int_{\ell_y}^{\ell_y+\sigma} dx dy \rho(\mathbf{r}) \mathbf{F}^w(\mathbf{r}) \cdot \mathbf{r}\right) \quad (5.12)$$

is the contribution from the corners that is subdominant in the limit $\ell_y \rightarrow \infty$. If one wants to define the pressure as the average force exerted by the wall on the particles [Sok10; Sol+15], one has to take the limit $\ell_x \gg \sigma$. With a change of variable $x = \ell_x + \varepsilon$ in (5.11) the dominant term reads:

$$\int_{\ell_x}^{\ell_x+\sigma} \int_{-\ell_y}^{\ell_y} \rho(x, y) \partial_x V(x) x dx dy = \int_0^\sigma \int_{-\ell_y}^{\ell_y} \rho(\ell_x + \varepsilon, y) \partial_\varepsilon V(\ell_x + \varepsilon) (\ell_x + \varepsilon) d\varepsilon dy \quad (5.13)$$

$$\begin{aligned} &= \ell_x \int_0^\sigma \int_{-\ell_y}^{\ell_y} \rho(\ell_x + \varepsilon, y) \partial_\varepsilon V(\ell_x + \varepsilon) d\varepsilon dy \\ &\quad + \int_0^\sigma \int_{-\ell_y}^{\ell_y} \rho(\ell_x + \varepsilon, y) \partial_\varepsilon V(\ell_x + \varepsilon) \varepsilon d\varepsilon dy \end{aligned} \quad (5.14)$$

$$= \ell_x \int_{-\ell_y}^{\ell_y} \left(\int_0^\sigma \rho(\ell_x + \varepsilon, y) \partial_\varepsilon V(\ell_x + \varepsilon) d\varepsilon \right) dy + O(\sigma) \quad (5.15)$$

$$= \ell_x \int_{-\ell_y}^{\ell_y} P(y) dy + O(\sigma) \quad (5.16)$$

$$\sim \ell_x (2\ell_y) P_b, \quad (5.17)$$

where we have replaced the sum along y by $2\ell_y P_b$ when $\ell_y \rightarrow \infty$. To leading order, the pressure is indeed translational invariant along y , and the total force is simply the homogeneous bulk pressure P_b times the length of the wall. Now, we can perform the exact same computation for the opposite wall located at $x = -\ell_x$, and this will also give a contribution $\ell_x (2\ell_y) P_b$ to the sum (5.9). The walls located at $y = \pm\ell_y$ will each give a contribution of $\ell_y (2\ell_x) P_b$ to the sum. If we define the total lengths of the system as $L_x \equiv 2\ell_x$ and $L_y \equiv 2\ell_y$, we obtain to leading order in L_x and L_y :

$$-\sum_i \langle \mathbf{F}_i^w \cdot \mathbf{r}_i \rangle = - \int d^d \mathbf{r} \rho(\mathbf{r}) \mathbf{F}^w(\mathbf{r}) \cdot \mathbf{r} \quad (5.18)$$

$$= 2L_x L_y P_b \quad (5.19)$$

$$\equiv dV_d P_b, \quad (5.20)$$

where V_d is the total bulk volume and d the space dimension.

Now that we have established the equality that brings the pressure out, we come back to our Virial formula (5.1) for active fluids. For ABPs, RTPs and AOUPs, the active force reads $\mathbf{F}_i^a = (v_0/\mu) \mathbf{u}_i$ where \mathbf{u}_i is a unitary vector whose components verify the correlations:

$$\langle u_i^\alpha(t) u_j^\beta(t') \rangle = \frac{\delta_{ij} \delta_{\alpha\beta}}{d} e^{-|t-t'|/\tau}, \quad (5.21)$$

where τ defines the correlation time.

We want to compute $\langle \mathbf{u}_i \cdot \mathbf{r}_i \rangle$. In the steady state, the time derivative of $\langle \mathbf{u}_i \cdot \mathbf{r}_i \rangle$ vanishes. We get

$$\frac{d}{dt} \langle \mathbf{r}_i \cdot \mathbf{u}_i \rangle = \mu \langle \mathbf{F}_i^w \cdot \mathbf{u}_i \rangle + \mu \sum_j \langle \mathbf{F}_{ji} \cdot \mathbf{u}_i \rangle + v_0 \langle \mathbf{u}_i \cdot \mathbf{u}_i \rangle - \tau \langle \mathbf{r}_i \cdot \mathbf{u}_i \rangle \quad (5.22)$$

$$= \mu \langle \mathbf{F}_i^w \cdot \mathbf{u}_i \rangle + \mu \sum_j \langle \mathbf{F}_{ji} \cdot \mathbf{u}_i \rangle + v_0 - \tau \langle \mathbf{r}_i \cdot \mathbf{u}_i \rangle \quad (5.23)$$

$$= 0, \quad (5.24)$$

which leads to

$$\langle \mathbf{r}_i \cdot \mathbf{u}_i \rangle = \mu \tau \langle \mathbf{F}_i^w \cdot \mathbf{u}_i \rangle + \mu \tau \sum_{j \neq i} \langle \mathbf{F}_{ji} \cdot \mathbf{u}_i \rangle + v_0 \tau. \quad (5.25)$$

Using $\mathbf{F}_i^a = (v_0/\mu)\mathbf{u}_i$ and Eq. (5.25), we obtain from Eq. (5.3) the following equation

$$\begin{aligned} - \sum_i \langle \mathbf{r}_i \cdot \mathbf{F}_i^w \rangle &= dNk_B T + \sum_i \sum_{j \neq i} \langle \mathbf{r}_i \cdot \mathbf{F}_{ji} \rangle \\ &+ v_0 \tau \sum_i \langle \mathbf{F}_i^w \cdot \mathbf{u}_i \rangle + v_0 \tau \sum_i \sum_{j \neq i} \langle \mathbf{F}_{ji} \cdot \mathbf{u}_i \rangle + \frac{Nv_0^2 \tau}{\mu}. \end{aligned} \quad (5.26)$$

Finally, using the identity (5.20), the pressure for an active fluid reads

$$P_b = P^{\text{eq}} + P^a + \frac{v_0 \tau}{dV_d} \sum_i \langle \mathbf{F}_i^w \cdot \mathbf{u}_i \rangle, \quad (5.27)$$

where the equilibrium and active contributions read

$$P^{\text{eq}} = \frac{Nk_B T}{V_d} + \frac{1}{V_d d} \sum_i \sum_{j \neq i} \langle \mathbf{r}_i \cdot \mathbf{F}_{ji} \rangle, \quad (5.28)$$

$$P^a = \frac{Nv_0^2 \tau}{d\mu V_d} + \frac{v_0 \tau}{dV_d} \sum_i \sum_{j \neq i} \langle \mathbf{F}_{ji} \cdot \mathbf{u}_i \rangle, \quad (5.29)$$

respectively. Let us comment on the term $V_d^{-1} \sum_i \langle \mathbf{F}_i^w \cdot \mathbf{u}_i \rangle$ appearing in (5.27). This term scales like the number of particle adsorbed at the boundaries N_A , over the total volume V_d of the system. In [SJ16], the authors confirm that $N_A = o(N)$ in the thermodynamic limit, which means that N_A/V_d vanishes in the thermodynamic limit. This validates the fact that the pressure is a bulk state variable for a certain class of active liquids. At this stage, we can actually focus on the precise scaling of this surface term $V_d^{-1} \sum_i \langle \mathbf{F}_i^w \cdot \mathbf{u}_i \rangle$ for particles confined in a spherical cavity. Indeed, for such a system, the pressure at the wall P_w is strictly homogeneous because of the rotational invariance. In particular, for an ideal gas of active, the only correction to the bulk pressure comes from this surface

term. Equation (5.27) simplifies and the Virial computation thus exactly yields

$$P_w = \frac{Nk_B T}{V_d} + \frac{Nv_0^2 \tau}{d\mu V_d} + \frac{v_0 \tau}{dV_d} \sum_i \langle \mathbf{F}_i^w \cdot \mathbf{u}_i \rangle. \quad (5.30)$$

Using $d \times V_d = RS_{d-1}$, with R the radius of the $(d-1)$ -sphere of surface area S_{d-1} , we get

$$P_w = \frac{Nk_B T}{V_d} + \frac{Nv_0^2 \tau}{d\mu V_d} + \frac{1}{R} \left(\frac{v_0 \tau}{S_{d-1}} \sum_i \langle \mathbf{F}_i^w \cdot \mathbf{u}_i \rangle \right). \quad (5.31)$$

Since the particles at the wall point towards the wall in average, and because of the rotational invariance, $\sum_i \langle \mathbf{F}_i^w \cdot \mathbf{u}_i \rangle / S_{d-1}$ has a finite value in the thermodynamic limit. The formula (5.31) shows that the pressure of an ideal gas of active particles possesses finite size corrections, and that these corrections scale as $1/R$, which is reminiscent of the Laplace-Young formula (which we discuss further once we have defined the surface tension of an active liquid on a wall).

In the next section, we are going to see how we can extract the surface tension γ of a fluid-solid interface thanks to our modified Virial. We will also establish the link between the surface tension and the correction to the pressure for particles in a sphere.

5.2 The Virial for planar interfaces

In the previous section, we have seen behind the scenes of a Virial derivation to the equation of state. Let's see if a similar route can be found to extract surface tension. The Virial formula obviously contains subdominant contributions to the pressure (the term I_c in (5.11) for instance) that might be extracted in a computation. We see also in (5.8) that the divergence of the position vector yields exactly the good thermodynamic scaling for the pressure term. In what follows, we are going to astutely modify the starting point of our Virial computation in order to extract the sub-extensive contributions only. We will here consider a modified Virial $\mathcal{V}^* = \sum_i (\mathbf{r}_i \cdot \mathbf{r}_i^*) / 2$, where \mathbf{r}^* will be a divergenceless vector.

5.2.1 Surface tension in a rectangular box

We focus on the same two-dimensional setup as before, depicted in Fig. 5.1 and 5.2. Particles are confined by a potential $V(x, y)$ that extends from $-\ell_x - \sigma$ to $\ell_x + \sigma$ in the x direction, and from $-\ell_y - \sigma$ to $\ell_y + \sigma$ in the y direction. The particles are not subjected to the wall force in the bulk, i.e.: $V(x, y) = 0$ for $(x, y) \in [-\ell_x, \ell_x] \times [-\ell_y, \ell_y]$. We define $L_x \equiv 2\ell_x$ and $L_y \equiv 2\ell_y$ the lengths of the box. How is the fluid-solid surface tension defined for such a system? We do not consider any phase separation in the fluid here to avoid dealing with the liquid-vapor surface tension in the first place (this will be dealt with later). With this assumption in mind, we now use the classic mesoscopic approach in which the total force exerted on the planar wall has two contributions. A contribution from the pressure and a contribution from the surface tension. For instance, the total

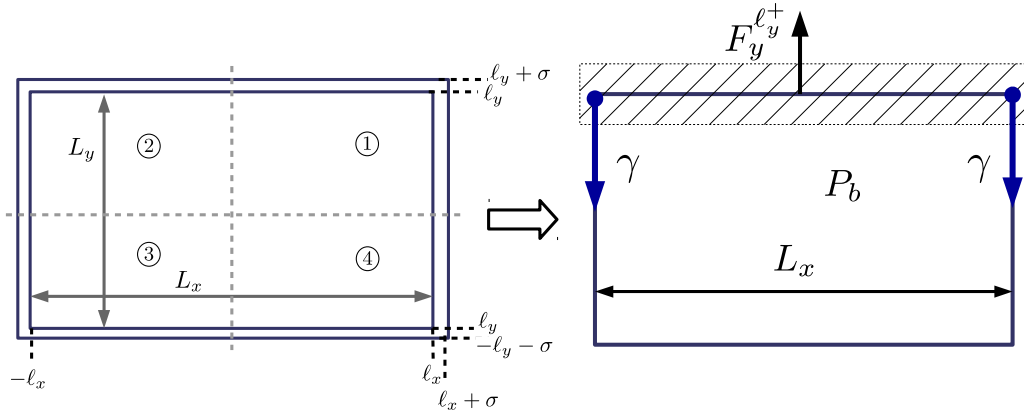


Figure 5.2 – Rectangular box that confines the active liquid. The total force on the upper wall is $F_y^{\ell_y^+} = P_b L_x - 2\gamma$.

force exerted in the y direction by the particles located at the top wall, denoted $F_y^{\ell_y^+}$, reads

$$F_y^{\ell_y^+} = \int_{-\ell_x-\sigma}^{\ell_x+\sigma} \int_{\ell_y}^{\ell_y+\sigma} dx dy \rho(x, y) \partial_y V \quad (5.32)$$

$$\equiv P_b L_x - 2\gamma, \quad (5.33)$$

with $P_b \equiv \lim_{L_x \rightarrow \infty} (F_y^{\ell_y^+} / L_x)$, and γ can thus be seen as a macroscopic definition of the fluid-solid surface tension. The factor 2 stands for the contribution of the two edges of the wall. We notice that in two dimensions, surface tension has the dimension of a force, while the pressure has the dimension of a force per unit length. In three dimensions, familiar scalings are recovered (force per unit area for the pressure and force per unit length for the surface tension).

Let us now show how defining the Virial using a divergenceless vector, we are able to get rid of the pressure while retaining the surface contribution. In this rectangular geometry, we use $\mathbf{r}_i^* = (x_i, -y_i)$. The time derivative of $\sum_i \langle \mathbf{r}_i \cdot \mathbf{r}_i^* \rangle / 2$ yields

$$0 = \sum_i \langle \mathbf{r}_i^* \cdot \frac{d\mathbf{r}_i}{dt} \rangle + 0 \quad (5.34)$$

$$= \left(\sum_i \langle \mathbf{r}_i^* \cdot \mathbf{F}_i^w \rangle + \sum_i \sum_j \langle \mathbf{r}_i^* \cdot \mathbf{F}_{ji} \rangle + \sum_i \langle \mathbf{r}_i^* \cdot \mathbf{F}_i^a \rangle \right), \quad (5.35)$$

where the translational noise correlations have cancelled each other using Itô calculus. We are now going to show that the term $\sum_i \langle \mathbf{r}_i^* \cdot \mathbf{F}_i^w \rangle$ contains the surface tension contribution we are looking for.

With the microscopic density $\rho(x, y)$, the Virial term of interest writes:

$$-\sum_i \langle \mathbf{F}_i^w \cdot \mathbf{r}_i^* \rangle = \int_{-\ell_x-\sigma}^{\ell_x+\sigma} dx \int_{-\ell_y-\sigma}^{\ell_y+\sigma} dy (x\rho(x, y)\partial_x V - y\rho(x, y)\partial_y V) \quad (5.36)$$

We define the linear force density, along the top wall for instance, located at $y = +\ell_y$:

$$f_y^{\ell_y+}(x) = \int_{\ell_y}^{\ell_y+\sigma} dy \rho(x, y) \partial_y V \quad (5.37)$$

where we recall that the wall diverges at $\ell_y + \sigma$. The total force on the top wall is given by:

$$F_y^{\ell_y+} = \int_{-\ell_x-\sigma}^{\ell_x+\sigma} dx f_y^{\ell_y+}(x) \quad (5.38)$$

We notice that the force density along x on the upper wall can actually be split as follows:

$$f_y^{\ell_y+}(x) = P_b + \delta f_y^{\ell_y+}(x), \quad (5.39)$$

where P_b is the average force density on the wall in the thermodynamic limit, and $\delta f_y^{\ell_y+}(x)$ is a correction due to a wall or an interface in the x -direction. Physically, we have $\delta f_y^{\ell_y+}(x) = 0$ when $-\ell_x + \ell \lesssim x \lesssim \ell_x - \ell$, with ℓ the typical width over which the system displays a density different from the bulk (call this phase a ‘boundary layer’). The sign of $\delta f_y^{\ell_y+}(x)$, or excess force density, depends on the particles considered. The definition of γ should be independent of the width ℓ of the boundary layer, which we do not know in advance. Hence (5.33) gives a nice definition of surface tension which does not explicitly depend on ℓ . The surface tension thus reads

$$\gamma \equiv -\frac{1}{2} \lim_{L_x \rightarrow \infty} (F_y^{\ell_y+} - L_x P_b) \quad (5.40)$$

$$= -\frac{1}{2} \lim_{\ell_x \rightarrow \infty} \int_{-\ell_x-\sigma}^{\ell_x+\sigma} dx \delta f_y^{\ell_y+}(x) \quad (5.41)$$

$$= -\lim_{\ell_x \rightarrow \infty} \int_0^{\ell_x+\sigma} dx \delta f_y^{\ell_y+}(x), \quad (5.42)$$

where we have used the symmetry of the system (left walls and right walls are identical) to go from second line to third line.

In the following, we are going to show that the modified Virial, in the hard wall limit, yields the surface tension we have defined in (5.42). Let us now focus on the force along y in the up right corner (corner ①):

$$I_{1y} = \int_0^{\ell_x+\sigma} dx \int_0^{\ell_y+\sigma} dy y \rho(x, y) \partial_y V. \quad (5.43)$$

We are going to perform a change of variable $y = \ell_y + \varepsilon$, with $\sigma/\ell_y \rightarrow 0$ in order to keep the leading order terms, and we are going to split the force density into the mean force

density P_b , plus a force density that varies along x . We have

$$I_{1y} = \int_0^{\ell_x+\sigma} dx \int_0^{\ell_y+\sigma} dy y \rho(x, y) \partial_y V \quad (5.44)$$

$$= \int_0^{\ell_x+\sigma} dx \int_{0-}^{\sigma} d\varepsilon (\ell_y + \varepsilon) \rho(x, \ell_y + \varepsilon) \partial_y V \quad (5.45)$$

$$= \left(\ell_y \int_0^{\ell_x+\sigma} dx f_y^{\ell_y+}(x) \right) + \left(\int_0^{\ell_x+\sigma} dx \int_{0-}^{\sigma} d\varepsilon \varepsilon \rho(x, \ell_y + \varepsilon) \partial_y V \right) \quad (5.46)$$

$$= \ell_y \int_0^{\ell_x+\sigma} dx P_b + \ell_y \int_0^{\ell_x+\sigma} dx \delta f_y^{\ell_y+}(x) + M \quad (5.47)$$

$$= \ell_x \ell_y P_b + \ell_y \sigma P_b + \ell_y \int_0^{\ell_x+\sigma} dx \delta f_y^{\ell_y+}(x) + M \quad (5.48)$$

with

$$|M| = \left| \int_0^{\ell_x+\sigma} dx \int_{0-}^{\sigma} d\varepsilon \varepsilon \rho(x, \ell_y + \varepsilon) \partial_y V \right| < \int_0^{\ell_x+\sigma} dx \int_{0-}^{\sigma} d\varepsilon |\varepsilon \rho(x, \ell_y + \varepsilon) \partial_y V| \quad (5.49)$$

$$< \sigma \int_0^{\ell_x+\sigma} dx |f_y^{\ell_y+}(x)| \quad (5.50)$$

$$< \sigma (P_b \ell_x + |\gamma|) \quad (5.51)$$

It is important to notice that in the hard wall limit, $\ell_y \sigma P_b \ll \ell_y \int_0^{\ell_x+\sigma} dx \delta f_y^{\ell_y+}(x) = O(\ell_y \gamma)$. Hence, defining $M'_y = (\ell_y \sigma P_b + M)$ one gets $M'_y \sim O(\sigma(\ell_x + \ell_y))$, negligible in the limit $\sigma \rightarrow 0$ (hard wall). The result is the same when computing the force along y in the up-left corner (labelled as ②). We obtain

$$I_{1y} + I_{2y} = P_b(2\ell_x)\ell_y + 2\ell_y \int_0^{\ell_x+\sigma} \delta f_y^{\ell_y+}(x) dx + 2M' \quad (5.52)$$

One notices that the force density on the y direction is odd with respect to variable x . For $x > 0$, the force density verifies $f_y^{\ell_y+}(x) = -f_y^{\ell_y-}(-x)$, with $f_y^{\ell_y-}(x)$ the force density on the wall at $y = -\ell_y$. For the bottom-left corner ③ we have by symmetry:

$$I_{3y} = \int_{-\ell_x-\sigma}^0 dx \int_{-\ell_y-\sigma}^0 dy y \rho(x, y) \partial_y V \quad (5.53)$$

$$= \ell_x \ell_y P_b + \ell_y \int_0^{\ell_x+\sigma} dx \delta f_y^{\ell_y+}(x) + M'_y \quad (5.54)$$

Thus the contributions of the down corners along y read:

$$I_{3y} + I_{4y} = P_b(2\ell_x)\ell_y + 2\ell_y \int_0^{\ell_x+\sigma} \delta f_y^{\ell_y+}(x) dx + 2M'_y \quad (5.55)$$

Finally, the total contribution along y reads

$$I_y = I_{1y} + I_{2y} + I_{3y} + I_{4y} = P_b L_x L_y + 2L_y \int_0^{\ell_x + \sigma} \delta f_y^{\ell_y +}(x) dx + 4M'_y, \quad (5.56)$$

where we have used $2\ell_x = L_x$ and $2\ell_y = L_y$. Similarly along x we have:

$$I_x = I_{1x} + I_{2x} + I_{3x} + I_{4x} = P_b L_x L_y + 2L_x \int_0^{\ell_y + \sigma} \delta f_x^{\ell_x +}(y) dy + 4M'_x. \quad (5.57)$$

Finally, combining (5.56) and (5.57) the volume terms cancel out in the modified Virial:

$$-\sum_i \langle \mathbf{F}_i^w \cdot \mathbf{r}_i^* \rangle = I_x - I_y \quad (5.58)$$

$$= 2L_x \int_0^{\ell_y + \sigma} \delta f_x^{\ell_x +}(y) dy - 2L_y \int_0^{\ell_x + \sigma} \delta f_y^{\ell_y +}(x) dx + 4M'_x - 4M'_y \quad (5.59)$$

$$= -2C^* \gamma + O(\sigma), \quad (5.60)$$

with $C^* = (L_x - L_y)$, a linear combination that depends on our definition of \mathbf{r}^* , and $\gamma = -\int_0^{\ell_y + \sigma} \delta f_x^{\ell_x +}(y) dy = -\int_0^{\ell_x + \sigma} \delta f_y^{\ell_y +}(x) dx$. Note also that $\int_0^{\ell_x + \sigma} \delta f_y^{\ell_y +}(x) dx$ is indeed a finite number when $\ell_x \rightarrow \infty$ because $\delta f_y^{\ell_y +}(x) = 0$ for $x < \ell_x - \ell$, with ℓ a small width.

We are now able to express the surface tension as a function of the microscopic correlators. Injecting (5.60) in (5.35) one gets

$$\gamma = -\frac{1}{2(L_x - L_y)} \left(\sum_i \sum_{j \neq i} \langle \mathbf{r}_i^* \cdot \mathbf{F}_{ji} \rangle + \sum_i \langle \mathbf{r}_i^* \cdot \mathbf{F}_i^a \rangle \right). \quad (5.61)$$

We can be more specific by looking at the surface tension of ABPs, RTPs or AOUPs on a hard wall. Again, the active force reads $\mathbf{F}_i^a = (v_0/\mu) \mathbf{u}_i$ with the correlations of \mathbf{u}_i given by Eq. (5.21). We now have to compute the correlator $\langle \mathbf{r}_i^* \cdot \mathbf{u}_i \rangle$. We extend the definition of the $*$ operator to any vector \mathbf{A} such that $\mathbf{A}^* = (A_x, -A_y)$. Similarly to Eq. (5.24), we take the time derivative of $\langle \mathbf{r}_i^* \cdot \mathbf{u}_i \rangle$, and we finally get:

$$\langle \mathbf{r}_i^* \cdot \mathbf{u}_i \rangle = \mu\tau \langle \mathbf{F}_i^w \cdot \mathbf{u}_i^* \rangle + \tau\mu \sum_{j \neq i} \langle \mathbf{F}_{ji} \cdot \mathbf{u}_i^* \rangle + v_0\tau \langle \mathbf{u}_i \cdot \mathbf{u}_i^* \rangle. \quad (5.62)$$

We recall that in steady state, $\langle \mathbf{u}_i \cdot \mathbf{u}_i^* \rangle = 0$ since \mathbf{u}_i is isotropic on its full history. Injecting (5.62) in (5.61), we finally obtain the surface tension of a fluid of active particles on a hard wall:

$$\gamma = -\frac{1}{2C^*} \left(\sum_i \sum_{j \neq i} \langle \mathbf{F}_{ji} \cdot \mathbf{r}_i^* \rangle + v_0\tau \sum_i \sum_{j \neq i} \langle \mathbf{F}_{ji} \cdot \mathbf{u}_i^* \rangle + v_0\tau \sum_i \langle \mathbf{F}_i^w \cdot \mathbf{u}_i^* \rangle \right). \quad (5.63)$$

While our derivation above applied to the case $d = 2$, this result can be naturally extended to higher dimensions. The coefficient C^* obviously depends on the dimension, and scales like the contact area between the fluid and the wall.

We can actually relate this result to the finite size correction we have obtained for

the pressure of an active ideal gas in a spherical cavity. Without pairwise interactions between particles in (5.63), we arrive at the expression of the surface tension of an ideal gas of active particles on a planar hard wall:

$$\gamma = -\frac{1}{2C^*} \left(v_0 \tau \sum_i \langle \mathbf{F}_i^w \cdot \mathbf{u}_i^* \rangle \right). \quad (5.64)$$

A nice property of this correlator is that it is non zero only for particles at the wall. Let us focus on the $d = 2$ case. The renormalizing factor $C^* = (L_x - L_y)$ is equivalent to L_x in the thermodynamic limit when we add the constraint $L_x/L_y \rightarrow \infty$. Thus, $2C^*$ is then nothing but the total length $2L_x$ of the fluid-solid interface (bottom wall + upper wall). One observes the same extensive scaling $\sim L_x$ for $\sum_i \langle \mathbf{F}_i^w \cdot \mathbf{u}_i^* \rangle$ which becomes equivalent to $\sum_i \langle \mathbf{F}_i^w \cdot \mathbf{u}_i \rangle$ in the $L_x/L_y \rightarrow \infty$ limit, since the contributions of the side walls are now negligible. By symmetry and with this extensive scaling in the interface length, one can isolate the surface tension γ of active particles on a single planar wall of length L :

$$\gamma = -\frac{v_0 \tau}{L} \sum_i \langle \mathbf{F}_i^w \cdot \mathbf{u}_i \rangle. \quad (5.65)$$

We are now able to identify the correction to the pressure that active particles exert on a $(d - 1)$ -sphere of radius R . Specifically, for particles in a circle, the correction to the pressure reads (see Eq. (5.31)):

$$\frac{1}{R} \frac{v_0 \tau}{2\pi R} \sum_i \langle \mathbf{F}_i^w \cdot \mathbf{u}_i \rangle = \frac{1}{R} \left(\frac{v_0 \tau}{2\pi R} \times 2\pi \lim_{\varphi \rightarrow 0} \frac{1}{\varphi} \sum_{\mathbf{r}_i \in \Omega_\varphi} \langle \mathbf{F}_i^w \cdot \mathbf{u}_i \rangle \right) \quad (5.66)$$

$$= -\frac{\gamma}{R}, \quad (5.67)$$

where we have used the rotational invariance of the correlator, Ω_φ being a circular sector of angle φ , and we have used (5.65) to obtain the surface tension of a wall of length $R\varphi$. One thus obtain $P_w = P_0 - \gamma/R$, which is indeed the Laplace-Young formula for an active gas in eq. (5.31).

5.2.2 Mesoscopic shortcut

The detailed proof of the validity of the Virial route leads us to simply describe the pressure and the surface tension as they were historically considered: the pressure as a homogeneous surface force, and the surface tension as a force localized in the corners of the system. The simplified derivation for the surface tension can be applied in $d = 2$ or $d = 3$ as shown below.

a. In dimension $d = 2$

In the limit of hard walls, the external force density along a side of the box is naturally decomposed into pressure and surface tension contributions, as depicted in Fig. 5.3. Using this decomposition, a direct evaluation shows that $\langle \sum_i \mathbf{F}_i^{\text{ext}} \cdot \mathbf{r}_i^* \rangle = \gamma L_x + \gamma(L_x - L_y) - \gamma L_y + P_b L_x L_y - P_b L_y L_x$. The pressure contribution cancels out, since \mathbf{r}^* is divergenceless,

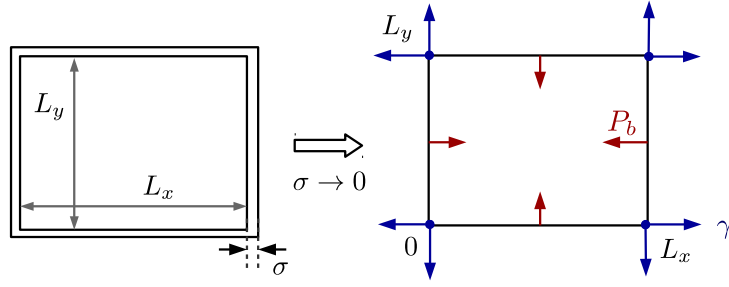


Figure 5.3 – Rectangular box that confines the active liquid in the hard-wall limit $\sigma \rightarrow 0$. In the mesoscopic description, the walls exert a homogeneous pressure P_b on the fluid, and the surface tension contribution γ is localized in the corners.

and Eq. (5.35) leads to our modified Virial for the surface tension:

$$\gamma = -\frac{1}{2(L_x - L_y)} \sum_i \left\langle \mathbf{r}_i^* \cdot \left(\frac{v_0}{\mu} \mathbf{u}_i + \sum_j \mathbf{F}_{j \rightarrow i} \right) \right\rangle. \quad (5.68)$$

Similarly, one can recover in a few steps, using the mesoscopic description, the surface tension in dimension $d = 3$.

b. In dimension $d = 3$

We consider an active fluid in a cubic box. Again, we suppose that the fluid is composed of a single phase. We adopt a mesoscopic definition of the tension γ , similarly to what we usually do for the pressure. We define $\mathcal{V} = \sum_i (\mathbf{r}_i \cdot \mathbf{r}_i^*)/2$ with $\mathbf{r} = (x, y, z)$, $\mathbf{r}^* = (\lambda_x x, \lambda_y y, \lambda_z z)$, and we take the coefficients $(\lambda_x, \lambda_y, \lambda_z) = (\frac{1}{2}, \frac{1}{2}, -1)$ to have $\nabla \cdot \mathbf{r}^* = 0$. More generally, we will consider the operator $*$ such that for any vector \mathbf{a} we have $\mathbf{a}^* = (a_x/2, a_y/2, -a_z)$. We recall the Langevin equation of motion:

$$\dot{\mathbf{r}}_i = \mu \mathbf{F}_i^w + \mu \sum_j \mathbf{F}_{ji} + \mu \mathbf{F}_i^a + \sqrt{2k_B T \mu} \boldsymbol{\xi}_i. \quad (5.69)$$

The modified Virial yields

$$0 = \sum_i \langle \mathbf{r}_i^* \cdot \mathbf{F}_i^w \rangle + \sum_i \sum_j \langle \mathbf{r}_i^* \cdot \mathbf{F}_{ji} \rangle + \sum_i \langle \mathbf{r}_i^* \cdot \mathbf{F}_i^a \rangle, \quad (5.70)$$

Using the mesoscopic definition of surface tension, we split the force exerted by a wall on the fluid in its two main contributions, namely, the pressure force exerted by the surface, and the surface tension exerted by the edges of the face. This follows the rigorous proof we have established in Section 5.2.1. The faces are indexed by k , and \mathcal{C}_k denotes the

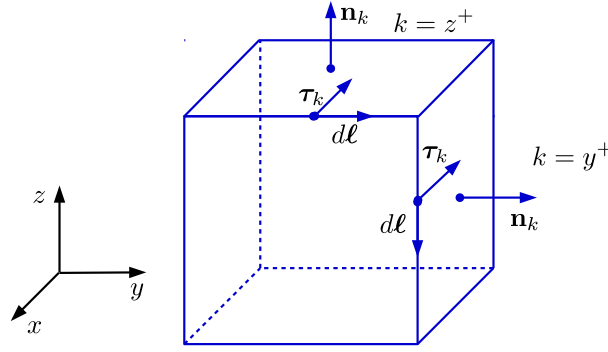


Figure 5.4 – Cubic geometry to compute the surface tension with the modified Virial.

contour of the face k , along which the fluid is submitted to the surface tension.

$$0 = \sum_i \langle \mathbf{r}_i^* \cdot \mathbf{F}_i^w \rangle + \sum_i \sum_j \langle \mathbf{r}_i^* \cdot \mathbf{F}_{ji} \rangle + \sum_i \langle \mathbf{r}_i^* \cdot \mathbf{F}_i^a \rangle \quad (5.71)$$

$$= \oint_S -P_b \mathbf{r}^* \cdot d\mathbf{S} + \sum_k \oint_{C_k} \gamma_k d\ell \boldsymbol{\tau}_k(\mathbf{r}) \cdot \mathbf{r}^* + \sum_i \sum_j \langle \mathbf{r}_i^* \cdot \mathbf{F}_{ji} \rangle + \sum_i \langle \mathbf{r}_i^* \cdot \mathbf{F}_i^a \rangle \quad (5.72)$$

$$= -P_b \iiint_V \nabla \cdot \mathbf{r}^* dV + \sum_k \gamma_k \oint_{C_k} (\mathbf{n}_k \times d\ell) \cdot \mathbf{r}^* + \sum_i \sum_j \langle \mathbf{r}_i^* \cdot \mathbf{F}_{ji} \rangle + \sum_i \langle \mathbf{r}_i^* \cdot \mathbf{F}_i^a \rangle \quad (5.73)$$

$$= \sum_k \gamma_k \oint_{C_k} (\mathbf{r}^* \times \mathbf{n}_k) \cdot d\ell + \sum_i \sum_j \langle \mathbf{r}_i^* \cdot \mathbf{F}_{ji} \rangle + \sum_i \langle \mathbf{r}_i^* \cdot \mathbf{F}_i^a \rangle \quad (5.74)$$

$$= \sum_k \gamma_k \iint_{S_k} \nabla \times (\mathbf{r}^* \times \mathbf{n}_k) \cdot \mathbf{n}_k dS_k + \sum_i \sum_j \langle \mathbf{r}_i^* \cdot \mathbf{F}_{ji} \rangle + \sum_i \langle \mathbf{r}_i^* \cdot \mathbf{F}_i^a \rangle. \quad (5.75)$$

The unit vectors $\boldsymbol{\tau}_k$ and \mathbf{n}_k which depend on the face k are such that $d\ell \times \boldsymbol{\tau}_k = d\ell \mathbf{n}_k$, see Fig. 5.4. In short, $\boldsymbol{\tau}_k$ is in the plane of face k and points toward the interior of the face, and \mathbf{n}_k is the normal of the face that points toward the exterior of the parallelepiped. Let us compute explicitly the first term in the r.h.s. for $\mathbf{n}_k = \pm \mathbf{e}_x$ and $\mathbf{n}_k = \pm \mathbf{e}_z$ for instance (\mathbf{e}_x and \mathbf{e}_y play symmetric roles). For $\mathbf{n}_k = \pm \mathbf{e}_x$, this term reads

$$\iint_{S_x^+} \nabla \times (\mathbf{r}^* \times \mathbf{e}_x) \cdot \mathbf{e}_x dz dy = \iint_{S_x^+} \nabla \times \left(-z \mathbf{e}_y - \frac{y}{2} \mathbf{e}_z \right) \cdot \mathbf{e}_x dz dy \quad (5.76)$$

$$= \iint_{S_x^+} \frac{1}{2} dz dy \quad (5.77)$$

$$= \frac{1}{2} S_x, \quad (5.78)$$

and for $\mathbf{n}_k = \mathbf{e}_z$ we have

$$\iint_{S_z^+} \nabla \times (\mathbf{r}^* \times \mathbf{e}_z) \cdot \mathbf{e}_z dx dy = \iint_{S_z^+} \nabla \times \left(\frac{y}{2} \mathbf{e}_x - \frac{x}{2} \mathbf{e}_y \right) \cdot \mathbf{e}_z dx dy \quad (5.79)$$

$$= \iint_{S_z^+} -1 dx dy \quad (5.80)$$

$$= -S_z, \quad (5.81)$$

Considering that $\gamma_k \equiv \gamma$ is the same for all the hard walls, taking into account the contribution of all the faces, one obtains

$$0 = \gamma(S_x + S_y - 2S_z) + \sum_i \sum_j \langle \mathbf{r}_i^* \cdot \mathbf{F}_{ji} \rangle + \sum_i \langle \mathbf{r}_i^* \cdot \mathbf{F}_i^a \rangle, \quad (5.82)$$

yielding the surface tension:

$$\gamma = -\frac{1}{2C^*} \left(\sum_i \sum_j \langle \mathbf{r}_i^* \cdot \mathbf{F}_{ji} \rangle + \sum_i \langle \mathbf{r}_i^* \cdot \mathbf{F}_i^a \rangle \right), \quad (5.83)$$

with $C^* = \frac{1}{2}S_x + \frac{1}{2}S_y - S_z$, a linear combination of the surface areas that depends on our definition of \mathbf{r}^* . In the rectangular box in dimension 2, we had $C^* = L_x - L_y$ when defining $\mathbf{r}^* = (x, -y)$.

Defining the surface tension as a force per unit length on a contour has paved the road for the computation of the surface tension in the case of a phase-separated system. In what follows, the system undergoes a liquid-vapor phase separation and the two phases are separated by a horizontal planar interface.

5.2.3 Virial with a phase separation

Up to now, we had consider a single-phase fluid in our parallelepiped box, such that the only surface tension we could extract was the fluid-solid surface tension. Here, we consider that the fluid undergoes a phase separation. In the confining box, we find the

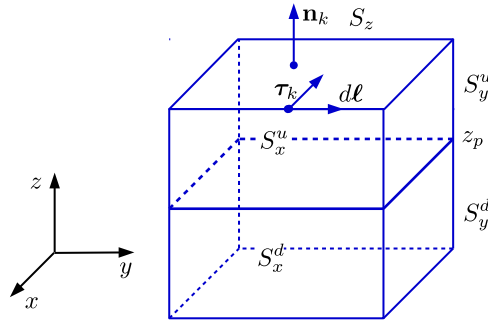


Figure 5.5 – Cubic geometry with a phase separation. The plane $z = z_p$ defines the interface between the liquid and the vapor.

vapor in mechanical equilibrium with the liquid, and we consider that the interface is parallel to the xy -plan, and located at $z = z_p$ (see Fig. 5.5). With this new interface, the system is now split into two parts. With our mesoscopic approach, we still consider that the pressure P_b is homogeneous in the system. This rests on the hypothesis that pressure is equilibrated, which is a correct hypothesis for the class of active particles we consider here. However, three different surface tensions now apply to the particles on the edges. The upper part, of side areas S_x^u and S_y^u , contains the vapor, and the particles in this part are thus subjected to the solid-vapor surface tension. We label with index k_u the different contours on which the linear force is the solid-vapor surface tension γ_{SV} . The lower part, of side areas S_x^d and S_y^d , contains the liquid, and the particles in this part are

subjected to the solid-liquid surface tension. We label with index k_d the different contours on which the linear force is the solid-liquid surface tension γ_{SL} . Finally, the contour of the liquid-vapor interface is subjected to the liquid-vapor surface tension, denoted γ_{LV} . This contour will be denoted \mathcal{C}_{z_p} . Again, we compute the time derivative of our modified Virial $\langle \mathcal{V}^* \rangle$, and we obtain (see Eq. (5.70)):

$$0 = \sum_i \langle \mathbf{r}_i^* \cdot \mathbf{F}_i^w \rangle + \sum_i \sum_j \langle \mathbf{r}_i^* \cdot \mathbf{F}_{ji} \rangle + \sum_i \langle \mathbf{r}_i^* \cdot \mathbf{F}_i^a \rangle \quad (5.84)$$

$$= \sum_{k_u} \oint_{\mathcal{C}_{k_u}} \gamma_{SV} d\ell \boldsymbol{\tau}_{k_u}(\mathbf{r}) \cdot \mathbf{r}^* + \sum_{k_d} \oint_{\mathcal{C}_{k_d}} \gamma_{SL} d\ell \boldsymbol{\tau}_{k_d}(\mathbf{r}) \cdot \mathbf{r}^* + \oint_{\mathcal{C}_{z_p}} \gamma_{LV} d\ell \boldsymbol{\tau}_{z_p}(\mathbf{r}) \cdot \mathbf{r}^* \\ + \sum_i \sum_j \langle \mathbf{r}_i^* \cdot \mathbf{F}_{ji} \rangle + \sum_i \langle \mathbf{r}_i^* \cdot \mathbf{F}_i^a \rangle \quad (5.85)$$

$$= \gamma_{SV}(S_x^u + S_y^u - S_z) + \gamma_{SL}(S_x^d + S_y^d - S_z) - \gamma_{LV} S_z \\ + \sum_i \sum_j \langle \mathbf{r}_i^* \cdot \mathbf{F}_{ji} \rangle + \sum_i \langle \mathbf{r}_i^* \cdot \mathbf{F}_i^a \rangle. \quad (5.86)$$

As previously, we have used the Stokes theorem to go from the second line to the third line.

This computation shows the principal difficulty of the Virial: since we have considered all the particles, we capture all the surface tension contributions in the same equation. In order to isolate one of the surface tension, one must take the appropriate thermodynamic scaling. For instance, imposing $S_x^u + S_y^u = S_z$ and $S_x^d + S_y^d = S_z$, it is possible to extract the liquid-vapor surface tension, even if the correlators keep a record of all the particles. In this case, the liquid-vapor surface tension reads

$$\gamma_{LV} = \frac{1}{S_z} \left(\sum_i \sum_j \langle \mathbf{r}_i^* \cdot \mathbf{F}_{ji} \rangle + \sum_i \langle \mathbf{r}_i^* \cdot \mathbf{F}_i^a \rangle \right), \quad (5.87)$$

where we recover the usual equilibrium correlator that defines the surface tension of a fluid-fluid interface when the active force is taken to 0.

In the next chapter, we are finally addressing the question of the measurement of the surface tension for an active fluid. In particular, we will relate the surface tension obtained with the Virial derivation to the surface tension measured in adapted mechanical setups implemented in computer simulations.

Chapter 6

Measuring surface tension of active fluids

In this chapter, we present practical setups that allow for direct measurements of surface tension in active fluids. These new results provide a direct physical interpretation of surface tension in active systems in terms of tangential forces. Starting from first principles, they complement existing approaches that defined surface tension from *in silico* measurement of local correlators. In practice, we first give a mechanical definition of surface tension for an active liquid on a solid boundary in Sections 6.1 and 6.2 before addressing the liquid-vapor surface tension in Section 6.3.

6.1 A delicate measurement

6.1.1 The Langmuir experiment

The setup we have presented in Section 4.3 will now prove useful to define the surface tension of active fluids on a wall. Let's define the setup that we are going to use to carry out our numerical experiments, and let's state what we are going to measure.

Our version of the Langmuir balance [Lan17] to measure the solid-gas surface tension is implemented as follows. We consider particles in a rectangular box. To confine the particles we use an external potential $V(\mathbf{r})$. In the upper region, this potential mimics two walls glued together with a smooth junction extending over a width w , see Fig. 6.1. The definition of $V(\mathbf{r})$ is the following:

$$V(\mathbf{r}) = \begin{cases} \kappa(y - L_y)^4 [\lambda_1 + \frac{\lambda_2 - \lambda_1}{2} (\tanh \frac{x-l}{w} + 1)], & \text{if } y > L_y, \\ \kappa y^4, & \text{if } y < 0, \\ \kappa(L_x - x)^4, & \text{if } x > L_x, \\ \kappa x^4, & \text{if } x < 0, \\ 0, & \text{if } 0 \leq x \leq L_x, 0 \leq y \leq L_y, \end{cases} \quad (6.1)$$

where κ , λ_1 and λ_2 fix the stiffness of the potential and l is the length of Wall 1. The different contributions on x and y add on when particles are in the corners. In short, the upper region interpolates between two repulsive potentials which, a few w 's from the junction, look like $\sim \kappa\lambda_1(y - L_y)^4$ for Wall 1, and like $\sim \kappa\lambda_2(y - L_y)^4$ for Wall 2.

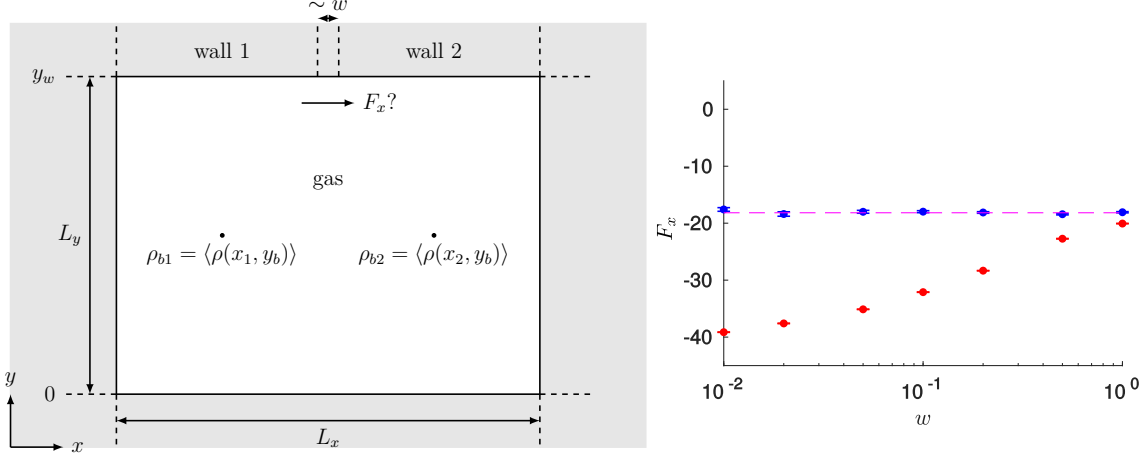


Figure 6.1 – Left: A sketch of the system setup with a single junction. **Right:** total force exerted on the wall, in the x -direction, as a function of the width w of the junction. Blue dots: passive particles. Red dots: active particles. Pink dashed line: $\Delta\gamma \equiv \gamma_2 - \gamma_1$, with γ_1 and γ_2 measured independently in a quasi-1d simulation. The value of $\Delta\gamma$ obtained from the quasi-1d simulations for active particles and the value of $\Delta\gamma$ obtained from the quasi-1d simulations for passive particles show a 0.1% discrepancy. Parameters: $v = 5$, $D_r = 1$, $\Delta t = 10^{-3}$, $t \sim 5 \times 10^8$, $N = 384$. Wall stiffness: $\lambda_1 = 10$, $\lambda_2 = 0.1$, $\kappa = 0.5$.

In Section 4.3, we have seen that our Langmuir balance could be used to measure the total force (in the direction x) F_x that particles exert on the upper wall made of two materials. This force F_x is actually the difference $\Delta\gamma \equiv \gamma_2 - \gamma_1$ of surface tensions, γ_1 (resp. γ_2) being the surface tension between Wall 1 (resp. Wall 2) and a fluid in equilibrium. In addition, the difference of surface tensions $\Delta\gamma$ does not depend on the width w of the junction between the two walls, in equilibrium.

In the following, we shall test if these properties hold for a simple active fluid, such as an ideal gas of active particles. The equation of motion of a particle i reads

$$\dot{\mathbf{r}}_i = v_0 \mathbf{u}_i - \mu \nabla_{\mathbf{r}_i} V(\mathbf{r}_i), \quad (6.2)$$

where we have neglected thermal diffusion, and where the active force on particle i enters through $(v_0/\mu)\mathbf{u}_i$, with v_0 the propulsion speed, μ the mobility and $\mathbf{u}_i \equiv (\cos \theta_i, \sin \theta_i)$ is the orientation of the active force. The wall being flat at a distance $\sim 2w$ from the junction, we identify the total force along x on the upper wall with the total force along x on the junction. This force thus simply reads

$$F_x = \int_{x_1}^{x_2} dx \int_{y_b}^{\infty} dy \rho(x, y) \partial_x V, \quad (6.3)$$

with y_b an ordinate in the bulk of the system, $x_1 = L_x/4$, $x_2 = 3L_x/4$, and $\rho(\mathbf{r}) = \langle \sum_i \delta(\mathbf{r} - \mathbf{r}_i) \rangle$ the average density of particles where brackets represent averages over

the active-force statistics. Since we do not have access to the stationary measure of the position of the active particles, we will directly measure the total force on the upper wall in a computer simulation. Such a measurement is simply the sum of the force contributions of each particle near the junction, and it reads

$$F_x = \sum_{\{i|x_1 < x_i < x_2; y_i > y_b\}} \langle \partial_x V(x_i, y_i) \rangle \quad (6.4)$$

We carry out the simulations with active Brownian particles (but again, RTPs or AOUPs would lead to identical results). The angle θ_i follows a random walk and its diffusion coefficient is denoted D_r . We measure the force F_x for different values of the junction width w . As shown in Fig. 6.1 (right, red dots), the force clearly depends on the width of the junction. In other words, the transverse force does not (only) depend on the possible intrinsic surface tensions between the gas and each of the two walls as it is the case in equilibrium (blue dots). We numerically checked that, indeed, in equilibrium, the transverse force exerted by the particles does not depend on the details of the junction. To do so, we consider an ideal gas of overdamped Langevin particles in equilibrium at temperature T . Given the parameters κ , λ_1 and λ_2 , we can actually compute the temperature T which would lead to the same transverse force as the one measured for active particles. The definition of γ for an ideal gas is given in Eq. (4.30), and reads

$$\gamma = -k_B T \rho_0 \int_{y_w}^{\infty} dy e^{-V(x,y)/T}, \quad (6.5)$$

where ρ_0 is the bulk density of particles in the thermodynamic limit, and y_w denotes the ordinate where the confining potential starts. From this, for $V_k(y) = \kappa \lambda_k (y - y_w)^4$ (with $k = 1, 2$), introducing the gamma function Γ , the difference $\Delta\gamma$ reads

$$\Delta\gamma = -\rho_0 (k_B T)^{5/4} \Gamma\left(\frac{5}{4}\right) \left(\frac{1}{(\kappa \lambda_1)^{1/4}} - \frac{1}{(\kappa \lambda_2)^{1/4}} \right). \quad (6.6)$$

In Fig. 6.1 (right), one can see that the force exerted by passive particles on the junction (blue dots) matches exactly the force predicted (pink dashed line), and does not depend on the width w of the junction.

In the following, we are going to carry out analytic computations in order to understand the origin of the dependence of the force with the details of the junction.

6.1.2 Why does the active measurement give non-trivial results?

To elucidate analytically the dependence of F_x on the width of the junction w , we start from the dynamics of N non-interacting active particles, given in Eq. (6.2). The density field $\rho(\mathbf{r}) = \langle \sum_i \delta(\mathbf{r} - \mathbf{r}_i) \rangle$ evolves according to the continuity equation

$$\partial_t \rho = -\nabla \cdot \mathbf{J}, \quad \mathbf{J} = v_0 \mathbf{m} - \rho \nabla V \quad (6.7)$$

where the local orientation field $\mathbf{m}(\mathbf{r}) = \langle \sum_i \mathbf{u}_i \delta(\mathbf{r} - \mathbf{r}_i) \rangle$ controls the contribution of the active forces to the particle flow. From the definition (6.3), using Eq. (6.7), the tangential force F_x exerted on the upper wall can be written as

$$F_x = F_D + \int_{x_1}^{x_2} \int_{y_b}^{\infty} \frac{v_0}{\mu} m_x(x, y) dx dy \quad (6.8)$$

where F_D is the total drag force experienced by particles around the junction

$$F_D = -\frac{1}{\mu} \int_{x_1}^{x_2} dx \int_{y_b}^{\infty} dy J_x = -\mu^{-1} \sum_{x_i \in [x_1, x_2]; y_i > y_b} \langle \dot{\mathbf{r}}_i \cdot \mathbf{e}_x \rangle \quad (6.9)$$

Equation (6.8) has an appealing physical interpretation in terms of force balance: the total active force exerted by the particles, which is the second term on the r.h.s. of (6.8), is split between the force exerted on the upper wall and the drag force, i.e. the force exerted on the environment. Equation (6.8) can be further simplified when expressing $\mathbf{m}(\mathbf{r})$ in steady state. Indeed, the evolution equation of the microscopic density (see, *e.g.*, [Sol+15]) reads :

$$\partial_t \hat{\psi} = -\nabla \cdot [v_0 \mathbf{u} \hat{\psi} - \mu \nabla V] + \tau^{-1} \partial_\theta^2 \hat{\psi} + \text{noise terms}, \quad (6.10)$$

where $\hat{\psi}(\mathbf{r}, \theta) = \sum_i \delta(\mathbf{r} - \mathbf{r}_i) \delta(\theta - \theta_i)$ and τ the auto-correlation time of the active force ($\tau = D_r^{-1}$ for ABPs in 2d); multiplying (6.10) by \mathbf{u} , integrating over θ and averaging over noise realizations yields the evolution of \mathbf{m} which simplifies in steady state into

$$m_\alpha = -\partial_\beta \left[v_0 \tau \left(Q_{\alpha\beta} + \frac{\rho \delta_{\alpha\beta}}{2} \right) - \mu \tau m_\alpha \partial_\beta V \right] \quad (6.11)$$

where Q measures the local nematic order through $Q_{\alpha\beta}(\mathbf{r}) = \langle \sum_i (\mathbf{u}_{i,\alpha} \mathbf{u}_{i,\beta} - \delta_{\alpha\beta}/2) \delta(\mathbf{r} - \mathbf{r}_i) \rangle$, with Greek letters referring to space directions. Eq. (6.11) holds for all models of active particles in which a local order $\mathbf{m}(\mathbf{r})$ decays exponentially in time because of the stochastic dynamics of the active force. This covers, in particular, RTPs, AOUPs, and ABPs; all simulations shown in this chapter are carried out with the latter.

Using Eq. (6.11), the isotropy of the bulk, translational invariance far from the junction, and that $\int_{y_b}^{\infty} dy Q_{xx}(x, y) = 0$ for $x = x_1$ or $x = x_2$ (shown in Appendix B.1), the force balance equation (6.8) can be rewritten as:

$$F_x = F_D - \frac{v_0^2 \tau}{2\mu} \int_{y_b}^{\infty} dy [\rho(x_2, y) - \rho(x_1, y)], \quad (6.12)$$

or equivalently,

$$F_x = F_D + \Delta\gamma \quad (6.13)$$

with $\Delta\gamma = \gamma_2 - \gamma_1$ and where we define γ_k ($k = 1, 2$) as

$$\gamma_k \equiv -\frac{v_0^2 \tau}{2\mu} \left(\int_{y_b}^{\infty} dy \rho(x_k, y) - \int_{y_b}^{y_w} dy \rho_0 \right). \quad (6.14)$$

Equations (6.13) and (6.14) form a central result of this chapter. First, Equation (6.14) can be seen as an “equation of state” for γ_k . It is determined by the excess density accumulated at the wall, compared to the bulk values in a translationally invariant system, and thus solely depends on the interaction between the active fluid and wall i . Second, the F_D contribution strongly depends on the details of the junction: the presence of an asymmetric potential combined with the nonequilibrium dynamics of the active particles generates, as in a ratchet, steady currents which are bound to be junction-dependent; the latter give rise to a non-zero drag force which contributes to the measure of F_x .

Fig. 6.2 shows independent measurements of F_x , F_D and $\Delta\gamma$ in a simulation. For the junction centered at $L_x/2$, we take $x_1 = L_x/4$ and $x_2 = 3L_x/4$ for the bulk abscissas. Also, the bulk ordinate y_b should verify $L_y - y_b \gg \ell_p$, where $\ell_p = v_0\tau$ is the persistence length of the particles. It turns out that $\sim 2\ell_p$ is the distance at which correlators have converged to their bulk values in a translationally invariant system. We thus take $y_b = L_y - 2\ell_p$. Fig. 6.2 shows that, indeed, the dependence of F_x on the width w of the junction is entirely due to the variations of F_D , whereas $\Delta\gamma$ is independent of w . All in all, the measurement F_x appears to be given by the bare $\Delta\gamma$ dressed up by F_D , which arises from the junction-dependent currents.

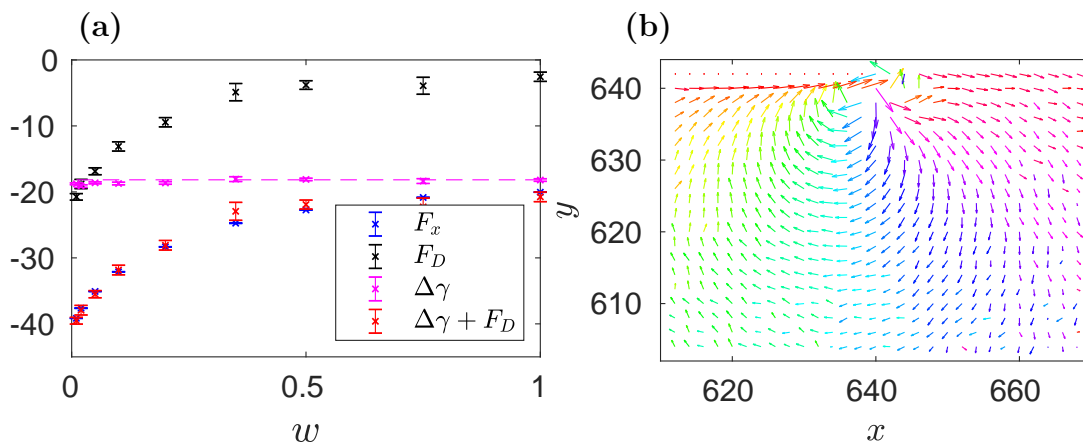


Figure 6.2 – (a) Comparison between F_x and the sum of the bare $\Delta\gamma$ and the junction-dependent drag force F_D . $\Delta\gamma$ coincides with its independent measurements using Eq. (6.14) in homogeneous systems bounded by upper potentials $V_1 = V(x \ll l)$ and $V_2 = V(x \gg l)$ (dashed line). (b) Map of the current around the junction for $|\mathbf{J}| > 10^{-6}$. The amplitude of the arrows are proportional to $\log |\mathbf{J}/10^{-6}|$; the color encodes its directions. In both figures, $\lambda_1 = 5$, $\lambda_2 = 0.05$, $l = L_x/2$, $v = 5$, $D_r = 1$, $L_x = 2L_y = 1280$. For the current field, $w = 0.01$. *Simulation results courtesy of Yongfeng Zhao.*

In the $\tau \rightarrow 0$ limit, with $D \equiv v_0^2\tau$ fixed, active particles behave as equilibrium colloids at an effective temperature $k_B T_{\text{eff}} = D/\mu$ and, indeed, Eq. (6.14) reduces to its equilibrium counterpart (6.5). The partial cancellation of the two integrals in (6.14) then stems from the fact that, unlike active particles, passive ones have a steady-state distribution which is a local function of the external potential $V(x, y)$. In this limit, as for true equilibrium systems, no currents survive in the steady state; F_D vanishes and F_x is then a direct measurement of the bare, equation-of-state-abiding contribution $\Delta\gamma$.

In what follows, we explore the variations of the current and of the density with the

distance from the center of the junction. We will see that long-range corrections to the translationally invariant system must be taken into account.

6.1.3 The dipolar field created by the junction

Figure 6.3 shows how $\Delta\gamma$ and F_D vary when the system size L_y changes for $y_b = L_y - 2\ell_p$ and for $y_b = L_y/2$, for a fixed junction width w . We normalize all quantities with the bulk density ρ_b such that when L_y increases while keeping N constant, the normalized pressure and surface tension remain identical (since they are one-body quantities for an ideal gas).

Let us comment the results. For $y_b = L_y - 2\ell_p$, as the system size increases, $\Delta\gamma$ converges to the value $\Delta\gamma_{\text{quasi-1d}} = \gamma_2 - \gamma_1$ where γ_1 and γ_2 are obtained independently, in a quasi-1d simulation (periodic boundary conditions along one direction). For $y_b = L_y/2$, as the system size increases, $\Delta\gamma$ no longer converges towards $\Delta\gamma_{\text{quasi-1d}}$, surprisingly (see Fig. 6.3, right). Instead, $\Delta\gamma$ seems to plateau, or to slightly increase. Recalling the definition of $\Delta\gamma = -v_0^2\tau/(2\mu) \int_{y_b}^{\infty} dy \Delta\rho(y)$, where $\Delta\rho(y) = \rho(x_2, y) - \rho(x_1, y)$, we have roughly, for $L_y \gg \ell_p$, $\int_{L_y/2}^{L_y} dy \Delta\rho(y) = O(1)$ which is compatible with a power-law decrease $\sim \frac{1}{y}$ of the density difference.

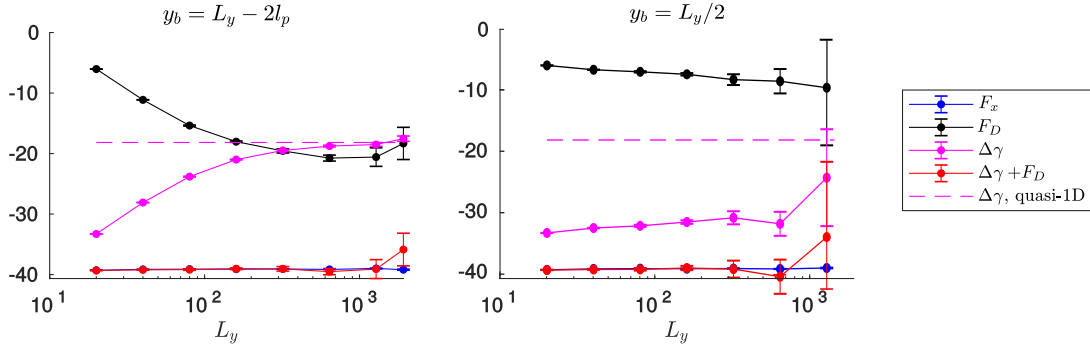


Figure 6.3 – Contributions to the total force on the junction as a function of the system size for two different y_b . **Left:** $y_b = L_y - 2\ell_p$, with $\ell_p = v_0\tau$ the run length of the particles. **Right:** $y_b = L_y/2$.

Such a scaling $\Delta\rho(r) \sim O(r^{-1})$ is actually reminiscent of the density profile that emerges around an asymmetric object embedded in a fluid of active particles. In Ref. [Bae+18], the authors show that the density profile around an asymmetric passive object centered at the origin can be cast in the following form:

$$\rho(\mathbf{r}) = \rho_b + \frac{\mu}{2\pi D} \frac{\mathbf{r} \cdot \mathbf{p}}{r^2} + O(r^{-2}). \quad (6.15)$$

The dipole moment \mathbf{p} is equal to the total force exerted by the object on the active particles:

$$\mathbf{p} = - \int d^2\mathbf{r}' \rho(\mathbf{r}') \nabla U, \quad (6.16)$$

where $U(\mathbf{r})$ is the potential created by the passive object. Similarly for the current of

active particles, we have

$$\mathbf{J}(\mathbf{r}) = -\frac{\mu}{2\pi} \left(\frac{\mathbf{p}}{r^2} - \frac{2(\mathbf{r} \cdot \mathbf{p})\mathbf{r}}{r^4} \right). \quad (6.17)$$

One can access the dipole strength with numerical simulations, and the density profile created by the junction can be compared to the one created by a artificial dipole located $(L_x/2, L_y)$ (at the junction), pointing in the x direction. The results are shown in Fig. 6.4 and display an excellent agreement between the results and the dipole ansatz. The scaling for the current $|J(r)| \sim O(r^{-2})$ has also been checked.

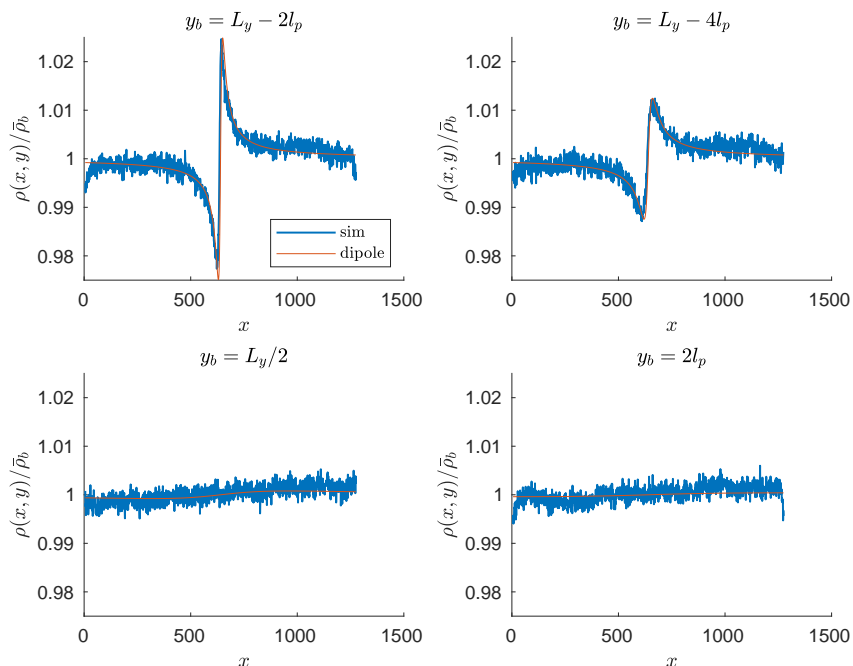


Figure 6.4 – Density profile along x at different ordinate y_b in the junction setup, compared with the theoretical prediction of a dipolar field [Bae+18]. The junction between the two walls can be assimilated with a dipole of strength $p = -38.1$ pointing in the x -direction and located at the center of the junction when fitting the model parameters on the data. The dipole strength matches the total force $F_x = 39.1$ exerted by particles on the junction. Parameters: $v_0 = 5$, $\tau = 1$, $w = 0.01$, $L_x = 1280 = 256\ell_p$, $L_y = 640 = 128\ell_p$. Wall stiffness: $\kappa = 0.5$, $\lambda_1 = 10$, $\lambda_2 = 0.1$. Time step: $\Delta t = 10^{-3}$, $t > 10^8$. Results courtesy of Yongfeng Zhao.

Let us summarize our findings. We have seen that the surface tension of an active fluid could not be directly measured by means of the Langmuir setup. The Langmuir setup nonetheless pinpoints the role of the emerging currents, specific to nonequilibrium dynamics, along with a long-range variation of the density, that are responsible for a junction-dependent measurement of the difference of surface tension. The *bare* surface tension, which depends only on the properties of the wall, could be isolated in the computation, but the question remains as to whether it is possible to directly measure this bare surface tension. The question is all the more relevant that we have seen in Section 5.2.1 that the *bare* surface tension obtained with the Virial did control the pressure correction to the bulk pressure in a circular cavity of radius R .

6.2 Accessing the bare surface tension

6.2.1 A setup where currents do not contribute

The currents arising in the Langmuir setup, which prevents the direct measurement of the bare surface tension, are due to the junction. Following [Bae+18], we expect that a more symmetric setup would reduce the strength—and thus the impact through F_D —of currents. I thus suggested considering the setup depicted in Fig. 6.5, in which the displacement of a piston allows one to access the surface tension between the fluid and the walls of the container. The normal force balance on the piston indeed writes

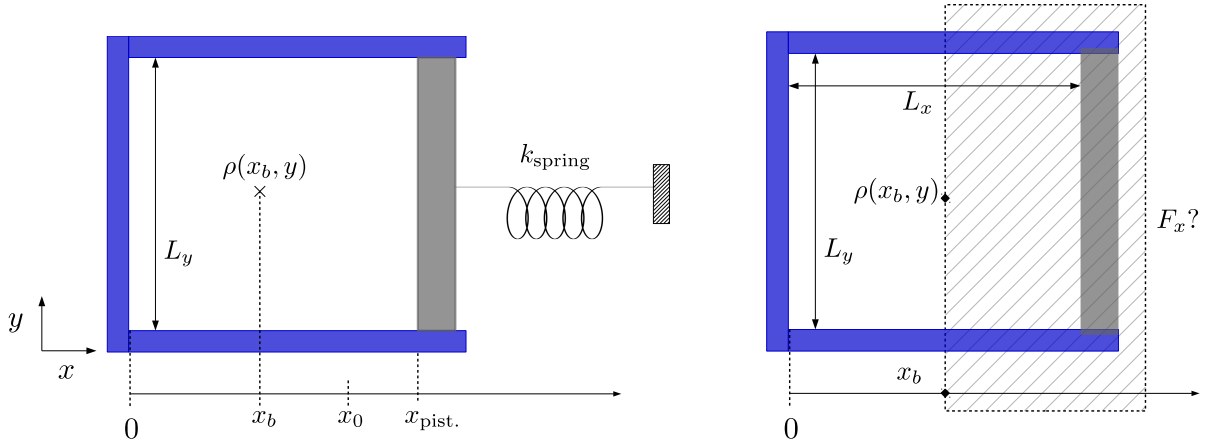


Figure 6.5 – Left: Practical setup to measure the fluid-solid surface tension between the fluid in the box and blue walls. On the grey wall, particles exert a force which is the sum of a thermodynamic pressure and a surface tension contribution of two fluid-wall interfaces. **Right:** Numerical implementation of this setup. We directly measure the total force F_x that particles exert on the grey wall.

$F_x - k_{\text{spring}}(x_{\text{pist.}} - x_0) = 0$ where $x_{\text{pist.}}$ and x_0 are the average and rest position of the piston and

$$F_x = \int_{x_b}^{\infty} \int_{-\infty}^{\infty} dx dy \rho(x, y) \partial_x V(x, y) \quad (6.18)$$

is the total force exerted by the active fluid. Let us recall how F_x can be related directly to the surface tension between the active fluid and the upper and lower walls. In the steady-state, using (6.7), F_x can be decomposed as

$$F_x = -\frac{1}{\mu} \langle \sum_{x_i > x_b} \dot{x}_i \rangle + \int_{x_b}^{\infty} \int_{-\infty}^{\infty} dx dy \frac{v_0}{\mu} m_x \quad (6.19)$$

Equation (6.11) expresses m_x as the divergence of a vector, which allows to simplify (6.19) into

$$F_x = F_D + \int_{-\infty}^{\infty} dx dy \rho(x_b, y) \frac{v_0^2 \tau}{2\mu} \quad (6.20)$$

where we have used that all fields vanish at infinity and that $\int_{-\infty}^{\infty} Q_{xx}(x_b, y) dy = 0$. We have also set $F_D = -\mu^{-1} \langle \sum_{x_i > x_b} \dot{x}_i \rangle$. Introducing the bulk pressure in thermodynamic

limit $P_b = v_0^2 \tau \rho_0 / (2\mu)$, F_x is finally given by

$$F_x = F_D + P_b L_y - 2\gamma \quad (6.21)$$

where γ is again given by Eq. (6.14), assuming for simplicity that upper and lower walls are identical.

It turns out that for this setup, $F_D = 0$. Indeed, from the continuity equation we can integrate the fields in the region $x > x_b$, which yields in steady state:

$$0 = \partial_t \int_{x_b}^{\Lambda} \int_{-\Lambda}^{\Lambda} dx dy \rho(x, y) = - \int_{x_b}^{\Lambda} \int_{-\Lambda}^{\Lambda} dx dy \nabla \cdot \mathbf{J} \quad (6.22)$$

$$= - \int_{\mathcal{C}} \mathbf{J} \cdot \hat{\mathbf{n}} ds \quad (6.23)$$

$$= \int_{-\Lambda}^{\Lambda} dy J_x(x_b, y) dy, \quad (6.24)$$

where Λ refers to a coordinate ‘far beyond the wall’ without any particle, and where we have used the divergence theorem between the first line and the second line, $\hat{\mathbf{n}}$ being the outward unitary vector normal to the displacement ds on the contour \mathcal{C} . Since we have $\int_{-\infty}^{\infty} dy J_x(x_b, y) dy = 0$, then

$$F_D = -\mu^{-1} \int_{x_b}^{\infty} \int_{-\infty}^{\infty} dy J_x(x_b, y) dy dx = 0. \quad (6.25)$$

Independent numerical measurements of F_x , F_D , P_b and γ show that the contribution of F_D is indeed null (see Fig. 6.6): the direct measurement of the bare surface tension can now be realized in practice from the displacement of the piston (see the setup Fig. 6.5). Small circulations can persist close to the corners of the setup, but their contributions to the force cancel out because of the $\int_{-\infty}^{\infty} dy J_x = 0$ constraint.

In summary, using this setup where currents do not contribute to the measurement, it is now possible to directly access the bare surface tension of a fluid-solid interface. In the hard-wall limit, this surface tension shall converge to the surface tension obtained from the Virial derivation. The next paragraph addresses this question.

6.2.2 The hard-wall limit and the Virial surface tension

In the hard-wall limit, before embarking on the simulations, one can actually guess the surface tension of an active ideal gas. Indeed, two length scales appear in the dimensional analysis, namely $\rho_0^{-1/d}$ and $v_0 \tau$, but one already has $\gamma \sim \rho_0$ since γ is a one-body quantity. The parameters left being v_0 , τ , μ , the surface tension on a hard wall simply reads

$$\gamma = c_d \rho_0 \frac{v_0^3 \tau^2}{\mu}, \quad (6.26)$$

valid for any dimension, and where c_d is a constant specific to the dimension. As expected, $\gamma = c_d \rho_0 \ell_p^2 |\mathbf{F}^a|$ scales like a force in $d = 2$ and like a linear force in $d = 3$ ($\ell_p = v_0 \tau$). In

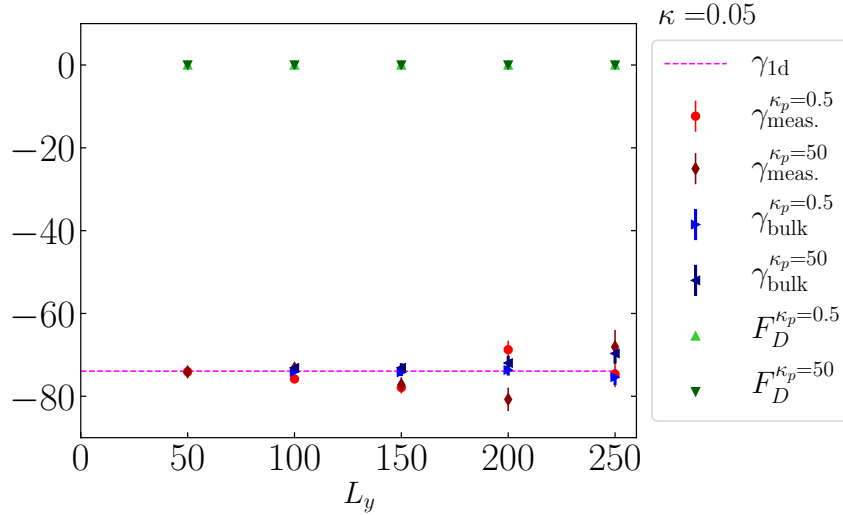


Figure 6.6 – Surface tension $\gamma_{\text{meas.}} = -(F_x - P_b L_y)/2$, bulk surface tension γ_{bulk} , bare surface tension γ_{1d} and drag force F_D , as a function of the length L_y , for two different values of the side wall stiffness κ_p . All values are renormalized by ρ_b . Parameters: $v_0 = 5$, $\tau = 1$, $N = 1024$, $\kappa = 0.05$.

the equilibrium limit where $\tau \rightarrow 0$ with $D = v_0^2 \tau$ fixed, one also recovers $\gamma_{\text{eq}} = 0$.

This prediction can be numerically checked using the Virial formula obtained in (5.63) which gives, for the surface tension of an ideal gas in a rectangular box of size $L_x \times L_y$ with $L_x \neq L_y$:

$$\gamma = -\frac{v_0 \tau}{2(L_x - L_y)} \sum_i \langle \mathbf{F}_i^w \cdot \mathbf{u}_i^* \rangle, \quad (6.27)$$

where $\mathbf{u}_i^* = (\cos \theta_i, -\sin \theta_i)$. In addition, this correlator should agree with the previous correlator (6.14) used to compute the surface tension for a wall of any shape. Figure 6.8 shows the variation of the surface tension with the speed v_0 , for active particles on a stiff wall¹. The two correlators used to compute the surface tension give the same results. The results also validate the scaling $(\gamma/\rho_b) \sim v_0^\eta$ with $\eta = 3.015 \pm 0.009$, and the scaling $(\gamma/\rho_b) \sim \tau^\nu$ with $\nu = 2.00 \pm 0.02$. The coefficient c_d has also been evaluated as $c_d = -0.40 \pm 0.02$ for ABPs and RTPs in dimension $d = 2$. To carry out the simulations on RTPs, we have used a tumble rate $\alpha = D_r = \tau^{-1}$.

The next step of this study is to implement interactions between active particles. In particular, one would like to access the liquid-vapor surface tension through the measurement of a force. The next section tackles this issue.

6.3 The liquid-vapor surface tension

We now consider active particles interacting *via* a short-range repulsive potential. When the size σ of the particles is small with respect to the persistence length $v_0 \tau$ of their active motion, the system typically undergoes a phase separation (MIPS): a liquid phase

¹In the simulations we take $V(x_p) = \kappa x_p^4$ with $\kappa = 10^4$, and x_p being the penetration distance from where the wall starts.

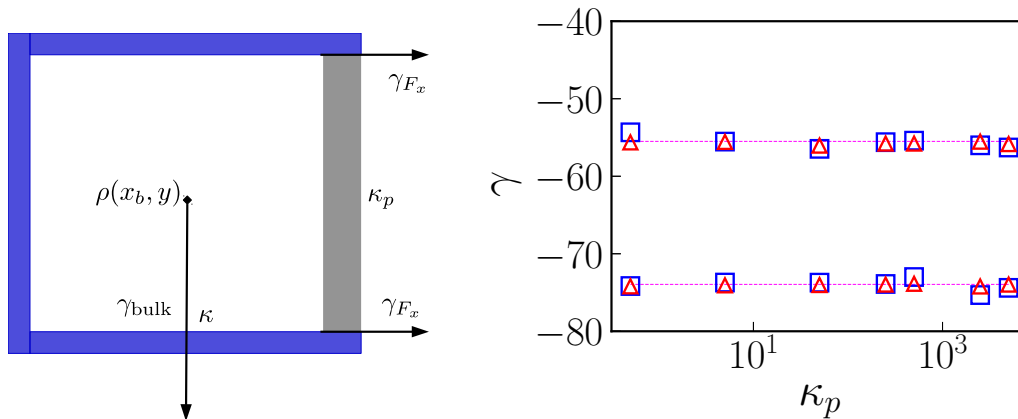


Figure 6.7 – Left: Sketch of the setup used to measure the surface tension of the blue wall. **Right:** Measurements of surface tension of the blue wall (stiffness κ) for different stiffness κ_p of the right wall. Surface tension $\gamma_{F_x} = -(F_x - P_b L_y)/(2\rho_b)$ (blue squares), and bulk surface tension $\gamma_{\text{bulk}} = (-v_0^2 \tau / (2\mu \rho_b)) (\int_{-\infty}^{y_b} \rho(x_b, y) dy - y_b \rho_b)$ (red triangles). Dashed lines: Tension measured for $\kappa = 5$ (upper results) and $\kappa = 0.05$ (lower results) for a translationally invariant system (periodic boundary conditions in one direction). Parameters: $v_0 = 5$, $\tau = 1$, $N = 1024$.

and a gaseous phase can coexist, and this behavior cannot be observed in equilibrium for purely short-range repulsive particles [FM12; Sol+18].

The surface tension of an active liquid in mechanical equilibrium with its vapor has been found negative (see Ref. [Bia+15]). While this observation is remarkable, it would probably be more accurate to say that the quantity that was measured by the authors of [Bia+15] is based on an analogy with equilibrium (using the anisotropy of the stress tensor), which leads to a formula equivalent to the Kirkwood-Buff one in equilibrium. The mechanical meaning, if any, of that quantity, was neither established nor discussed. This surface tension is negative despite the interface being stable, and it has been shown that this tension controls also the pressure discontinuity across a liquid-vapor interface of a circular drop of radius R , according to a Young-Laplace formula $\Delta P = \gamma/R$ (see Ref. [Sol+18]).

Following a similar approach to the one presented above for active fluids in contact with a solid wall, one would like to develop a mechanical setup that will allow for a direct measurement of the liquid-vapor surface tension γ_{LV} of an active fluid. A first suggestion might be to consider the previous current-free setup (see Fig. 6.5) in which the phase separation is orthogonal to the wall on which the force is measured, see Fig. 6.9. Yet, when MIPS occurs, the nucleation of the active liquid mainly takes place at the wall, thus wetting walls that become homogeneously covered with the liquid layer. Hence, it is not clear how to access the liquid-vapor surface tension with this method.

6.3.1 The Wilhelmy probe for active fluids

Since the active liquid homogeneously wets any stiffly repulsive wall, the Wilhelmy plate experiment seems to be particularly suited (see Section 4.1.2). Indeed, considering an object embedded the liquid phase, one can pull on it (with a spring for instance) and one

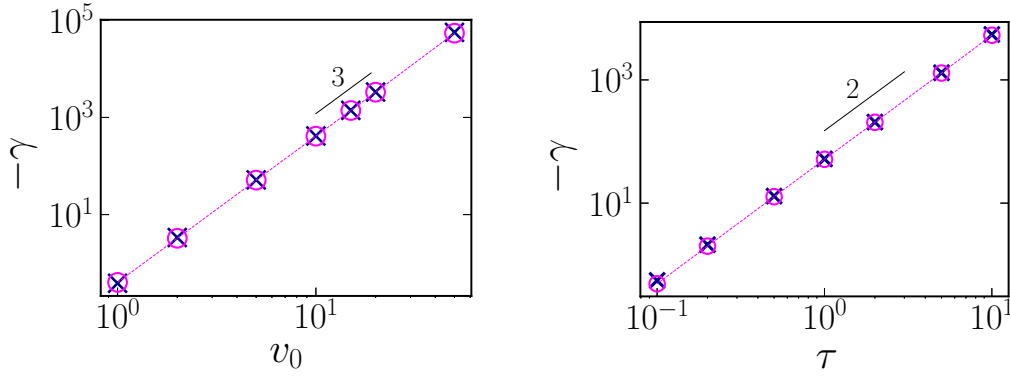


Figure 6.8 – Check of the scaling $\gamma \sim v_0^3$ (left) and $\gamma \sim \tau^2$ (right) for the surface tension of an active gas on a hard wall. Blue cross: γ using the bulk correlator (6.14). Pink circles: γ using the Virial correlator (6.27). We normalize the tension with the bulk density ρ_b . Parameters: $L_x = 2L_y = 120$, $N = 1024$, $\mu = 1$, $\kappa = 10^4$, $t \sim 5 \times 10^5$, $\Delta t = 10^{-3}$. Left: $\tau = 1$. Right: $v_0 = 5$.

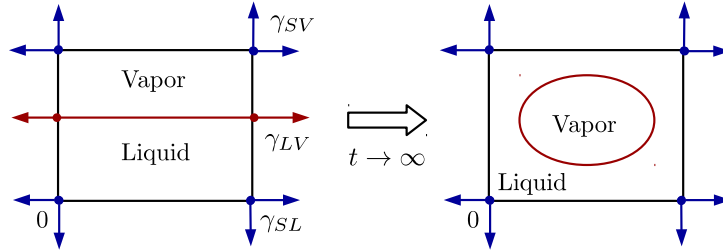


Figure 6.9 – Local forces applied on a wall in the initial state: γ_{SV} , γ_{LV} and γ_{SL} . In stationary state, one cannot extract the γ_{LV} surface tension since the active liquid completely wets the walls.

directly measures the liquid-gas surface tension when the object leaves the liquid phase. One should add that the object that plays the role of a probe must be fully symmetric, otherwise long-range currents might lead to an unwanted drag force that would dress the measurement of surface tension. Hence we choose a circular probe in dimension $d = 2$.

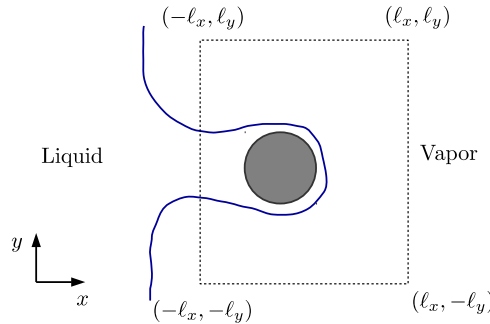


Figure 6.10 – Sketch of the setup used to access the liquid-vapor surface tension.

For interacting active particles, without thermal noise, the current \mathbf{J} in the continuity equation $\partial_t \rho = -\nabla \cdot \mathbf{J}$ takes the following form (see e.g. [Sol+18] from which we borrow

the notations):

$$\mathbf{J} = v_0 \mathbf{m} + \mathbf{I}^{(0)} - \mu \rho \nabla V(\mathbf{r}), \quad (6.28)$$

where again $\mathbf{m}(\mathbf{r})$ is the local average orientation field, $V(\mathbf{r})$ is the potential exerted by the probe, and $\mathbf{I}^{(0)}(\mathbf{r})$ is the two-body interaction field and reads

$$\mathbf{I}^{(0)}(\mathbf{r}) = - \int d\mathbf{r}' \mu \nabla U(|\mathbf{r} - \mathbf{r}'|) \langle \hat{\rho}(\mathbf{r}) \hat{\rho}(\mathbf{r}') \rangle, \quad (6.29)$$

with $\hat{\rho}(\mathbf{r}) = \sum_i \delta(\mathbf{r} - \mathbf{r}_i)$ is the instantaneous density field, and $U(\mathbf{r})$ is the two-body interaction potential. Similarly to the non-interacting case treated above, the local orientation field in the steady state can be cast as follows:

$$m_\alpha = -\tau \partial_\beta \left[v_0 (Q_{\alpha\beta} + \frac{\rho \delta_{\alpha\beta}}{2}) + I_{\alpha\beta}^{(1)} - m_\alpha \partial_\beta V \right], \quad (6.30)$$

where the correlation between the pairwise forces and the local orientation is encoded by the tensor $I_{\alpha\beta}^{(1)}$ which reads

$$I_{\alpha\beta}^{(1)} = - \int d\mathbf{r}' \mu \partial_\beta U(|\mathbf{r} - \mathbf{r}'|) \langle \hat{\rho}(\mathbf{r}') \hat{m}_\alpha(\mathbf{r}) \rangle. \quad (6.31)$$

Consequently, the total force on the probe can be computed by integrating the force density in a region $[-\ell_x, \ell_x] \times [-\ell_y, \ell_y]$ surrounding the probe, see Fig. 6.10. The total force in the direction x reads

$$F_x = \frac{1}{\mu} \int_{-\ell_x}^{\ell_x} \int_{-\ell_y}^{\ell_y} [v_0 m_x + I_x^{(0)}] dx dy + F_D, \quad (6.32)$$

where the drag force is indeed negligible in this geometry. In addition, $\mathbf{I}^{(0)}$ is also the divergence of a tensor, namely, the Irving-Kirkwood stress tensor [IK50]. We have $I_\alpha^{(0)} = \mu \partial_\beta \sigma_{\alpha\beta}^{\text{IK}}$ with

$$\sigma_{\alpha\beta}^{\text{IK}}(\mathbf{r}) = \frac{1}{2} \int d\mathbf{r}' \frac{(\mathbf{r} - \mathbf{r}')_\alpha (\mathbf{r} - \mathbf{r}')_\beta}{|\mathbf{r} - \mathbf{r}'|} \frac{dU(|\mathbf{r} - \mathbf{r}'|)}{d|\mathbf{r} - \mathbf{r}'|} \int_0^1 d\lambda \langle \hat{\rho}(\mathbf{r} + (1 - \lambda)\mathbf{r}') \hat{\rho}(\mathbf{r} - \lambda\mathbf{r}') \rangle. \quad (6.33)$$

The integration of eq. (6.32) yields

$$\begin{aligned} F_x = & \int_{-\ell_y}^{\ell_y} \left[-\frac{v_0 \tau}{\mu} \left(v_0 (Q_{xx} + \frac{\rho}{2}) + I_{xx}^{(1)} - m_x \partial_x V \right) + \sigma_{xx}^{\text{IK}} \right]_{-\ell_x}^{\ell_x} dy \\ & + \int_{-\ell_x}^{\ell_x} \left[-\frac{v_0 \tau}{\mu} \left(v_0 (Q_{xy} + I_{xy}^{(1)} - m_x \partial_y V) + \sigma_{xy}^{\text{IK}} \right) \right]_{-\ell_y}^{\ell_y} dx. \end{aligned} \quad (6.34)$$

The second integral in the r.h.s. of (6.34) vanishes since the vapor is isotropic along the horizontal lines (from $-\ell_x$ to ℓ_x) at ordinate $-\ell_y$ and ℓ_y . Moreover, the term $m_x \partial_x V$ only

contributes at the surface of the probe and can thus be discarded in the first integral. Finally, since the system is homogeneous along the y -axis at $x = \ell_x$, the total force along F_x simplifies into

$$F_x = \int_{-\ell_y}^{\ell_y} dy [\bar{\sigma}_{xx} - \sigma_{xx}(-\ell_x, y)], \quad (6.35)$$

where σ_{xx} is the sum of an active tensor and the Irving-Kirkwood stress tensor and it reads

$$\sigma_{xx} = \frac{v_0 \tau}{\mu} \left(v_0 (Q_{xx} + \frac{\rho}{2}) + I_{xx}^{(1)} \right) + \sigma_{xx}^{\text{IK}}, \quad (6.36)$$

and $\bar{\sigma}_{xx} = \sigma_{xx}(\ell_x, y)$ is constant in the bulk of the liquid and in the bulk of the vapor phase and it is given by

$$\bar{\sigma}_{xx} = \frac{v_0 \tau}{\mu} \left(v_0 \frac{\rho}{2} + I_{xx}^{(1)} \right) + \sigma_{xx}^{\text{IK}}, \quad (6.37)$$

since there is no nematic order in the bulk of either phase.

What is the connection, if any, between this force F_x and surface tension? Well, first, when the capillary bridge has a constant width and no curvature (which is the case for soap bubbles for instance), then the force on the object can be identified with the two contributions of surface tension that the bulk fluid A exerts on the fluid B that is wetting the probe, see Fig. 6.11 (left). In that case, since the bridge is flat, there are no contributions from the Laplace pressure to the total force. A second situation is when the bridge of width ϵ is infinitely thin and, though there is a contribution to the force F_x from the Laplace pressure ΔP , the pressure force scales like $\Delta P \epsilon \ll \gamma$ as already described in Section 4.1.2. In these two cases where the liquid-vapor interfaces are parallel to the x -axis, formula (6.35) has obviously the same physical content as that of the Kirkwood-Buff expression of the surface tension (4.13) written in Chapter 4. Indeed, $\bar{\sigma}_{\alpha\beta}$ being a bulk tensor, it is also isotropic thus $\bar{\sigma}_{xx} = \bar{\sigma}_{yy}$. Equation (6.35) then becomes

$$F_x = \int_{-\ell_y}^{\ell_y} dy [\bar{\sigma}_{yy} - \sigma_{xx}(-\ell_x, y)] \quad (6.38)$$

$$= -2\gamma_{LV}, \quad (6.39)$$

which is our mechanical definition of the liquid-vapor surface tension.

The computation validates the fact that the liquid-vapor surface tension can indeed be measured by means of a Wilhelmy probe. We now turn to the results of the computer simulations.

6.3.2 Simulation results

We consider an active fluid that undergoes a motility induced phase separation. We implement the dynamics of active Brownian particles of unit radius, interacting *via* a short-range repulsive pairwise harmonic potential $U(r) = 50(1 - r^2)\Theta(1 - r)$ where r is

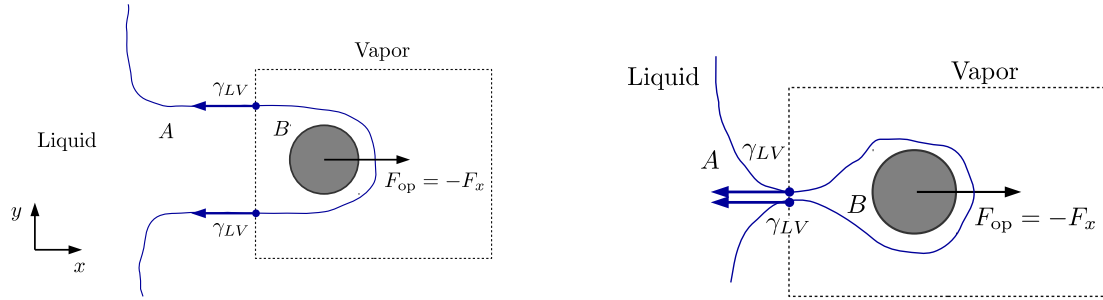


Figure 6.11 – Two cases where the force on the probe obviously reads $F_x = -2\gamma_{LV}$. The operator has to apply a force F_{op} on the object to maintain its position.

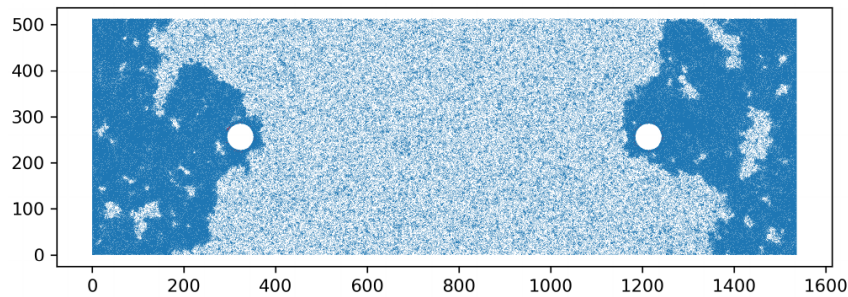


Figure 6.12 – Snapshot of the two Wilhelmy probes (white circles) dipped in an active liquid of active Brownian particles (dark blue). The light blue region is the vapor. The fluid is confined by two vertical stiff walls located at $x = 0$ and $x = 1536$. We take periodic boundary conditions in the y -direction. Parameters: $v_0 = 5$, $\tau = 5$, $L_y = 512$, $L_x = 1536$.

the distance between the centers of the particles and Θ is the Heaviside step function. The speed of the particles is $v_0 = 5$ and the rotational diffusion constant is $D_r = 0.2$, yielding a persistence length $\ell_p = 25$. Thermal noise is not included in the dynamics. The fluid is bounded in the x -direction by two stiff walls, which interact with the particles with a Weeks-Chandler-Andersen potential $V(z)$ that reads

$$V(z) = 4\epsilon \left(\frac{\sigma^{12}}{z^{12}} - \frac{\sigma^6}{z^6} \right) + \epsilon, \quad (6.40)$$

with $\sigma = 5/2^{1/6}$ and $\epsilon = 10^{-4}$, and where z is the penetration length of a particle into the wall. We take periodic boundary conditions along the y -axis. For symmetry reasons, two circular objects of radius 32 are placed at the interface between the liquid and the vapor (white circles in Fig. 6.12, and their distance from the interface is gradually increased. The circular probes interact with the particles also *via* the WCA potential. Measuring the total force on the object will lead to a mechanical evaluation of the liquid-vapor surface tension. The numerical simulations were implemented by Yongfeng Zhao.

In order to reduce fluctuations and to improve our precision, we fix the position of the probes 20σ away from the planar interface. A capillary bridge is created by the active liquid, and we measure directly the force on the x -direction and the force on the y -direction. The average density profile can be obtained from the simulations, and the position of the interface is given by the mid-density curve. From the geometry and the

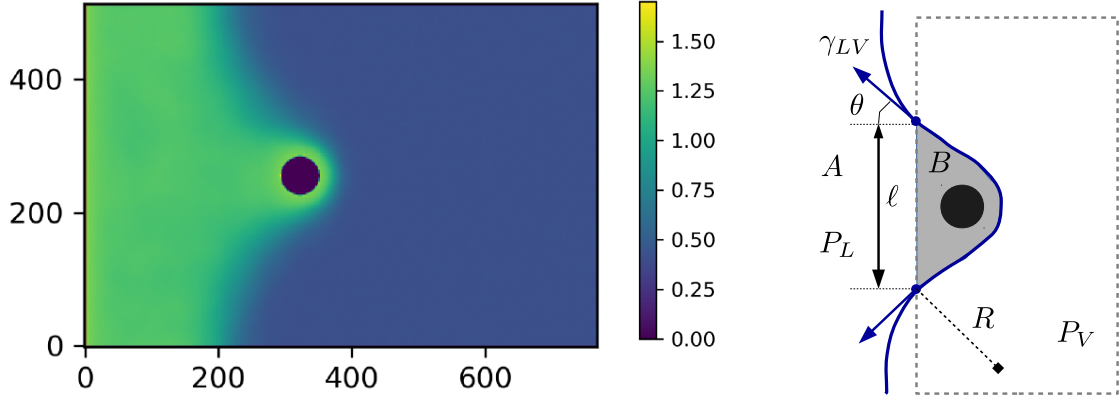


Figure 6.13 – **Left:** Zoom on the left-probe region: density profile of the fluid of interacting ABPs. We do observe an average steady interface between the liquid and the vapor. **Right:** schema of the mesoscopic forces that the fluid in domain A and the vapor exert on the fluid B . Since the fluid B is in mechanical equilibrium, then $F_{A \rightarrow B} + F_{\text{probe} \rightarrow B} = 0$, but we also have $F_{\text{probe} \rightarrow B} = -F_x$ by Newton's third law. Thus $F_x = F_{A \rightarrow B}$.

force F_x , γ can be inferred. The force balance on the fluid region B (see 6.13) reads

$$0 = (P_L - P_V)\ell - 2\gamma_{LV} \cos \theta - F_x, \quad (6.41)$$

where P_L , P_V , ℓ and θ are defined in Fig. 6.13. Using the Laplace-Young formula for active liquids [Sol+18] yields the pressure difference $P_V - P_L = \gamma/R$, where R is the radius of curvature at the interface (see Fig. 6.13). The force on the object then reads

$$F_x = -\gamma_{LV} \left(\frac{\ell}{R} + 2 \cos \theta \right). \quad (6.42)$$

From 56 independent numerical simulations, we obtain the average force along the x -axis, along with the force F_y on the y -direction. As expected, the average force along y is zero since the system possesses a symmetry axis that joins the two centers of the probes. A geometry analysis yields

$$\ell = 217 \pm 5, \quad (6.43)$$

$$R = 278 \pm 10, \quad (6.44)$$

$$\cos \theta = 0.64 \pm 0.03, \quad (6.45)$$

while the measurement on F_x yields

$$F_x = 10.3 \pm 0.6. \quad (6.46)$$

Finally, using (6.42), we obtain

$$\gamma_{LV} = -4.9 \pm 0.2. \quad (6.47)$$

The surface tension γ_{LV} is indeed negative, as previously computed with the Kirkwood-Buff formula in [Bia+15]. In our simulation, the same value for γ_{LV} is also recovered

when using the Kirkwood-Buff formula on the quasi-planar liquid-vapor interface, far from the probe. From the Kirkwood-Buff correlator, we find $\gamma_{LV}^{\text{KB}} = -4.80 \pm 0.01$, (5% error with the direct force measurement) thus showing the consistency of the Wilhelmy probe measurement.

This result is interesting in the sense that it eventually agrees with the equilibrium intuition one could gather on the liquid-vapor surface tension. Though the active liquid completely wets the probe, the latter is expelled from the liquid (the force F_x is positive). An operator has to exert a negative force (the operator must push the object towards the liquid) to maintain the object close to the interface. For phase separation in equilibrium, the force F_x is negative and one has to pull to remove the object from the liquid; this pulling force reflects the fact that the surface tension γ_{LV} is positive.

To summarize, in this Chapter, we have shown that, as in equilibrium, surface tension can be defined in active fluids by considering the tangential forces exerted on an interface. Focusing first on a solid-fluid interface, we have seen that any anisotropy of the boundary is expected to lead to steady currents that contribute to the force balance. We nevertheless identified a bare, equation-of-state abiding contribution to surface tension, which was shown to share properties with its equilibrium counterpart. The success of the mechanical measurement of the surface tension of a solid-fluid interface has led us to consider another mechanical measurement, the liquid-vapor surface tension of an active fluid, inspired by the Wilhelmy plate experiment. The force on the probe embedded in the fluid, close to the interface, shows that the probe is expelled from the liquid, in agreement with our equilibrium intuition on the liquid-vapor surface tension if the surface tension is negative. Elucidating the mechanical implications of the surface tension of active fluids paves the road to comprehension of surface wetting by active fluids, and may give insights to study interfaces between active liquids made of different particle species [Ste+15; WWF16]. Our results apply to spherical active particles interacting *via* pairwise forces, but it should be very interesting to extend the mechanical approach we have followed, for other class of active particles such as quorum-sensing active particles [Fil+17], torque-interacting active particles [CGS15], etc.

Conclusion

This thesis has focused on two families of systems pertaining to the active branch of the soft matter realm.

The first part of this thesis was devoted to the properties of a system of particles whose interactions are mediated by a fluctuating background, and whose active nature arises from a non-thermal source of noise. The combination of mediated interactions and of the nonequilibrium drive was shown to lead to complex structures. Our predictions, beyond statistical mechanical methods, rest on extending the methods of nonlinear dynamics in pattern forming systems, to systems with a local conservation law. The original biophysical context behind our model is that of transmembrane proteins with chemically driven changes of conformation. The model we have coined was design to filter out what we believed to be the key ingredients of their physics. Many other soft matter systems match the coarse description of our model, while they may belong to areas remote from biophysics. Future research directions should be focused on narrowing the gap between the model and the more realistic description of, say, transmembrane proteins, etc. This requires to critically examine the statics and dynamics of the fluctuating background field, the nature of the nonequilibrium drive, and the specifics of the coupling of the particles to the background. This thesis also presents a system of particles with mediated interactions – albeit in equilibrium – that directly connects to experimental observations. The methods of statistical mechanics have allowed us to predict the details of the interactions between two colloids embedded in a lamellar phase.

The second part emphasizes the notion of surface tension for interfaces involving active fluids. We have come up with a definition relating macroscopic forces to microscopic ones, either between particles or, when applicable, between particles and a confining medium. When the active fluid is in contact with a solid boundary, the solid-fluid surface tension is, in general, a more complex quantity than its equilibrium counterpart. By this we mean that its value may depend on the geometry or other details of the measuring device. We have also shown that a carefully designed probe allows us to access an equation-of-state-abiding surface tension akin to its equilibrium counterpart. In active fluids, geometry controls local steady currents that play a role in the value of surface tension. Liquid-vapor interfaces can also be encountered in assemblies of self-propelled particles when these undergo a motility-induced phase separation. Our mechanical definition at the macroscopic level has led us to suggest an adapted Wilhelmy plate experiment able to extract a value of surface tension which also agrees with its microscopic definition (the

latter matches a previously postulated expression). After understanding the physics of a solid-fluid or of a solid vapor interface, the next obvious, yet ambitious, step is to develop a full theory of wetting and capillarity in active fluids.

Appendix A

Details on experiments of colloids in lamellar phases

A.1 Monte Carlo simulations

To determine the predictions of our model when applied to many particles dispersed in the lamellar phase, and to compute structure factors that can be compared to experimental measurements, we perform a Monte Carlo simulation. We model the membrane-mediated interaction between the colloidal particles by means of the interaction that we have previously computed, which takes into account the presence of the lamellae and the fluctuations of both the membrane and the particles in the normal z -direction. Note that the in-plane fluctuations of the particles are implemented in the Monte Carlo algorithm. Specifically, we model the colloidal particle-lamellar phase system as a finite number M of stacks of identical colloidal particles orthogonal to z -direction, each one consisting of the same finite number N of particles confined in a disk of radius R_d . We suppose that the particles cannot change stack. We also neglect the possibility of the particles to promote defects in the lamellar phase. This is natural since we do not explicitly model the layers and also reasonable in surfactant phases owing to the weak strength of the interactions (smaller than $k_B T$). To simplify, we consider only the pairwise interactions calculated above (i.e., we neglect multibody effects) and we take into account only the contributions coming from particles in the same layer and one layer apart. Indeed, as we saw in Section 3.3, the interaction decreases rapidly with the layer separation. Moreover, since the interactions are short-ranged, we do not impose periodic boundary conditions within each layer, but we do use periodic boundary conditions in the z -direction, such that a small number ($\simeq 7$) of layers is enough for simulating an infinite system.

We start the simulation by placing the same number N of particles in each one of the M layers according to a random uniform distribution respecting a given hard-core minimum distance a_0 . We then pick at random one particle and we move it randomly inside a circle of radius ϵ . We compute the associated variation of the interaction energy and we accept the movement according to the Metropolis rule, taking into account the hard-core

constraint. The radius ϵ is adjusted in order to have an acceptance ratio of $\simeq 50\%$. The interaction energy between two colloidal particles is computed according to eqn (3.26) [resp. (3.40)] for the membrane-binding (resp. membrane-excluding) case, where the correlation functions $G_0(R)$ and $G_1(R)$ [see eqn (3.12)] can be expressed analytically in terms of modified Bessel functions (as shown in [Zak+19]).

After equilibration, we characterize the statistical order of the colloidal particles by means of the structure factor [Yan+99; Con10]:

$$\begin{aligned} S(\mathbf{q}, Q) &= \frac{1}{MN} \left\langle \left| \sum_{j,p} \exp[i(\mathbf{q} \cdot \mathbf{R}_{jp} + pQd)] \right|^2 \right\rangle, \\ &= S_0(\mathbf{q}) + 2 \sum_{n=1}^{\infty} S_n(\mathbf{q}) \cos(nQd), \end{aligned} \quad (\text{A.1})$$

where \mathbf{R}_{jp} is the position of the j -th particle of the p -th layer and \mathbf{q} (resp. Q) is the component of the wavevector parallel (resp. perpendicular) to the lipid layers. The structure factor is proportional to the Fourier transform of the two-particle correlation function. Note that in eqn (A.1) we neglect the fluctuations of the colloidal particles in the z -direction. The partial structure factors $S_n(\mathbf{q})$ describe the correlations between particles n layers apart.

For a liquid-like order, the structure factors do not depend on the orientation of the \mathbf{q} vector and thus coincide with their average with respect to the orientation of \mathbf{q} :

$$S_n(q) = \frac{1}{MN} \left\langle \sum_{i,j=0}^{N-1} \sum_{p=0}^{M-1} J_0(q |\mathbf{R}_{ip} - \mathbf{R}_{j(p+n)}|) \right\rangle, \quad (\text{A.2})$$

where q is the modulus of \mathbf{q} and because of the periodic boundary conditions in the direction perpendicular to the layers, layers p and $p + M$ coincide.

A.2 Joint validation of the Monte Carlo simulations and the Percus-Yevicz approximation

In the literature, the structure factors of pairwise interacting particles are often calculated in the framework of the Ornstein-Zernicke relation with the approximate Percus-Yevick closure, using the numerical method introduced by Lado [Lad67; Lad68]. Mapping our multilayer problem to a multicomponent fluid, as done in ref. [Con10], we have computed the equatorial structure factor $S(q) = S_0(q) + 2S_1(q)$ that can be measured by small-angle X-ray scattering with a scattering vector contained in the plane of the layers. At small concentrations, we find that the Percus-Yevick approximation is reasonably good (see Fig. A.1). However, at higher concentrations for our system the Lado algorithm does not converge in general.

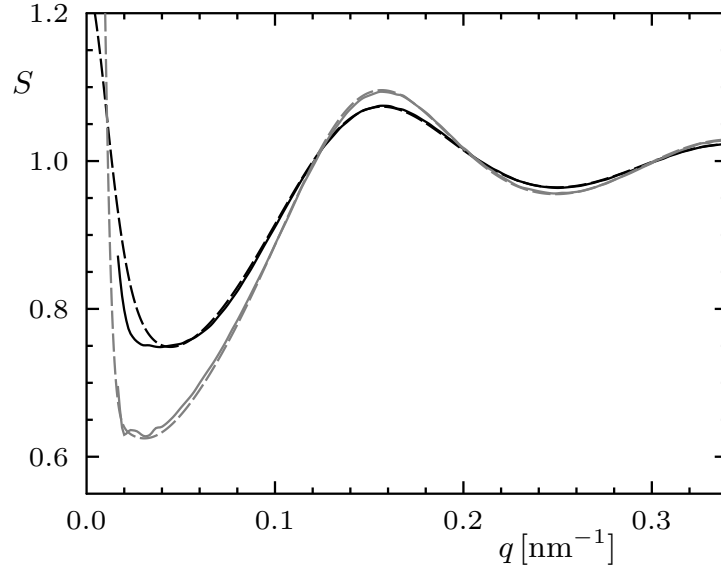


Figure A.1 – Comparison of the equatorial structure factor $S(q) = S_0(q) + 2S_1(q)$, as a function of the in-plane wavevector q , computed with a Monte Carlo simulation (full lines) and the Percus-Yevick approximation (dashed lines). The black (resp. gray) curves correspond to the membrane-binding (resp. membrane-excluding) case. The parameters are the same as in Figs. 3.7 and 3.8.

Appendix B

Details on the surface tension for active fluids

B.1 Vanishing nematic tensor

The computation of the force on the junction exerted along \mathbf{e}_x leads us to integrate the nematic tensor from the bulk to a point ‘deep in the wall’. In particular we can prove that $\int_{y_b}^{\infty} dy Q_{xx}(x_b, y) = 0$ for a translationally invariant system in the direction \mathbf{e}_x . By definition, we have

$$Q_{xx}(\mathbf{r}) = \langle \hat{Q}_{xx}(\mathbf{r}) \rangle \quad (\text{B.1})$$

$$= \langle \sum_i \left(\cos^2 \theta_i - \frac{1}{2} \right) \delta(\mathbf{r} - \mathbf{r}_i) \rangle \quad (\text{B.2})$$

$$= \langle \sum_i \cos(2\theta_i) \delta(\mathbf{r} - \mathbf{r}_i) \rangle \quad (\text{B.3})$$

For active Brownian particles where the angle evolves according to

$$\dot{\theta}_i = \sqrt{2D_r} \xi_i, \quad (\text{B.4})$$

with ξ_i a zero mean, unit variance, Gaussian white noise, using Itô calculus, we have

$$\dot{Q}_{xx} = -4D_r Q_{xx} - \partial_y \langle \sum_i \cos(2\theta_i) \dot{y}_i \delta(\mathbf{r} - \mathbf{r}_i) \rangle - \partial_x \langle \sum_i \cos(2\theta_i) \dot{x}_i \delta(\mathbf{r} - \mathbf{r}_i) \rangle. \quad (\text{B.5})$$

The derivative along x vanishes for a translationally invariant system, and in steady state we have:

$$Q_{xx} = -\frac{1}{4D_r} \partial_y \langle \sum_i \cos(2\theta_i) \dot{y}_i \delta(\mathbf{r} - \mathbf{r}_i) \rangle, \quad (\text{B.6})$$

which yields, after integration along y ,

$$\int_{y_b}^{\infty} dy Q_{xx} = \frac{1}{4D_r} \langle \sum_i \cos(2\theta_i) v_0 \sin \theta_i \delta(y_b - y_i) \delta(x - x_i) \rangle. \quad (\text{B.7})$$

Since the bulk is isotropic in steady state, one finally gets

$$\int_{y_b}^{\infty} dy Q_{xx} = 0. \quad (\text{B.8})$$

B.2 Measurements in the computer simulations

In the computer simulation, the correlators are renormalized by the bulk density ρ_b to avoid increasing the number of particles when increasing the system size while keeping a constant density. Since the pressure and the surface tension are one-body quantities for an ideal gas, normalizing by ρ_b yields conveniently a constant pressure and a constant solid-gas surface tension when L_y increases. In the quasi-1d simulations, γ is thus computed as follows

$$\gamma = -\frac{v_0^2 \tau}{2\mu \rho_b} \left(\int_{y_b}^{\infty} dy \rho(x_b, y) - \int_{y_b}^{y_w} dy \rho_b \right), \quad (\text{B.9})$$

with $\rho_b = \rho(x_b, y_b)$. From these independent measurement of γ , we deduce $\Delta\gamma_{\text{quasi-1d}}$. For the 2d-junction setup, $\Delta\gamma$ is directly obtained from the integrated the density difference:

$$\Delta\gamma = -\frac{v_0^2 \tau}{2\mu \bar{\rho}_b} \int_{y_b}^{\infty} dy [\rho(x_2, y) - \rho(x_1, y)], \quad (\text{B.10})$$

where $\bar{\rho}_b = (\rho(x_1, y_b) + \rho(x_2, y_b))/2$.

Publications

All the publications can be found on my personal webpage <https://rzakine.github.io>

P1. R. Zakine, A. P. Solon, T. Gingrich, F. van Wijland, *Stochastic Stirling engine operating in contact with active baths*, Entropy **19**, 193 (2017).

P2. R. Zakine, J.-B. Fournier, F. van Wijland, *Field-Embedded Particles Driven by Active Flips*, Phys. Rev. Lett. **121**, 028001 (2018)

P3. R. Zakine, D. de Silva Edirimuni, D. Constantin, P. Galatola and J.-B. Fournier, *Interaction and structuration of membrane-binding and membrane-excluding colloidal particles in lamellar phases*, Soft Matter, **15**, 4351-4362 (2019)

Recently submitted:

- R. Zakine, Y. Zhao, M. Knežević, A. Daerr, Y. Kafri, J. Tailleur, and F. van Wijland, *Surface Tensions between Active Fluids and Solid Interfaces: bare vs dressed*
- R. Zakine, J.-B. Fournier, F. van Wijland, *Spatial Organization of Active Particles with field mediated interactions*

Publication not related to this thesis:

- R. Zakine, M. Lemoine, *The elusive synchrotron precursor of collisionless shocks*, Astronomy & Astrophysics **601** (2017)

Bibliography

- [APP91] A. Ajdari, L. Peliti, and J. Prost. “Fluctuation-induced long-range forces in liquid crystals”. *Phys. Rev. Lett.* 66 (11 Mar. 1991), pp. 1481–1484. DOI: [10.1103/PhysRevLett.66.1481](https://doi.org/10.1103/PhysRevLett.66.1481).
- [AS20] B. Andreotti and J. H. Snoeijer. “Statics and Dynamics of Soft Wetting”. en. *Annual Review of Fluid Mechanics* 52.1 (Jan. 2020), pages. DOI: [10.1146/annurev-fluid-010719-060147](https://doi.org/10.1146/annurev-fluid-010719-060147).
- [Bae+18] Y. Baek, A. P. Solon, X. Xu, N. Nikola, and Y. Kafri. “Generic Long-Range Interactions Between Passive Bodies in an Active Fluid”. *Phys. Rev. Lett.* 120 (5 Jan. 2018), p. 058002. DOI: [10.1103/PhysRevLett.120.058002](https://doi.org/10.1103/PhysRevLett.120.058002).
- [Bén+08] K. Béneut, D. Constantin, P. Davidson, A. Dessombz, and C. Chanéac. “Magnetic Nanorods Confined in a Lamellar Lyotropic Phase”. en. *Langmuir* 24.15 (Aug. 2008), pp. 8205–8209. DOI: [10.1021/la800387a](https://doi.org/10.1021/la800387a).
- [Ber71] M. V. Berry. “The molecular mechanism of surface tension”. *Physics Education* 6.2 (1971), p. 79. DOI: [10.1088/0031-9120/6/2/001](https://doi.org/10.1088/0031-9120/6/2/001).
- [BET16] M. A. Boles, M. Engel, and Talapin. “Self-Assembly of Colloidal Nanocrystals: From Intricate Structures to Functional Materials”. *Chemical Reviews* 116.18 (2016), pp. 11220–11289. DOI: [10.1021/acs.chemrev.6b00196](https://doi.org/10.1021/acs.chemrev.6b00196).
- [BG70] F. Brochard and P. de Gennes. “Theory of magnetic suspensions in liquid crystals”. en. *Journal de Physique* 31.7 (1970), pp. 691–708. DOI: [10.1051/jphys:01970003107069100](https://doi.org/10.1051/jphys:01970003107069100).
- [Bia+15] J. Bialké, J. T. Siebert, H. Löwen, and T. Speck. “Negative Interfacial Tension in Phase-Separated Active Brownian Particles”. *Phys. Rev. Lett.* 115 (9 Aug. 2015), p. 098301. DOI: [10.1103/PhysRevLett.115.098301](https://doi.org/10.1103/PhysRevLett.115.098301).
- [Bri+13] A. Bricard, J.-B. Caussin, N. Desreumaux, O. Dauchot, and D. Bartolo. “Emergence of macroscopic directed motion in populations of motile colloids”. en. *Nature* 503.7474 (Nov. 2013), pp. 95–98. DOI: [10.1038/nature12673](https://doi.org/10.1038/nature12673).
- [Buf55] F. P. Buff. “Spherical Interface. II. Molecular Theory”. en. *The Journal of Chemical Physics* 23.3 (Mar. 1955), pp. 419–427. DOI: [10.1063/1.1742005](https://doi.org/10.1063/1.1742005).
- [Cas48] H. B. Casimir. “On the attraction between two perfectly conducting plates”. 51 (1948), p. 793.

- [CC06] C.-H. Chen and H.-Y. Chen. “Finite-size domains in membranes with active two-state inclusions”. *Phys. Rev. E* 74 (5 Nov. 2006), p. 051917. DOI: [10.1103/PhysRevE.74.051917](https://doi.org/10.1103/PhysRevE.74.051917).
- [CF85] P. Coullet and S. Fauve. “Propagative phase dynamics for systems with Galilean invariance”. en. *Physical Review Letters* 55.26 (Dec. 1985), pp. 2857–2859. DOI: [10.1103/PhysRevLett.55.2857](https://doi.org/10.1103/PhysRevLett.55.2857).
- [CGS15] L. F. Cugliandolo, G. Gonnella, and A. Suma. “Rotational and translational diffusion in an interacting active dumbbell system”. en. *Physical Review E* 91.6 (June 2015). DOI: [10.1103/PhysRevE.91.062124](https://doi.org/10.1103/PhysRevE.91.062124).
- [CH93] M. C. Cross and P. C. Hohenberg. “Pattern formation outside of equilibrium”. en. *Reviews of Modern Physics* 65.3 (July 1993), pp. 851–1112. DOI: [10.1103/RevModPhys.65.851](https://doi.org/10.1103/RevModPhys.65.851).
- [Che04] H.-Y. Chen. “Internal States of Active Inclusions and the Dynamics of an Active Membrane”. *Phys. Rev. Lett.* 92 (16 Apr. 2004), p. 168101. DOI: [10.1103/PhysRevLett.92.168101](https://doi.org/10.1103/PhysRevLett.92.168101).
- [CL95] P. M. Chaikin and T. C. Lubensky. *Principles of condensed matter physics*. Cambridge, US: Cambridge University Press, 1995.
- [CM03] S. Cox and P. Matthews. “Instability and localisation of patterns due to a conserved quantity”. en. *Physica D: Nonlinear Phenomena* 175.3-4 (Feb. 2003), pp. 196–219. DOI: [10.1016/S0167-2789\(02\)00733-9](https://doi.org/10.1016/S0167-2789(02)00733-9).
- [CM10] H.-Y. Chen and A. S. Mikhailov. “Dynamics of biomembranes with active multiple-state inclusions”. *Phys. Rev. E* 81 (3 Mar. 2010), p. 031901. DOI: [10.1103/PhysRevE.81.031901](https://doi.org/10.1103/PhysRevE.81.031901).
- [Con10] D. Constantin. “The interaction of hybrid nanoparticles inserted within surfactant bilayers”. *The Journal of Chemical Physics* 133.14 (2010), p. 144901. DOI: [10.1063/1.3499741](https://doi.org/10.1063/1.3499741).
- [Cou+12] D. Coursault, J. Grand, B. Zappone, H. Ayeb, G. Lévi, N. Félidj, and E. Lacaze. “Linear Self-Assembly of Nanoparticles Within Liquid Crystal Defect Arrays”. *Advanced Materials* 24.11 (2012), pp. 1461–1465. DOI: [10.1002/adma.201103791](https://doi.org/10.1002/adma.201103791).
- [CP48] H. B. G. Casimir and D. Polder. “The Influence of Retardation on the London-van der Waals Forces”. *Phys. Rev.* 73 (4 Feb. 1948), pp. 360–372. DOI: [10.1103/PhysRev.73.360](https://doi.org/10.1103/PhysRev.73.360).
- [Dea96] D. S. Dean. “Langevin equation for the density of a system of interacting Langevin processes”. *Journal of Physics A: Mathematical and General* 29.24 (1996), p. L613. DOI: [10.1088/0305-4470/29/24/001](https://doi.org/10.1088/0305-4470/29/24/001).
- [Di +10] R. Di Leonardo et al. “Bacterial ratchet motors”. *Proceedings of the National Academy of Sciences* 107.21 (2010), pp. 9541–9545. DOI: [10.1073/pnas.0910426107](https://doi.org/10.1073/pnas.0910426107).

- [DQ08] R. Dingreville and J. Qu. “Interfacial excess energy, excess stress and excess strain in elastic solids: Planar interfaces”. en. *Journal of the Mechanics and Physics of Solids* 56.5 (May 2008), pp. 1944–1954. DOI: [10.1016/j.jmps.2007.11.003](https://doi.org/10.1016/j.jmps.2007.11.003).
- [Eva+13] J. S. Evans, Y. Sun, B. Senyuk, P. Keller, V. M. Pergamenshchik, T. Lee, and I. I. Smalyukh. “Active Shape-Morphing Elastomeric Colloids in Short-Pitch Cholesteric Liquid Crystals”. en. *Physical Review Letters* 110.18 (Apr. 2013). DOI: [10.1103/PhysRevLett.110.187802](https://doi.org/10.1103/PhysRevLett.110.187802).
- [Fal+16] G. Falasco, F. Baldovin, K. Kroy, and M. Baiesi. “Mesoscopic virial equation for nonequilibrium statistical mechanics”. *New Journal of Physics* 18.9 (2016), p. 093043. DOI: [10.1088/1367-2630/18/9/093043](https://doi.org/10.1088/1367-2630/18/9/093043).
- [FG15] J.-B. Fournier and P. Galatola. “High-order power series expansion of the elastic interaction between conical membrane inclusions”. en. *The European Physical Journal E* 38.8 (Aug. 2015), p. 86. DOI: [10.1140/epje/i2015-15086-3](https://doi.org/10.1140/epje/i2015-15086-3).
- [FG78] M. E. Fisher and P. G. de Gennes. *C. R. Acad. Sci. Paris Ser. B* 287 (1978), p. 207.
- [Fil+17] Y. Fily, Y. Kafri, A. P. Solon, J. Tailleur, and A. Turner. “Mechanical pressure and momentum conservation in dry active matter”. *Journal of Physics A: Mathematical and Theoretical* 51.4 (2017), p. 044003. DOI: [10.1088/1751-8121/aa99b6](https://doi.org/10.1088/1751-8121/aa99b6).
- [Fir+01] M. A. Firestone, D. E. Williams, S. Seifert, and R. Csencsits. “Nanoparticle Arrays Formed by Spatial Compartmentalization in a Complex Fluid”. *Nano Letters* 1.3 (2001), pp. 129–135. DOI: [10.1021/nl10155025](https://doi.org/10.1021/nl10155025).
- [FM12] Y. Fily and M. C. Marchetti. “Athermal Phase Separation of Self-Propelled Particles with No Alignment”. *Phys. Rev. Lett.* 108 (23 June 2012), p. 235702. DOI: [10.1103/PhysRevLett.108.235702](https://doi.org/10.1103/PhysRevLett.108.235702).
- [FNR96] E. Freyssingeas, F. Nallet, and D. Roux. *Langmuir* 12 (1996), p. 6028.
- [Fri+14] P. F. Fribourg, M. Chami, C. O. S. Sorzano, F. Gubellini, R. Marabini, S. Marco, J.-M. Jault, and D. Lévy. “3D Cryo-Electron Reconstruction of BmrA, a Bacterial Multidrug ABC Transporter in an Inward-Facing Conformation and in a Lipidic Environment”. en. *Journal of Molecular Biology* 426.10 (May 2014), pp. 2059–2069. DOI: [10.1016/j.jmb.2014.03.002](https://doi.org/10.1016/j.jmb.2014.03.002).
- [Gam+09a] A. Gambassi, A. Maciołek, C. Hertlein, U. Nellen, L. Helden, C. Bechinger, and S. Dietrich. “Critical Casimir effect in classical binary liquid mixtures”. en. *Physical Review E* 80.6 (Dec. 2009). DOI: [10.1103/PhysRevE.80.061143](https://doi.org/10.1103/PhysRevE.80.061143).
- [Gam+09b] A. Gambassi, C. Hertlein, L. Helden, S. Dietrich, and C. Bechinger. “The critical casimir effect universal fluctuation-induced forces at work”. *Europhysics News* 40.1 (2009), pp. 18–22. DOI: [10.1051/ePN/2009301](https://doi.org/10.1051/ePN/2009301).

- [GBQ04] P.-G. de Gennes, F. Brochard-Wyart, and D. Quéré. “Capillarity and Wet-ting Phenomena Drops, Bubbles, Pearls, Waves” (2004).
- [GDM95] S. C. Glotzer, E. A. Di Marzio, and M. Muthukumar. “Reaction-controlled morphology of phase-separating mixtures”. *Physical review letters* 74.11 (1995), p. 2034. DOI: [10.1103/PhysRevLett.74.2034](https://doi.org/10.1103/PhysRevLett.74.2034).
- [Gen69] P.-G. de Gennes. *J. Phys. (Paris), Colloq.* 30 (1969), pp. C4–65.
- [Gen85] P. G. de Gennes. “Wetting: statics and dynamics”. *Rev. Mod. Phys.* 57 (3 July 1985), pp. 827–863. DOI: [10.1103/RevModPhys.57.827](https://doi.org/10.1103/RevModPhys.57.827).
- [Gin+15] F. Ginot, I. Theurkauff, D. Levis, C. Ybert, L. Bocquet, L. Berthier, and C. Cottin-Bizonne. “Nonequilibrium Equation of State in Suspensions of Active Colloids”. en. *Physical Review X* 5.1 (Jan. 2015). DOI: [10.1103/PhysRevX.5.011004](https://doi.org/10.1103/PhysRevX.5.011004).
- [Gin+18] F. Ginot, A. Solon, Y. Kafri, C. Ybert, J. Tailleur, and C. Cottin-Bizonne. “Sedimentation of self-propelled Janus colloids: polarization and pressure”. *New Journal of Physics* 20.11 (2018), p. 115001. DOI: [10.1088/1367-2630/aae732](https://doi.org/10.1088/1367-2630/aae732).
- [GP93] P.-G. de Gennes and J. Prost. *The Physics of Liquid Crystals*. Oxford: Oxford Science Publications, 1993.
- [GS18] J. Grawitter and H. Stark. “Feedback control of photoresponsive fluid in-terfaces”. en. *Soft Matter* 14.10 (2018), pp. 1856–1869. DOI: [10.1039/C7SM02101A](https://doi.org/10.1039/C7SM02101A).
- [GSJ94] S. C. Glotzer, D. Stauffer, and N. Jan. “Monte Carlo simulations of phase separation in chemically reactive binary mixtures”. *Physical review letters* 72.26 (1994), p. 4109. DOI: [10.1103/PhysRevLett.72.4109](https://doi.org/10.1103/PhysRevLett.72.4109).
- [Guo+10] C. Guo, J. Wang, F. Cao, R. J. Lee, and G. Zhai. “Lyotropic liquid crystal systems in drug delivery”. *Drug Discovery Today* 15.23 (2010), pp. 1032–1040. DOI: [10.1016/j.drudis.2010.09.006](https://doi.org/10.1016/j.drudis.2010.09.006).
- [Ham03] I. W. Hamley. “Nanotechnology with Soft Materials”. *Angewandte Chemie International Edition* 42.15 (2003), pp. 1692–1712. DOI: [10.1002/anie.200200546](https://doi.org/10.1002/anie.200200546). eprint: <https://onlinelibrary.wiley.com/doi/pdf/10.1002/anie.200200546>.
- [Hel73] W. Helfrich. “Elastic properties of lipid bilayers: theory and possible exper-iments”. *Z. Naturforsch. C* 28 (1973), p. 693. DOI: [10.1515/znc-1973-11-1209](https://doi.org/10.1515/znc-1973-11-1209).
- [Hel78] W. Helfrich. “Steric interaction of fluid membranes in multilayer systems”. *Z. Naturforsch. A* 83 (1978), p. 305. DOI: [10.1515/zna-1978-0308](https://doi.org/10.1515/zna-1978-0308).
- [Her+08] C. Hertlein, L. Helden, A. Gambassi, S. Dietrich, and C. Bechinger. “Direct measurement of critical Casimir forces”. *Nature* 451.7175 (2008), pp. 172–175. DOI: [10.1038/nature06443](https://doi.org/10.1038/nature06443).

- [HF18] J. Halatek and E. Frey. “Rethinking pattern formation in reaction–diffusion systems”. En. *Nature Physics* 14.5 (May 2018), p. 507. DOI: [10.1038/s41567-017-0040-5](https://doi.org/10.1038/s41567-017-0040-5).
- [HL99] M. Heni and H. Löwen. “Interfacial free energy of hard-sphere fluids and solids near a hard wall”. en. *Physical Review E* 60.6 (Dec. 1999), pp. 7057–7065. DOI: [10.1103/PhysRevE.60.7057](https://doi.org/10.1103/PhysRevE.60.7057).
- [Hoł91] R. Hołyst. “Landau-Peierls instability, x-ray-diffraction patterns, and surface freezing in thin smectic films”. *Physical Review A* 44.6 (Sept. 1991), pp. 3692–3709. DOI: [10.1103/PhysRevA.44.3692](https://doi.org/10.1103/PhysRevA.44.3692).
- [IK50] J. H. Irving and J. G. Kirkwood. “The Statistical Mechanical Theory of Transport Processes. IV. The Equations of Hydrodynamics”. *The Journal of Chemical Physics* 18.6 (1950), pp. 817–829. DOI: [10.1063/1.1747782](https://doi.org/10.1063/1.1747782).
- [Jho+10] Y. S. Jho, M. W. Kim, S. A. Safran, and P. A. Pincus. “Lamellar phase coexistence induced by electrostatic interactions”. *The European Physical Journal E* 31.2 (Feb. 2010), pp. 207–214. DOI: [10.1140/epje/i2010-10567-5](https://doi.org/10.1140/epje/i2010-10567-5).
- [JS92] M. Jonstroemer and R. Strey. “Nonionic bilayers in dilute solutions: effect of additives”. en. *The Journal of Physical Chemistry* 96.14 (July 1992), pp. 5993–6000. DOI: [10.1021/j100193a064](https://doi.org/10.1021/j100193a064).
- [Jun+17] G. Junot, G. Briand, R. Ledesma-Alonso, and O. Dauchot. “Active versus passive hard disks against a membrane: mechanical pressure and instability”. *Physical review letters* 119.2 (2017), p. 028002. DOI: [10.1103/PhysRevLett.119.028002](https://doi.org/10.1103/PhysRevLett.119.028002).
- [Kat+16] S. Katira, K. K. Mandadapu, S. Vaikuntanathan, B. Smit, and D. Chandler. “Pre-transition effects mediate forces of assembly between transmembrane proteins”. en. *eLife* 5 (Feb. 2016). DOI: [10.7554/eLife.13150](https://doi.org/10.7554/eLife.13150).
- [KB49] J. G. Kirkwood and F. P. Buff. “The statistical mechanical theory of surface tension”. *The Journal of Chemical Physics* 17.3 (1949), pp. 338–343.
- [KD91] M. Krech and S. Dietrich. “Finite-size scaling for critical films”. en. *Physical Review Letters* 66.3 (Jan. 1991), pp. 345–348. DOI: [10.1103/PhysRevLett.66.345](https://doi.org/10.1103/PhysRevLett.66.345).
- [Kra06] W. Krauth. *Statistical Mechanics Algorithms and Computations*. Oxford: Oxford University Press, 2006.
- [Lad67] F. Lado. *J. Chem. Phys.* 47 (1967), p. 4828.
- [Lad68] F. Lado. *J. Chem. Phys.* 49 (1968), p. 3092.
- [Lan17] I. Langmuir. “The constitution and fundamental properties of solids and liquids. II. Liquids.” *Journal of the American chemical society* 39.9 (1917), pp. 1848–1906.

- [Lew+13] W. Lewandowski, D. Constantin, K. Walicka, D. Pocięcha, J. Mieczkowski, and E. Górecka. “Smectic mesophases of functionalized silver and gold nanoparticles with anisotropic plasmonic properties”. *Chemical Communications* 49.71 (2013), pp. 7845–7847. DOI: [10.1039/c3cc43166e](https://doi.org/10.1039/c3cc43166e).
- [Liu+10] Q. Liu, Y. Cui, D. Gardner, X. Li, S. He, and I. I. Smalyukh. “Self-Alignment of Plasmonic Gold Nanorods in Reconfigurable Anisotropic Fluids for Tunable Bulk Metamaterial Applications”. *Nano Letters* 10.4 (2010), pp. 1347–1353. DOI: [10.1021/nl9042104](https://doi.org/10.1021/nl9042104).
- [LK92] H. Li and M. Kardar. “Fluctuation-induced forces between manifolds immersed in correlated fluids”. *Phys. Rev. A* 46 (10 Nov. 1992), pp. 6490–6500. DOI: [10.1103/PhysRevA.46.6490](https://doi.org/10.1103/PhysRevA.46.6490).
- [LM77] J. Langer and J. Müller-Krumbhaar. “Stability effects in dendritic crystal growth”. en. *Journal of Crystal Growth* 42 (Dec. 1977), pp. 11–14. DOI: [10.1016/0022-0248\(77\)90171-3](https://doi.org/10.1016/0022-0248(77)90171-3).
- [LM79] L. Liebert and A. Martinet. “Coupling between nematic lyomesophases and ferrofluids”. *Journal de Physique Lettres* 40.15 (1979), pp. 363–368. DOI: [10.1051/jphyslet:019790040015036300](https://doi.org/10.1051/jphyslet:019790040015036300).
- [LMC08] D. Loi, S. Mossa, and L. F. Cugliandolo. “Effective temperature of active matter”. en. *Physical Review E* 77.5 (May 2008). DOI: [10.1103/PhysRevE.77.051111](https://doi.org/10.1103/PhysRevE.77.051111).
- [LMS09] C. P. Lapointe, T. G. Mason, and I. I. Smalyukh. “Shape-Controlled Colloidal Interactions in Nematic Liquid Crystals”. en. *Science* 326.5956 (Nov. 2009), pp. 1083–1086. DOI: [10.1126/science.1176587](https://doi.org/10.1126/science.1176587).
- [LS99] J. L. Lebowitz and H. Spohn. “A Gallavotti–Cohen-Type Symmetry in the Large Deviation Functional for Stochastic Dynamics”. *Journal of Statistical Physics* 95.1 (Apr. 1, 1999), pp. 333–365. DOI: [10.1023/A:1004589714161](https://doi.org/10.1023/A:1004589714161).
- [LSB95] N. Lei, C. R. Safinya, and R. F. Bruinsma. “Discrete Harmonic Model for Stacked Membranes: Theory and Experiment”. *J Phys II France* 5.8 (Aug. 1995), pp. 1155–1163. DOI: [10.1051/jp2:1995174](https://doi.org/10.1051/jp2:1995174).
- [LYS14] Q. Liu, Y. Yuan, and I. I. Smalyukh. “Electrically and Optically Tunable Plasmonic Guest–Host Liquid Crystals with Long-Range Ordered Nanoparticles”. *Nano Letters* 14.7 (2014), pp. 4071–4077. DOI: [10.1021/nl501581y](https://doi.org/10.1021/nl501581y).
- [Mal+14] S. Mallory, A. Šarić, C. Valeriani, and A. Cacciuto. “Anomalous thermo-mechanical properties of a self-propelled colloidal fluid”. *Physical Review E* 89.5 (2014), p. 052303. DOI: [10.1103/PhysRevE.89.052303](https://doi.org/10.1103/PhysRevE.89.052303).
- [Mar+11] A. Marchand, J. H. Weijs, J. H. Snoeijer, and B. Andreotti. “Why is surface tension a force parallel to the interface?” en. *American Journal of Physics* 79.10 (Oct. 2011), pp. 999–1008. DOI: [10.1119/1.3619866](https://doi.org/10.1119/1.3619866).
- [MC00] P. C. Matthews and S. M. Cox. “Pattern formation with a conservation law”. en. *Nonlinearity* 13.4 (July 2000). arXiv: nlin/0006002, pp. 1293–1320. DOI: [10.1088/0951-7715/13/4/317](https://doi.org/10.1088/0951-7715/13/4/317).

- [MMM16] U. Marini Bettolo Marconi, C. Maggi, and S. Melchionna. “Pressure and surface tension of an active simple liquid: a comparison between kinetic, mechanical and free-energy based approaches”. en. *Soft Matter* 12.26 (2016), pp. 5727–5738. DOI: [10.1039/C6SM00667A](https://doi.org/10.1039/C6SM00667A).
- [Nar+17] C. Nardini, É. Fodor, E. Tjhung, F. van Wijland, J. Tailleur, and M. E. Cates. “Entropy Production in Field Theories without Time-Reversal Symmetry: Quantifying the Non-Equilibrium Character of Active Matter”. *Phys. Rev. X* 7 (2 Apr. 2017), p. 021007. DOI: [10.1103/PhysRevX.7.021007](https://doi.org/10.1103/PhysRevX.7.021007).
- [NB77] G. Navascués and M. Berry. “The statistical mechanics of wetting”. en. *Molecular Physics* 34.3 (Sept. 1977), pp. 649–664. DOI: [10.1080/00268977700102021](https://doi.org/10.1080/00268977700102021).
- [NF17] H. Noguchi and J.-B. Fournier. “Membrane structure formation induced by two types of banana-shaped proteins”. en. *Soft Matter* 13.22 (2017), pp. 4099–4111. DOI: [10.1039/C7SM00305F](https://doi.org/10.1039/C7SM00305F).
- [Nik+16] N. Nikola, A. P. Solon, Y. Kafri, M. Kardar, J. Tailleur, and R. Voituriez. “Active Particles with Soft and Curved Walls: Equation of State, Ratchets, and Instabilities”. *Phys. Rev. Lett.* 117 (9 Aug. 2016), p. 098001. DOI: [10.1103/PhysRevLett.117.098001](https://doi.org/10.1103/PhysRevLett.117.098001).
- [NT79] G. Navascués and P. Tarazona. “Surface tension of hard sphere fluid near a wall”. en. *Molecular Physics* 37.4 (Apr. 1979), pp. 1077–1087. DOI: [10.1080/00268977900100821](https://doi.org/10.1080/00268977900100821).
- [NvL90] M. J. P. Nijmeijer, van, and J. M. J. Leeuwen. “Microscopic expressions for the surface and line tension”. *Journal of Physics A: Mathematical and General* 23.19 (Oct. 1990), pp. 4211–4235. DOI: [10.1088/0305-4470/23/19/010](https://doi.org/10.1088/0305-4470/23/19/010).
- [Nyc+13] A. Nych, U. Ognysta, M. Škarabot, M. Ravnik, S. Žumer, and I. Mušević. “Assembly and control of 3D nematic dipolar colloidal crystals”. en. *Nature Communications* 4.1 (June 2013). DOI: [10.1038/ncomms2486](https://doi.org/10.1038/ncomms2486).
- [OB88] Y. Oono and M. Bahiana. “ $2/3$ -Power law for copolymer lamellar thickness implies a $1/3$ -power law for spinodal decomposition”. *Physical review letters* 61.9 (1988), p. 1109. DOI: [10.1103/PhysRevLett.61.1109](https://doi.org/10.1103/PhysRevLett.61.1109).
- [OK60] S. Ono and S. Kondo. “Molecular Theory of Surface Tension in Liquids”. *Structure of Liquids / Struktur der Flüssigkeiten*. Berlin, Heidelberg: Springer Berlin Heidelberg, 1960, pp. 134–280. DOI: [10.1007/978-3-642-45947-4_2](https://doi.org/10.1007/978-3-642-45947-4_2).
- [OS87] Y. Oono and Y. Shiwa. “Computationally efficient modeling of block copolymer and benard pattern formations”. *Modern Physics Letters B* 01.01n02 (1987), pp. 49–55. DOI: [10.1142/S0217984987000077](https://doi.org/10.1142/S0217984987000077).
- [Pal+17] S. Paliwal, V. Prymidis, L. Filion, and M. Dijkstra. “Non-equilibrium surface tension of the vapour-liquid interface of active Lennard-Jones particles”. *The Journal of chemical physics* 147.8 (2017), p. 084902. DOI: [10.1063/1.4989764](https://doi.org/10.1063/1.4989764).

- [Pan+11] B. Pansu, A. Lecchi, D. Constantin, M. Imp  rator-Clerc, M. Veber, and I. Dozov. “Insertion of Gold Nanoparticles in Fluid Mesophases: Size Filtering and Control of Interactions”. *The Journal of Physical Chemistry C* 115.36 (2011), pp. 17682–17687. DOI: [10.1021/jp2046189](https://doi.org/10.1021/jp2046189).
- [Pat+18] A. Patch, D. M. Sussman, D. Yllanes, and M. C. Marchetti. “Curvature-dependent tension and tangential flows at the interface of motility-induced phases”. *Soft matter* 14.36 (2018), pp. 7435–7445. DOI: [10.1039/C8SM00899J](https://doi.org/10.1039/C8SM00899J).
- [Pet+98] H. I. Petrache, N. Gouliaev, S. Tristram-Nagle, R. Zhang, R. M. Suter, and J. F. Nagle. “Interbilayer interactions from high-resolution x-ray scattering”. *Physical Review E* 57.6 (June 1998), pp. 7014–7024. DOI: [10.1103/PhysRevE.57.7014](https://doi.org/10.1103/PhysRevE.57.7014).
- [PF98] S. Puri and H. L. Frisch. “Phase Separation in Binary Mixtures with Chemical Reactions”. *International Journal of Modern Physics B* 12.15 (1998), pp. 1623–1641. DOI: [10.1142/S0217979298000892](https://doi.org/10.1142/S0217979298000892).
- [PM97] P. Sens and M.S. Turner. “Inclusions in Thin Smectic Films”. *J. Phys. II France* 7.12 (1997), pp. 1855–1870. DOI: [10.1051/jp2:1997218](https://doi.org/10.1051/jp2:1997218).
- [Pou+97] P. Poulin, H. Stark, T. C. Lubensky, and D. A. Weitz. “Novel Colloidal Interactions in Anisotropic Fluids”. *Science* 275.5307 (1997), pp. 1770–1773. DOI: [10.1126/science.275.5307.1770](https://doi.org/10.1126/science.275.5307.1770).
- [Pra+09] R. Pratibha, K. Park, I. I. Smalyukh, and W. Park. “Tunable optical metamaterial based on liquid crystal-gold nanosphere composite”. *Optics express* 17.22 (2009), pp. 19459–19469. DOI: [10.1364/OE.17.019459](https://doi.org/10.1364/OE.17.019459).
- [PV02] A. Pelissetto and E. Vicari. “Critical phenomena and renormalization-group theory”. *Physics Reports* 368.6 (2002), pp. 549–727. DOI: [https://doi.org/10.1016/S0370-1573\(02\)00219-3](https://doi.org/10.1016/S0370-1573(02)00219-3).
- [RBL05a] R. Reigada, J. Buceta, and K. Lindenberg. “Generation of dynamic structures in nonequilibrium reactive bilayers”. en. *Physical Review E* 72.5 (Nov. 2005). DOI: [10.1103/PhysRevE.72.051921](https://doi.org/10.1103/PhysRevE.72.051921).
- [RBL05b] R. Reigada, J. Buceta, and K. Lindenberg. “Nonequilibrium patterns and shape fluctuations in reactive membranes”. en. *Physical Review E* 71.5 (May 2005). DOI: [10.1103/PhysRevE.71.051906](https://doi.org/10.1103/PhysRevE.71.051906).
- [Rie92a] H. Riecke. “Ginzburg-Landau equation coupled to a concentration field in binary-mixture convection”. *Physica D: Nonlinear Phenomena* 61.1 (1992), pp. 253–259. DOI: [https://doi.org/10.1016/0167-2789\(92\)90169-N](https://doi.org/10.1016/0167-2789(92)90169-N).
- [Rie92b] H. Riecke. “Self-trapping of traveling-wave pulses in binary mixture convection”. en. *Physical Review Letters* 68.3 (Jan. 1992), pp. 301–304. DOI: [10.1103/PhysRevLett.68.301](https://doi.org/10.1103/PhysRevLett.68.301).
- [RL76] M. Rao and D. Levesque. “Surface structure of a liquid film”. *The Journal of Chemical Physics* 65.8 (1976), pp. 3233–3236. DOI: [10.1063/1.433495](https://doi.org/10.1063/1.433495).

- [RS88] D. Roux and C. R. Safinya. “A synchrotron X-ray study of competing undulation and electrostatic interlayer interactions in fluid multimembrane lyotropic phases”. *Journal de Physique* 49.2 (1988), pp. 307–318. DOI: [10.1051/jphys:01988004902030700](https://doi.org/10.1051/jphys:01988004902030700).
- [RW82] J. Rowlinson and B. Widom. “Molecular Theory of Capillarity 1982”. *Clarendon: Oxford* (1982), p. 56.
- [Saf94] S. A. Safran. *Statistical thermodynamics of surfaces, interfaces, and membranes*. Reading, Massachusetts: Addison-Wesley, 1994.
- [SAK10] K. P. Sharma, V. K. Aswal, and G. Kumaraswamy. “Adsorption of Non-ionic Surfactant on Silica Nanoparticles: Structure and Resultant Interparticle Interactions”. *The Journal of Physical Chemistry B* 114.34 (2010), pp. 10986–10994. DOI: [10.1021/jp1033799](https://doi.org/10.1021/jp1033799).
- [SD16] R. Sarfati and E. R. Dufresne. “Long-range attraction of particles adhered to lipid vesicles”. en. *Physical Review E* 94.1 (July 2016). DOI: [10.1103/PhysRevE.94.012604](https://doi.org/10.1103/PhysRevE.94.012604).
- [Sez+17] E. Sezgin, I. Levental, S. Mayor, and C. Eggeling. “The mystery of membrane organization: composition, regulation and roles of lipid rafts”. *Nature Reviews Molecular Cell Biology* 18 (Mar. 2017), p. 361. DOI: [10.1038/nrm.2017.16](https://doi.org/10.1038/nrm.2017.16).
- [SGJ17] C. Sandford, A. Y. Grosberg, and J.-F. Joanny. “Pressure and flow of exponentially self-correlated active particles”. *Physical Review E* 96.5 (2017), p. 052605. DOI: [10.1103/PhysRevE.96.052605](https://doi.org/10.1103/PhysRevE.96.052605).
- [SH77] J. Swift and P. C. Hohenberg. “Hydrodynamic fluctuations at the convective instability”. en. *Physical Review A* 15.1 (Jan. 1977), pp. 319–328. DOI: [10.1103/PhysRevA.15.319](https://doi.org/10.1103/PhysRevA.15.319).
- [SH82] P. Schofield and J. R. Henderson. “Statistical mechanics of inhomogeneous fluids”. *Proceedings of the Royal Society of London. A. Mathematical and Physical Sciences* 379.1776 (1982), pp. 231–246. DOI: [10.1098/rspa.1982.0015](https://doi.org/10.1098/rspa.1982.0015).
- [Shu50] R. Shuttleworth. “The Surface Tension of Solids”. en. *Proceedings of the Physical Society. Section A* 63.5 (May 1950), pp. 444–457. DOI: [10.1088/0370-1298/63/5/302](https://doi.org/10.1088/0370-1298/63/5/302).
- [SJ16] T. Speck and R. L. Jack. “Ideal bulk pressure of active Brownian particles”. *Phys. Rev. E* 93 (6 June 2016), p. 062605. DOI: [10.1103/PhysRevE.93.062605](https://doi.org/10.1103/PhysRevE.93.062605).
- [SK03] C. D. Santangelo and R. D. Kamien. “Bogomol’nyi, Prasad, and Sommerfield Configurations in Smectics”. *Phys. Rev. Lett.* 91 (4 July 2003), p. 045506. DOI: [10.1103/PhysRevLett.91.045506](https://doi.org/10.1103/PhysRevLett.91.045506).
- [Sok+10] A. Sokolov, M. M. Apodaca, B. A. Grzybowski, and I. S. Aranson. “Swimming bacteria power microscopic gears”. *Proceedings of the National Academy of Sciences* 107.3 (2010), pp. 969–974. DOI: [10.1073/pnas.0913015107](https://doi.org/10.1073/pnas.0913015107).

- [Sok10] I. M. Sokolov. “Statistical mechanics of entropic forces: disassembling a toy”. *European Journal of Physics* 31.6 (2010), p. 1353. DOI: [10.1088/0143-0807/31/6/005](https://doi.org/10.1088/0143-0807/31/6/005).
- [Sol+15] A. P. Solon, Y. Fily, A. Baskaran, M. E. Cates, Y. Kafri, M. Kardar, and J. Tailleur. “Pressure is not a state function for generic active fluids”. *Nature Physics* 11.8 (2015), p. 673. DOI: [10.1038/nphys3377](https://doi.org/10.1038/nphys3377).
- [Sol+18] A. P. Solon, J. Stenhammar, M. E. Cates, Y. Kafri, and J. Tailleur. “Generalized thermodynamics of motility-induced phase separation: phase equilibria, Laplace pressure, and change of ensembles”. en. *New Journal of Physics* 20.7 (July 2018), p. 075001. DOI: [10.1088/1367-2630/aacdd](https://doi.org/10.1088/1367-2630/aacdd).
- [Soy+08] F. Soyka, O. Zvyagolskaya, C. Hertlein, L. Helden, and C. Bechinger. “Critical Casimir Forces in Colloidal Suspensions on Chemically Patterned Surfaces”. en. *Physical Review Letters* 101.20 (Nov. 2008). DOI: [10.1103/PhysRevLett.101.208301](https://doi.org/10.1103/PhysRevLett.101.208301).
- [ST01] P. Sens and M. Turner. “Structure factor of a lamellar smectic phase with inclusions”. *The European Physical Journal E* 4.1 (Jan. 1, 2001), pp. 115–120. DOI: [10.1007/s101890170149](https://doi.org/10.1007/s101890170149).
- [Sta65] C. E. Stauffer. “The Measurement of Surface Tension by the Pendant Drop Technique”. en. *The Journal of Physical Chemistry* 69.6 (June 1965), pp. 1933–1938. DOI: [10.1021/j100890a024](https://doi.org/10.1021/j100890a024).
- [Ste+15] J. Stenhammar, R. Wittkowski, D. Marenduzzo, and M. E. Cates. “Activity-Induced Phase Separation and Self-Assembly in Mixtures of Active and Passive Particles”. en. *Physical Review Letters* 114.1 (Jan. 2015). DOI: [10.1103/PhysRevLett.114.018301](https://doi.org/10.1103/PhysRevLett.114.018301).
- [Sum+14] A. Sumino, D. Yamamoto, M. Iwamoto, T. Dewa, and S. Oiki. “Gating-Associated Clustering–Dispersion Dynamics of the KcsA Potassium Channel in a Lipid Membrane”. en. *The Journal of Physical Chemistry Letters* 5.3 (Feb. 2014), pp. 578–584. DOI: [10.1021/jz402491t](https://doi.org/10.1021/jz402491t).
- [Sur+05] G. Surendran et al. “Highly Swollen Liquid Crystals as New Reactors for the Synthesis of Nanomaterials”. *Chemistry of Materials* 17.6 (2005), pp. 1505–1514. DOI: [10.1021/cm0484495](https://doi.org/10.1021/cm0484495). eprint: <https://doi.org/10.1021/cm0484495>.
- [TFL13] O. M. Tovkach, J.-i. Fukuda, and B. I. Lev. “Peculiarity of the interaction of small particles in smectic liquid crystals”. *Phys. Rev. E* 88 (5 Nov. 2013), p. 052502. DOI: [10.1103/PhysRevE.88.052502](https://doi.org/10.1103/PhysRevE.88.052502).
- [TS97] M. S. Turner and P. Sens. “Interactions between particulate inclusions in a smectic-A liquid crystal”. *Phys. Rev. E* 55 (2 Feb. 1997), R1275–R1278. DOI: [10.1103/PhysRevE.55.R1275](https://doi.org/10.1103/PhysRevE.55.R1275).
- [TS98] M. S. Turner and P. Sens. “Multipole expansion for inclusions in a lamellar phase”. *Phys. Rev. E* 57 (1 Jan. 1998), pp. 823–828. DOI: [10.1103/PhysRevE.57.823](https://doi.org/10.1103/PhysRevE.57.823).

- [TYB14] S. C. Takatori, W. Yan, and J. F. Brady. “Swim pressure: stress generation in active matter”. *Physical review letters* 113.2 (2014), p. 028103.
- [Van+16] C. Van Der Wel, A. Vahid, A. Šarić, T. Idema, D. Heinrich, and D. J. Kraft. “Lipid membrane-mediated attraction between curvature inducing objects”. *Scientific Reports* 6 (Sept. 2016). DOI: [10.1038/srep32825](https://doi.org/10.1038/srep32825).
- [Ven+11] E. Venugopal, S. K. Bhat, J. J. Vallooran, and R. Mezzenga. “Phase Behavior of Lipid-Based Lyotropic Liquid Crystals in Presence of Colloidal Nanoparticles”. *Langmuir* 27.16 (2011), pp. 9792–9800. DOI: [10.1021/la201767p](https://doi.org/10.1021/la201767p).
- [Viz+17] G. Vizsnyiczai, G. Frangipane, C. Maggi, F. Saglimbeni, S. Bianchi, and R. Di Leonardo. “Light controlled 3D micromotors powered by bacteria”. *Nature communications* 8 (2017), p. 15974. DOI: [10.1038/ncomms15974](https://doi.org/10.1038/ncomms15974).
- [VM05] D. Vella and L. Mahadevan. “The “Cheerios effect””. en. *American Journal of Physics* 73.9 (Sept. 2005), pp. 817–825. DOI: [10.1119/1.1898523](https://doi.org/10.1119/1.1898523).
- [WBS09a] B. West, F. L. H. Brown, and F. Schmid. “Membrane-Protein Interactions in a Generic Coarse-Grained Model for Lipid Bilayers”. *Biophysical Journal* 96.1 (2009), pp. 101–115. DOI: <https://doi.org/10.1529/biophysj.108.138677>.
- [WBS09b] B. West, F. L. Brown, and F. Schmid. “Membrane-Protein Interactions in a Generic Coarse-Grained Model for Lipid Bilayers”. en. *Biophysical Journal* 96.1 (Jan. 2009), pp. 101–115. DOI: [10.1529/biophysj.108.138677](https://doi.org/10.1529/biophysj.108.138677).
- [Weia] E. W. Weisstein. *Bessel Function of the First Kind*. en. Text.
- [Weib] E. W. Weisstein. *Modified Bessel Function of the Second Kind*. en. Text.
- [WER99] W. Wang, S. Efrima, and O. Regev. “Directing Silver Nanoparticles into Colloid-Surfactant Lyotropic Lamellar Systems”. *The Journal of Physical Chemistry B* 103.27 (July 1999), pp. 5613–5621. DOI: [10.1021/jp983125n](https://doi.org/10.1021/jp983125n).
- [Win06] D. M. Winterbottom. “Pattern formation with a conservation law”. 2006.
- [Woj+09] M. Wojcik, W. Lewandowski, J. Matraszek, J. Mieczkowski, J. Borysiuk, D. Pocięcha, and E. Gorecka. “Liquid-crystalline phases made of gold nanoparticles”. *Angewandte Chemie (International Ed. in English)* 48.28 (2009), pp. 5167–5169. DOI: [10.1002/anie.200901206](https://doi.org/10.1002/anie.200901206).
- [WWF16] S. N. Weber, C. A. Weber, and E. Frey. “Binary Mixtures of Particles with Different Diffusivities Demix”. en. *Physical Review Letters* 116.5 (Feb. 2016). DOI: [10.1103/PhysRevLett.116.058301](https://doi.org/10.1103/PhysRevLett.116.058301).
- [WWG15] R. G. Winkler, A. Wysocki, and G. Gompper. “Virial pressure in systems of spherical active Brownian particles”. *Soft matter* 11.33 (2015), pp. 6680–6691. DOI: [10.1039/C5SM01412C](https://doi.org/10.1039/C5SM01412C).

- [Yan+99] L. Yang, T. Weiss, T. Harroun, W. Heller, and H. Huang. “Supramolecular structures of peptide assemblies in membranes by neutron off-plane scattering: method of analysis”. *Biophys. J.* 77.5 (1999), pp. 2648–2656. DOI: [10.1016/S0006-3495\(99\)77099-2](https://doi.org/10.1016/S0006-3495(99)77099-2).
- [YMM14] X. Yang, M. L. Manning, and M. C. Marchetti. “Aggregation and segregation of confined active particles”. *Soft matter* 10.34 (2014), pp. 6477–6484. DOI: [10.1039/C4SM00927D](https://doi.org/10.1039/C4SM00927D).
- [You05] T. Young. “III. An essay on the cohesion of fluids”. *Philosophical Transactions of the Royal Society of London* 95 (1805), pp. 65–87. DOI: [10.1098/rstl.1805.0005](https://doi.org/10.1098/rstl.1805.0005). eprint: <https://royalsocietypublishing.org/doi/pdf/10.1098/rstl.1805.0005>.
- [Zak+19] R. Zakine, D. de Silva Edirimuni, D. Constantin, P. Galatola, and J.-B. Fournier. “Interaction and structuration of membrane-binding and membrane-excluding colloidal particles in lamellar phases”. *Soft Matter* (2019), pages. DOI: [10.1039/C9SM00230H](https://doi.org/10.1039/C9SM00230H).

Liste des éléments retirés

Figure 1.1 , page 21

Figure 1.2 , page 21

Figure 1.3 , page 22

Figure 1.4 , page 23

Figure 1.5 , page 23